2004-04-29

Process Models for Laser Engineered Net Shaping

John Kummailil
Worcester Polytechnic Institute

PROCESS MODELS FOR LASER ENGINEERED NET SHAPING

by

John Kummailil

A Dissertation

Submitted to the Faculty

of the

WORCESTER POLYTECHNIC INSTITUTE

in partial fulfillment of the requirements for the

Degree of Doctor of Philosophy

in

Manufacturing Engineering

May 2004

APPROVED:

Professor Christopher A. Brown
(Advisor and Program Head)

Professor Kevin Rong

Professor William C. S. Weir

Mr. Carmine Sammarco

Dr. David J. Skinner

Abstract

The goal of this dissertation is to develop a model relating LENS™ process parameters to deposited thickness, incorporating the effect of substrate heating. A design review was carried out, adapting the technique of functional decomposition borrowed from axiomatic design. The review revealed that coupling between the laser path and laser power caused substrate heating. The material delivery mechanism was modeled and verified using experimental data. It was used in the derivation of the average deposition model which predicted deposition based on build parameters, but did not incorporate substrate heating. The average deposition model appeared capable of predicting deposited thickness for single line, 1-layer and 2-layer builds, performing best for the 1-layer builds which were built under essentially isothermal conditions.

This model was extended to incorporate the effect of substrate heating, estimated using an energy partition approach. The energy used for substrate heating was modeled as a series of timed heating events from an instantaneous point heat source along the path of the laser. The result was called the spatial deposition model, and was verified using the same set of experimental data. The model appeared capable of predicting deposited thickness for single line, 1-layer and 2-layer builds and was able to predict the characteristic temperature rise near the borders as the laser reversed direction.

For my *bhariya,* my *appachen* and my *ammachan*

and, of course, for my *appa* and *amma*:

they know why

TABLE OF CONTENTS

List of Figures

List of Tables

Acknowledgements

I did not – and could not – have got here alone. This section is for the many people who held my hand and walked me through this programme.

I tried to choose my committee cautiously, selecting members who would help me negotiate the challenges I must face, but even I did not expect the extent of support they would give me. Prof. Brown, in particular, spent many hours going over derivations with me, eliminating inconsistencies, simplifying and refining our ideas. He provided me with a stipend relieving me of the mundane necessity of finding other employment, freeing me to concentrate on experimentation and research instead. He opened his beautiful house to my family and took the pressure off me by constantly reiterating that there was more to life than work. Prof. Rong took a great interest in this research, allowing me to present experimental results in his class. He had valuable input on the design of experiments and in the final shape of this document. Prof. Weir and I spent many hours discussing the engineering challenges to be overcome in getting experiments to work – a lot of this research would not have been possible without his input. I owe a lot to Mr. Sammarco and Dr. Skinner, my ex-supervisor and my ex-colleague respectively. The three of us spent countless hours on the equipment, bouncing ideas off each other, trying to fathom its workings. I must also thank them for keeping me employed as the company we worked for slowly folded around us, enabling me to land on my feet in WPI.

I would like to thank LaserFare; in particular Mr. Mueller and Mr. Feeley, for the use of their equipment and Mr. Wirta, for helping me run it. I thank Prof. Stucker, from URI, for letting us use the equipment in his laboratories.

I gratefully acknowledge the help of the ME and MFE students for helping me through the programme. In particular, I thank Mr. Bergstrom, Mr. Geiger, Mr. Munyon and Ms. Hamel some of whom helped me with experimental issues and some of whom listened to my presentation and provided valuable input. I thank Dr. Hahn for letting me bounce questions off him and Ms. Milkman for taking care of things I am incapable of, such as organizing notices, ordering food and reserving rooms.

No westerner can ever understand the competition for access to higher education in less affluent countries. I would like to thank my parents Mr. and Mrs. K. Jacob John for the innumerable nights they stayed up with me, making sure I stayed awake and studied for my entrance exams to engineering college. I would like to thank Mrs. Allagapan, who set me sample papers and corrected them on a daily basis, preparing me for these exams. I'd like to thank Mr. and Mrs. John for critiquing my work and for the welcome relief of their visits provided me. I thank Dr. Mathew for providing support in person at my defense. I would like to thank Dr. Jacob Eapen, Dr. Sucy Eapen, my parents-in-law, and Mr. George Eapen, my brother-in-law for being my most avid fans as I completed this programme. And finally, I would like to thank my darling wife for everything: without her, I could not and would not have accomplished this.

Nomenclature

Symbol	Explanation
a	Power to which build parameters are raised in material delivery model
A_{Bead}	Area of the cross section of the melt bead
A_{CS}	Area of the cross section of the melt bead
A_{HAZ}	Area of the cross section of the heat affected zone on the substrate
A_M	Area of the region on the substrate into which material falls
A_L	Area of the region on the substrate that is molten
c_p	Specific heat capacity
C_{AM}	Dimensionless constant relating A_M to d_{Pwdr} (shape factor)
C_{AL}	Dimensionless constant relating A_L to d_{Melt} (shape factor)
C_{CS}	Dimensionless constant relating A_{CS} to z^2 (shape factor)
d_{Pwdr}	Length characteristic of the region into which powders fall
d_{Melt}	Length characteristic of the region which is molten
f_1	Fraction of material available for deposition
f_2	Fraction of absorbed energy used for deposition
GPa	Giga Pascals
h_f	Heat of fusion
K	Thermal Conductivity
K_A	Average Deposition Model Constant.
K_{EA}	Average Deposition Model, Energy Constant.
K_M	Material Delivery Model Constant
K_S	Spatial Deposition Model Constant
m	Mass
m_s	Mass of substrate
m_y	Mass per unit length
$\dot{m}$	Mass flow rate
mg	Milligramme
N	Number of layers
P	Laser Power
P_c	Critical laser power to initiate melting
P_{Max}	Upper bound of laser location on the substrate.
P_{Min}	Lower bound of laser location on the substrate.
$P(t)$	Position of the laser relative to the origin
Q	Energy

Q_L	Constant energy from the laser
$Q(x,y,z,t)$	Energy at a location (x,y,z) on the laser path that it reaches at time, t
$Q_h(x,y,z,t)$	Energy at (x,y,z) due to a single substrate heating event at time, t
$Q_T(x,y,z,t)$	Energy at (x,y,z) due to all previous substrate heating events
r	Distance between two locations
t	Time
t_d	Time for a draw operation
t_d	Time to travel a distance d
t_{ndx}	Time for an index operation
t_L	Time to draw a line
t_{End}	End time for a draw or index operation
t_{Start}	Start time for a draw or index operation
T_0	Room temperature
u	Velocity
V	Volume
W	Watt
x	Cartesian coordinate axis
$x(t)$	$x-$coordinate of the laser at any time
X	Dimension of the sample along the $x-$axis
y	Cartesian coordinate axis
$y(t)$	$y-$coordinate of the laser at any time
Y	Dimension of the sample along the $y-$axis
z	Cartesian coordinate axis, or deposited height, depending on context
$z(x,y,t)$	Deposition at a location

Greek Symbols	Explanation
d	Interval length used in the spatial deposition model
e	Absorptivity
k	Thermal diffusivity
mm	Micrometer
p	3.14159….
r	Density
ΔT	Temperature rise in the substrate at any location
ΔT_m	Difference between melting point and room temperature
ΔT_s	Temperature rise in the substrate
Δx	Hatch spacing

Prologue

This dissertation grew out of a 1998 DARPA grant awarded to Dr. Donald Ingber of Harvard University titled "*Biomimetic Materials for Pathogen Neutralization*". Dr. Ingber noticed that the mammalian cell wall contained certain geometric structures that imparted a high degree of flexibility and strength to the membrane. Other examples of regular, repeating structures were seen in the trabecular structure of mammalian bones, which provide a lightweight, porous, impact-resistant scaffold within which other biochemical processes can occur.

Reasoning that Nature had perfected these structures using brute-force methods over millions of years, Dr. Ingber started a company, Molecular Geodesics/Tensegra to develop the manufacturing methods required to create these structures. Research at Molecular Geodesics conducted in part by the author led to a hybrid injection molding/casting process to create these structures, albeit in the millimeter scale. A patent application "*Methods and Molds for Forming Complex Unitary Three-Dimensional Structures*" was filed based on this research.

The utility of the physical regularity of these biomimetic structures is dependent on their scale. In the millimeter scale, for example, having a regular structure is not any more useful than having an irregular structure. Therefore, materials with structural features in the millimeter scale are currently dominated by random metal foams, which can be inexpensively produced in bulk in a variety of materials or by anisotropic materials like honeycombs that can be extruded just as inexpensively. The research goal, therefore, became the reduction of the size of these biomimetic structures, to the point where their regular dimensions could be exploited, legitimizing their price premium. The process developed at Molecular Geodesics was inherently unsuited to building sub-millimeter scale geometries, so a search for candidate processes was initiated.

Laser Engineered Net Shaping, (LENS™), a solid freeform fabrication technology developed by Sandia National Laboratories, emerged as the most likely candidate. Though the process is currently capable of producing components in the millimeter scale, it was capable of doing so using recalcitrant but useful materials like titanium alloys.

Little published scientific literature on the process was available at that time, so users arrived at build parameters through trial and error. Plainly, this was not an acceptable method for the target applications of biomimetic structures. A process model that could relate deposition to build parameters was clearly necessary. This dissertation focuses on developing a process model for the LENS™ process, which could, perhaps, help create such complicated structures directly in metal.

1 Introduction

Laser Engineered Net Shaping (LENS™), is a direct metal deposition (DMD™) technology – a subset of solid freeform fabrication (SFF) technologies – and can create complex, three-dimensional (3D) geometries in metal using a layer-by-layer process. It is a nascent computer-aided manufacturing (CAM) process and can convert computer-aided designs (CAD) to metal prototypes in a matter of hours. Figure 1 shows an example of the kinds of unitary geometries that can be built using this process. A detailed overview of the LENS™ process is provided in the Appendices.

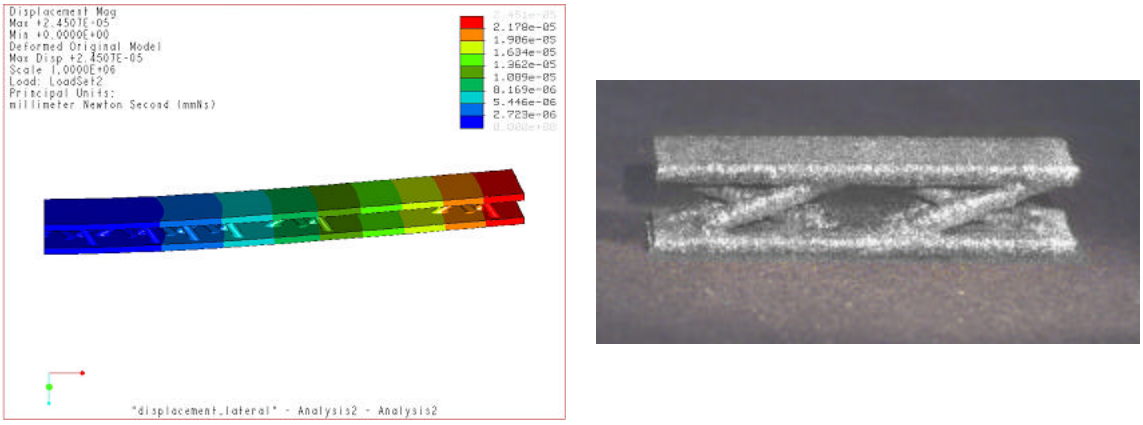

Figure 1: Complex design and LENS Ô prototype

Left: a complex geometry not manufacturable in a unitary form in titanium by conventional processing. Right: a LENS™ prototype of the design concept in titanium alloy obtained in 4 hours.

As with most new technologies, research has focused on sub-system development and on finding novel applications for the process. There has been little incentive to develop a process model, as it is possible to arrive at working build parameters with some trial and error and prior experience. The relatively high equipment cost and the relatively few machines in existence are other stumbling blocks. The inevitable result of this is a lack of published process research in this field.

Comparison of the LENS™ process to stereolithography, a close technological cousin, is less than flattering. The stereolithography process has found wide industrial acceptance and 3D Systems, the manufacturer of the equipment, has reported sales of $121M (3D Systems, 2001).

One reason for this acceptance is that stereolithography has been extensively researched and there are experimentally validated process models (Jacobs, 1992 and Jacobs, 1996) that relate process variables to ultimate dimensions. This has allowed relatively unskilled end-users to build complex geometries with ease, making the equipment attractive to purchasers. In contrast, the LENS™ process has been limited to research laboratories and universities, and only a few companies have purchased the equipment. The fact that acceptable LENS™ process models do not exist makes it nearly impossible to build consistent geometries and therefore hinder its market penetration.

1.1 Objectives

The goals of this dissertation are to

- Analyze the LENS™ equipment and process and identify key process parameters.
- Model energy and material delivery mechanisms.
- Model the average deposition and location-dependent deposition in a layer.
- Validate these models experimentally.

1.2 Rationale

Unlike stereolithography, which is limited to making plastic models, LENS™ can be used to fabricate metal objects directly, albeit at a relatively high cost. This opens up the tantalizing possibility of rapid-manufacturing custom metal components in low volumes – of special relevance to the aerospace, medical and casting industries, which often produce low volume, high value-added products. These are also industries that are particularly sensitive to failure; hence a sound understanding of the process is required before they can accept such a process even as a means of making prototypes. The availability of a robust process model therefore becomes a prerequisite to using LENS™ in mission-critical applications and could ultimately help transition it from a novel rapid prototyping method to a versatile, industrial rapid manufacturing process.

It seems logical that material deposition is caused by the interaction between the material and energy supplied. However, neither all the material nor all the energy supplied is available to the melt pool, making it difficult to predict how much will be deposited. Plainly, building uniform, identical layers is difficult without this knowledge, so models that can relate parameters to deposition would be useful.

One characteristic feature of layers built on the LENS™ machine using a serpentine raster pattern is the overheating of the edges, as the laser reverses direction. Models that incorporate the effect of substrate heating might be applied to predict the uneven deposition of material characteristic of the constant-energy, constant-velocity serpentine rastering pattern. This could provide the necessary tools to correct for spatial overheating by varying parameters in real time, resulting in more thermally uniform surfaces and, therefore, isotropic physical properties.

1.3 Literature Review

A series of papers describing the LENS™ process provide excellent process overviews and list compatible materials and their mechanical properties. Griffith (Griffith *et al*, 1996) and Mazumder (Mazumder *et al*, 1997) provide excellent process overviews of a variety of SFF processes and Sachs (Sachs, 2001) details the factors that need to be

overcome for them to mature into a manufacturing technology. Keicher (Keicher and Smugeresky, 1997) describes the process and provides physical properties of various stainless steels produced using it. He also relates the deposited volume to the power density. Arcella, in conjunction with Froes (Arcella and Froes, 2000, Froes, 2000) describes the Aeromet incarnation of the LENS™ process, which is primarily designed for high throughput applications. Froes (Froes, 2000) discusses the fatigue properties of aerospace components produced using Ti-6Al-4V and states that they overlap with conventional wrought and annealed samples. Gerekin (Gerekin, 1994) describes the process and its applications to the automotive industry and uses a cobalt alloy, Stellite 6, and a nickel alloy, Inconel-625, to produce thin-walled cylindrical components. Kobryn (Kobryn and Semiatin, 2001) studied the mechanical properties for Ti-6Al-4V, in particular, the tensile strength, fatigue and crack-growth resistance. They identified porosity elimination and microstructural control as being critical to the development of "good" mechanical properties and showed that the properties of LENS™-deposited Ti-6Al-4V could equal that of forged material.

Several researchers, chiefly at Sandia National Laboratories (SNL) and at Vanderbilt University, have studied the thermal effects during LENS™ processing. A lot of their research was published on the now defunct LENS™ Cooperative Research and Development Agreement (CRADA) website.

Griffith and coworkers at SNL undertook a huge study (Griffith *et al*, 2000) in which they measured the temperature distribution around the melt pool using thermal imaging and thermocouples. They used this information to calculate cooling rates, steady state temperature and the microstructure of the part being built. Their paper incorporated some of the data previously generated by Hofmeister using 316 stainless steel (Hofmeister *et al*, 1999). In a related study using similar techniques, Brooks and coworkers (Brooks *et al*, 1999 and Brooks *et al*, 2000) explained the types of novel microstructures that could be attained using 304L stainless steel based on the cooling rates the material experienced during processing. Ensz (Ensz, 2000) used thermocouples to calculate the "characteristic height" at which the thermal transients experienced by each layer becomes similar. He argued that above this height, there would be uniformity in microstructure and physical properties. In another paper (Ensz, 2000) published on the LENS™ CRADA, single line beads were made using combinations of parameters and empirical relations such as "velocity has a primary effect on bead height and little effect on pool diameter" were drawn.

Research on imposing a uniform thermal environment by the expedient of coupling thermal modeling with closed-loop control systems is just beginning. Doumanidis modeled the thermal fields in a process related to the LENS™ process which bonds thin layers of metal using a torch (Doumanidis, 1995). His work was aimed at providing the basis for future real-time controlling of the process to create uniform thermal fields. It may not be directly applicable as the temperature profiles due to a torch differ significantly from those due to a laser. Mazumder (Mazumder *et al*, 2000) do away with direct thermal modeling and use a "reflective topography technique" to control deposition volume in real time based on the measured deposition thickness. This technique

produces parts with far higher accuracy than was previously attained, but, unfortunately, can only respond after the uneven deposition has already occurred. It also relies on the measurement of thickness with moving sensors under low-light conditions – a technically difficult feat.

An early attempt to relate parameters to dimensions was carried out by Kummailil and coworkers at Tensegra, (Kummailil *et al*, 2000, Kummailil *et al*, 2001) who conducted a series of Placket-Burman studies to qualify the LENS™ process for manufacturing implantable medical devices. They derived an equation for cuboidal objects by relating the energy, the mass and the build parameters to the thickness of material deposited in a layer. Their final straight-line equation related *all* build parameters to final *z*-dimension by condensing them into a variable, ?, which was then used to determine the appropriate build parameters. Their equation allowed the operator to make changes to *any* build parameter, provided others were compensated to keep ? within range, allowing some degree of process control. The treatment was adequate for the particular application but incomplete, as it did not take into account either the laser attenuation due to particle scattering or the substrate heating by the laser.

Jacobs, (Jacobs, 2000) derived the "LENS™ Number", which is the ratio of the energy absorbed to the energy required to elevate the material in the melt pool to the melt pool temperature. Unfortunately, the melt pool temperature is, by definition, transient and the LENS™ number is essentially the process efficiency. Sample calculations show that the LENS™ number hovers around 10, indicating that the process is only 10% efficient at best, a fact that has been observed in practice. Pinkerton and Li (Pinkerton and Li, 2004) adapted the Hoffmeister energy balance model to single-wall builds in 2004, and were "able to improve build consistency" the month this dissertation was defended.

Though no further evidence of work relating parameters to dimensions was found in this literature review, research in related processes (laser cladding, sintering, welding and cutting) may be relevant. Boddu (Boddu *et al*, 2001) draws parallels between laser cladding and LENS™, indicating that process models that work for laser cladding should be equally applicable to LENS™. Schneider (Schneider, 1998) provides a detailed analysis of the laser-cladding process, and some of his experimental methods could be applicable to understanding the LENS™ process. Resch (Resch *et al*, 2001) conducted studies on the anisotropic physical properties of cobalt-based alloys built using a blown powder process and applied laser-cladding models to their research. They apply mass and energy balance models derived by Kaplan (Kaplan, 2000) and find good correlation in their experiments.

Several papers in the field of laser welding (Nguyen *et al*, 1999, Gorka, 2000; Rostami and Raisi, 1997) provide a wealth of information regarding thermal fields around a moving heat source based on the original Carslaw (Carslaw and Jaeger, 1965) moving heat source analysis. They provide analytical solutions for heat sources with disc, Gaussian and double-ellipsoidal power distributions, which can be used to refine the models based on point source analysis,.

A series of papers (Nickel, 1999, Nickel *et al* 2001, Li *et al*, 2000) modeled the thermal stresses created by the laser and the shape (Amon *et al*, 1993) of the melt pool in the selective laser sintering process. The papers focus on predicting thermal stress-induced warping in an attempt to improve part accuracy. Since warping has been widely observed in this process, keeping the thermal stresses below critical values by judicious choice of build parameters will improve part accuracy.

1.4 Approach

This study has four thrust areas, listed below:

- Design Review
- Modeling
- Experimentation
- Verification

The design review was performed to establish process capabilities based on the design of the equipment. The technique of functional decomposition was borrowed from the field of Axiomatic Design to accomplish this. The variables that affect deposition were segregated based on the degree of control the LENS™ equipment offered over them. The level of control over key process variables helped identify a realistic backdrop against which to test the models.

A material delivery model was developed by relating the mass flow rate and the mass available for deposition based on the path of the laser as it traversed a rectangular layer.

An energy delivery model called the "Average Deposition Model" was developed, which assumes that all the absorbed energy is used to deposit material and therefore neglects substrate heating. It was expected to perform best for builds that were massive relative to the substrate and least well near the edges of the build that are known to be subjected to overheating. A second energy delivery model called the "Spatial Deposition Model" was developed, incorporating substrate heating using the Carslaw Equation for an instantaneous point source of heat. This model can be used for any build, but is best used on smaller builds in which the substrate varies, justifying the computation required.

Experiments were carried out to test these models. One set of experiments was designed to be "isothermal". A single layer was built on a substrate that was approximately 74,000 times larger than the amount deposited. A second set of experiments was designed to study substrate heating by building a second layer over the first. Single line tests were conducted to expand the range of parameters to span the working range of the equipment.

2 Functional Decomposition of Equipment Design

2.1 Introduction

This section adapts the technique of functional decomposition – originally developed by Suh (Suh, 1990, Suh, 2001) for Axiomatic Design – to perform a design review on the LENS™ process.

In axiomatic design theory, a design consists of several domains, three of which are the functional, the physical and the process domain. The functional domain consists of "functional requirements" (FR), the physical domain consists of "design parameters" (DP) and the process domain consists of "process variables" (PV). Functional requirements are requirements that the design must satisfy to be considered "good". In this adaptation of the technique, design parameters are the components on the machine that satisfy these requirements. Process variables are the physical characteristics that enable the design element to satisfy the design requirement. Suh suggests that these (and other) domains can be related via mathematical mapping, aiding designers in the process of design.

Functional decomposition generates what is essentially a hierarchical list, and can be applied to any domain. When applied to the functional domain, a top-level functional requirement can be subdivided into lower-level requirements. For example, the requirement of "providing motion in the horizontal plane" can be broken into "provide motion in the x-direction", "provide motion in the y-direction" and "connect components that provide motion". The corresponding design elements would be the "x-stage", the "y-stage" and the "fixture connecting the x-stage and y-stage". Thus, functional decomposition provides a direct link between a functional requirement for the design and the design element on the machine that "satisfies" the requirement. The process lends itself to recursion and can be carried out until further subdivision becomes meaningless.

The technique of functional decomposition is best performed during the design phase to ensure that the functional requirements of the design are fulfilled. Since the designer's intent when designing the LENS™ machine is not known, plausible functional requirements (uses) are assigned to the existing design parameters, (components); essentially reverse engineering the machine. In one sense, the functional requirements of the LENS™ process are immaterial: the design parameters determine the functions the machine can perform.

First, existing design elements are functionally decomposed through progressively lower levels of hierarchy. Plausible functional requirements are generated for each of these

design elements. Next, process variables are assigned based on applicable principles of engineering and physics. For example, if the design element is a "rubber gasket", and the functional requirement is to "provide a seal against air", the process variable is the "compliance of the gasket material". Finally, the list of process variables obtained by this method is compared with those known to affect deposition, to establish the process limits of the machine.

As Suh suggests in one of his axioms, coupling between functional requirements and design elements results in a less efficient design. The example often used to illustrate coupling is hot and cold water faucets, in which changing temperature also changes the flow rate. The functional requirements of temperature and flow are "coupled". This study identifies regions of coupling on the LENS™ machine and discusses the effect of coupling on the LENS™ process.

2.2 Design Elements and Tables

The LENS™ machine consists of several sub-systems (high-level design parameters), each of which can be recursively broken down to the leaf-level of simplicity. The high level design parameters are called design elements and are shown in the design tables.

This study starts with design parameters (physical components of the machine) and decomposes them to leaf-level simplicity. At each level, the functional requirements are determined based on the capabilities of the design parameters identified. In short, the equipment is reverse engineered. The only exception to this approach was determining the top-level functional requirement, which is not negotiable: the LENS™ machine *must* be able to create and fuse a 2-dimensional metal layer to a substrate.

The tables shown at the end of this section represent the design parameters and the associated functional requirements. They show any coupling that occurs within the design parameter, but cannot show inter-design parameter coupling, which will be shown in section 2.4.

2.2.1 FR1: Provide Motion

An elementary requirement of any selective deposition process is to provide motion. The motion must be in orthogonal directions and is achieved using orthogonally oriented stages. The stages are attached to each other to provide simultaneous motion. One disadvantage of this system is that the weight of the stages contributes to the inertia of the system and hence makes near-instantaneous starts and stops impossible. This affects energy input when the stages accelerate, decelerate, and consequently affects the part accuracy. The requirements of the stage are identical, irrespective of the direction they are oriented, so the functional decomposition of the stage in the y-direction is identical to the functional decomposition of the stage in the x-direction.

Table 1: FR-DP design table for FR1: provide motion

shows the FR-DP design table for the first functional requirement, showing the coupling between the elements. The diagonal squares are necessarily coupled, but the design reveals that the individual components of the stage are coupled with each other. For example, the variable potentiometer is of no use without a stepper motor, and neither design parameter is of any use without the lead screw required to move the stages. This implies that the stages should be considered a leaf-level unit and not decomposed further. The decomposition of the motion requirement was stopped at this stage so that the analysis reflected the design of the LENS™ machine and not the design of the stage.

The stages are coupled with other functional requirements, but a table format does not reveal such coupling at this level of detail. The coupling between the stages and other functional requirements is shown in section 2.4.

FR-DP	1 LENS® machine.	□1.1 Orthogonal stages	□□1.1.1 X-Stage	□□□1.1.1.1 Stepper motor	□□□1.1.1.2 Variable potentiometer	□□□1.1.1.3 Lead screw	□□□1.1.1.4 Software	□□1.1.2 Y-Stage	□□□1.1.2.1 Stepper motor	□□□1.1.2.2 Variable potentiometer	□□□1.1.2.3 Lead screw	□□□1.1.2.4 Software
1 Create and fuse a 2-D metal layer to a substrate		0	0	0	0	0	0	0	0	0	0	0
□1.1 Provide movement in horizontal plane	0		0	0	0	0	0	0	0	0	0	0
□□1.1.1 Provide movement in X-direction	0	0		1	1	1	1	0	0	0	0	0
□□□1.1.1.1 Move workpiece	0	0	1		1	1	1	0	0	0	0	0
□□□1.1.1.2 Control workpiece velocity	0	0	1	1		1	1	0	0	0	0	0
□□□1.1.1.3 Provide positional accuracy of 0.002"	0	0	1	1	1		1	0	0	0	0	0
□□□1.1.1.4 Provide method of triggering movement	0	0	1	1	1	1		0	0	0	0	0
□□1.1.2 Provide movement in the Y-direction	0	0	0	0	0	0	0		1	1	1	1
□□□1.1.2.1 Move workpiece	0	0	0	0	0	0	0	1		1	1	1
□□□1.1.2.2 Control workpiece velocity	0	0	0	0	0	0	0	1	1		1	1
□□□1.1.2.3 Provide positional accuracy of 0.002"	0	0	0	0	0	0	0	1	1	1		1
□□□1.1.2.4 Provide method of triggering movement	0	0	0	0	0	0	0	1	1	1	1	

Table 1: FR-DP design table for FR1: provide motion

The individual components of the stage are coupled with each other, indicating that the stage itself is at a leaf-level of decomposition.

2.2.2 FR2: Provide Material

The next top-level functional requirement is to provide material to the workpiece. This allows the deposition of material at locations where the material and the energy intersect. Material must be stored under inert gas in order to prevent oxidation. The gas must flow

into the chamber as the powder is being used up to avoid creating a pressure differential. The storage chamber for the powder therefore requires a bleed valve that controls the gas flow into it. Additionally, the powder must be moved from the store location to the powder head, and then focused onto the substrate, so the mechanisms that achieve this must physically lie within the chamber.

FR-DP	1.2 Powder delivery system	1.2.1 Powder storage container	1.2.1.1 Lid	1.2.1.2 Nitrile rubber gasket	1.2.1.3 Transparent window	1.2.1.4 Bleed valve connected to inert gas	1.2.2 Conveying mechanism	1.2.2.1 Rotating perforated disc	1.2.2.1.1 Stepper motor	1.2.2.1.2 Variable potentiometer	1.2.2.1.3 Perforations	1.2.2.1.4 Powder pick up capacity	1.2.2.2 Pneumatic system	1.2.2.2.1 Gas delivery system	1.2.2.2.1.1 Gas control valve	1.2.2.2.2 Tubular pathway	1.2.2.2.3 Gas	1.2.2.2.4 Gas recirculating system	1.2.2.2.4.1 Damper	1.2.2.2.4.2 Porous filter	1.2.2.2.4.3 Tubes	1.2.2.2.4.4 Compressor	1.2.3 Powder delivery head	1.2.3.1 Radial flow splitting channels	1.2.3.2 Nozzles
1.2 Provide material to workpiece		0	0	0	0	0	0	0	0	0	0	0	0	0	0	0	0	0	0	0	0	0	0	0	0
1.2.1 Provide location to store powder	0		0	0	0	0	0	0	0	0	0	0	0	0	0	0	0	0	0	0	0	0	0	0	0
1.2.1.1 Allow addition of powder	0	0		0	0	0	0	0	0	0	0	0	0	0	0	0	0	0	0	0	0	0	0	0	0
1.2.1.2 Provide seal against air	0	0	0		0	0	0	0	0	0	0	0	0	0	0	0	0	0	0	0	0	0	0	0	0
1.2.1.3 Show powder level	0	0	0	0		0	0	0	0	0	0	0	0	0	0	0	0	0	0	0	0	0	0	0	0
1.2.1.4 Maintain constant pressure	0	0	0	0	0		0	0	0	0	0	0	0	0	0	0	0	0	0	0	0	0	0	0	0
1.2.2 Move powder from store to workpiece	0	0	0	0	0	0		0	0	0	0	0	0	0	0	0	0	0	0	0	0	0	0	0	0
1.2.2.1 Provide method of picking up powder	0	0	0	0	0	0	0		0	0	0	0	0	0	0	0	0	0	0	0	0	0	0	0	0
1.2.2.1.1 Provide rotation	0	0	0	0	0	0	0	0		0	0	0	0	0	0	0	0	0	0	0	0	0	0	0	0
1.2.2.1.2 Control rotation	0	0	0	0	0	0	0	0	0		0	0	0	0	0	0	0	0	0	0	0	0	0	0	0
1.2.2.1.3 Geometric feature that can hold powder	0	0	0	0	0	0	0	0	0	0		0	0	0	0	0	0	0	0	0	0	0	0	0	0
1.2.2.1.4 Provide capacity of at least x g.s-'	0	0	0	0	0	0	0	0	0	0	0		0	0	0	0	0	0	0	0	0	0	0	0	0
1.2.2.2 Impart kinetic energy to powder	0	0	0	0	0	0	0	0	0	0	0	0		0	0	0	0	0	0	0	0	0	0	0	0
1.2.2.2.1 Control powder mass flow rate	0	0	0	0	0	0	0	0	0	0	0	0	0		0	0	0	0	0	0	0	0	0	0	0
1.2.2.2.1.1 Control gas flow rate	0	0	0	0	0	0	0	0	0	0	0	0	0	0		0	0	0	0	0	0	0	0	0	0
1.2.2.2.2 Provide a pathway for powder	0	0	0	0	0	0	0	0	0	0	0	0	0	0	0		0	0	0	0	0	0	0	0	0
1.2.2.2.3 Must be inert to metal being processed [C]	0	0	0	0	0	0	0	0	0	0	0	0	0	0	0	0		0	0	0	0	0	0	0	0
1.2.2.2.4 Keep pressure in chambre constant	0	0	0	0	0	0	0	0	0	0	0	0	0	0	0	0	0		0	0	0	0	0	0	0
1.2.2.2.4.1 Prevent pressure spikes	0	0	0	0	0	0	0	0	0	0	0	0	0	0	0	0	0	0		0	0	0	0	0	0
1.2.2.2.4.2 Prevent powder from entering the system	0	0	0	0	0	0	0	0	0	0	0	0	0	0	0	0	0	0	0		0	0	0	0	0
1.2.2.2.4.3 Provide path to recirculate gas	0	0	0	0	0	0	0	0	0	0	0	0	0	0	0	0	0	0	0	0		0	0	0	0
1.2.2.2.4.4 Repressurize gas	0	0	0	0	0	0	0	0	0	0	0	0	0	0	0	0	0	0	0	0	0		0	0	0
1.2.3 Deliver powder to workpiece	0	0	0	0	0	0	0	0	0	0	0	0	1	1	1	0	0	0	0	0	0	0	0		0	0
1.2.3.1 Distribute powders radially	0	0	0	0	0	0	0	0	0	0	0	0	0	0	0	0	0	0	0	0	0	0	0	0	
1.2.3.2 Focus powders onto moulten spot	0	0	0	0	0	0	0	0	0	0	0	0	1	1	1	0	0	0	0	0	0	0	0	0	

Table 2: FR-DP design table for FR2: provide material

The pneumatic system used to impart kinetic energy to the powder affects the focusing of the powder on the workpiece.

Powder is picked up by a rotating disc containing radial perforations in which powder gets trapped as the disc rotates. The perforations move pass a stream of inert carrier gas, which blows them into a tube. The carrier gas has two functions: it imparts kinetic energy to the powders and controls the amount of powders being moved. Increasing the volumetric flow rate of the gas increases the amount of powder blown through the tube. An alternate way of increasing the mass of powders being carried is by increasing the rpm of the rotating disc, which increases the amount of powder picked up and delivered to the gas stream.

The powders are carried by the inert carrier gas and moved through tubes to the powder delivery head, which must distribute them radially in order to keep the build even. Uneven radial distribution of material will cause higher deposition every time the laser moves in the direction of higher material density, leading to uneven builds. The powder delivery head must evenly distribute the turbulent powder flow into four tubes leading to the nozzles. Perpendicular flow-splitting tubes that lead to four nozzles are used to achieve this. The nozzles are aimed at the melt pool and direct the powders to the substrate.

The areas in which this design parameter is coupled are highlighted in Table 2. The pneumatic system that is used to impart kinetic energy to the powder affects its focus. At extremely low powder flow rates, for example, the powders exit the nozzles with such low kinetic energy that they may not reach the melt pool. The powder delivery system is also coupled with other functional requirements, but the coupling is not visible at this level of detail. A more comprehensive table in the Design Matrices section shows the coupling between the powder delivery system and other high-level functional requirements.

2.2.3 FR3: Provide Energy

Energy is required to melt the material supplied to the workpiece. The energy must be focused to increase the build resolution. The system uses a laser to provide the energy, so all lower level functional requirements are constrained by this design choice. The energy supplied is coherent because a laser is used to generate it. Since different materials have different absorptivities, the energy must be controllable. A variable potentiometer is used to control the current to the laser.

A pathway to transmit the energy to the substrate is provided by a fiber optic cable. The fibers are shielded to protect them from heat and lead to an optical lens. The optical lens must be movable in order to keep the laser focused on the substrate and is attached to a z-stage. Table 3 shows the design tables for the energy delivery system.

The next section provides hierarchical information using screen-shots from software developed for this research.

FR-DP	1.3 Energy delivery system	1.3.1 CO2 Laser	1.3.1.1 Electron gun	1.3.1.2 CO2 gas	1.3.1.3 Resonating chambre	1.3.1.4 Reflecting mirror	1.3.2 Electric power control system	1.3.2.1 Variable potentiometer	1.3.3 Energy transmission system	1.3.3.1 Fibre-optic cable	1.3.3.1.1 Parallel fibres	1.3.3.1.2 Opaque sheath	1.3.3.1.3 Sheath material	1.3.3.2 Shutter mechanism	1.3.3.2.1 Shutter	1.3.3.2.2 Shutter activating mechanism	1.3.3.2.3 Black hole	1.3.4 Laser focusing system	1.3.4.1 Optical lens mount	1.3.4.1.1 Central purge system	1.3.4.1.1.1 Gas barrier	1.3.4.1.2 Optical lens	1.3.4.1.3 Z-stage	1.3.4.1.3.1 Stepper motor	1.3.4.1.3.2 Variable potentiometer	1.3.4.1.3.3 Lead screw	1.3.4.1.3.4 Software
1.3 Provide energy to workpiece		0	0	0	0	0	0	0	0	0	0	0	0	0	0	0	0	0	0	0	0	0	0	0	0	0	0
1.3.1 Create coherent energy	0		0	0	0	0	0	0	0	0	0	0	0	0	0	0	0	0	0	0	0	0	0	0	0	0	0
1.3.1.1 Provide energy to electron source	0	0		0	0	0	0	0	0	0	0	0	0	0	0	0	0	0	0	0	0	0	0	0	0	0	0
1.3.1.2 Generate coherent laser beam	0	0	0		0	0	0	0	0	0	0	0	0	0	0	0	0	0	0	0	0	0	0	0	0	0	0
1.3.1.3 Contain generated energy	0	0	0	0		0	0	0	0	0	0	0	0	0	0	0	0	0	0	0	0	0	0	0	0	0	0
1.3.1.4 Amplify generated energy	0	0	0	0	0		0	0	0	0	0	0	0	0	0	0	0	0	0	0	0	0	0	0	0	0	0
1.3.2 Control energy	0	0	0	0	0	0		0	0	0	0	0	0	0	0	0	0	0	0	0	0	0	0	0	0	0	0
1.3.2.1 Adjust input current	0	0	0	0	0	0	0		0	0	0	0	0	0	0	0	0	0	0	0	0	0	0	0	0	0	0	0
1.3.3 Transmit energy	0	0	0	0	0	0	0	0		0	0	0	0	0	0	0	0	0	0	0	0	0	0	0	0	0	0	0
1.3.3.1 Provide pathway for light	0	0	0	0	0	0	0	0	0		0	0	0	0	0	0	0	0	0	0	0	0	0	0	0	0	0	0
1.3.3.1.1 Transmit light	0	0	0	0	0	0	0	0	0	0		0	0	0	0	0	0	0	0	0	0	0	0	0	0	0	0	0
1.3.3.1.2 Prevent leakage of light	0	0	0	0	0	0	0	0	0	0	0		0	0	0	0	0	0	0	0	0	0	0	0	0	0	0	0
1.3.3.1.3 Resist heat	0	0	0	0	0	0	0	0	0	0	0	0		0	0	0	0	0	0	0	0	0	0	0	0	0	0	0
1.3.3.2 Control energy pathway	0	0	0	0	0	0	0	0	0	0	0	0	0		0	0	0	0	0	0	0	0	0	0	0	0	0	0
1.3.3.2.1 Open/close pathway	0	0	0	0	0	0	0	0	0	0	0	0	0	0		0	0	0	0	0	0	0	0	0	0	0	0	0
1.3.3.2.2 Switch from open to close	0	0	0	0	0	0	0	0	0	0	0	0	0	0	0		0	0	0	0	0	0	0	0	0	0	0	0
1.3.3.2.3 Trap energy when closed	0	0	0	0	0	0	0	0	0	0	0	0	0	0	0	0		0	0	0	0	0	0	0	0	0	0	0
1.3.4 Deliver energy	0	0	0	0	0	0	0	0	0	0	0	0	0	0	0	0	0		0	0	0	0	0	0	0	0	0	0
1.3.4.1 Focus energy on workpiece	0	0	0	0	0	0	0	0	0	0	0	0	0	0	0	0	0	0		0	0	0	0	0	0	0	0	0
1.3.4.1.1 Protect lens from powders	0	0	0	0	0	0	0	0	0	0	0	0	0	0	0	0	0	0	0		0	0	0	0	0	0	0	0
1.3.4.1.1.1 Maintain cleanliness of lens	0	0	0	0	0	0	0	0	0	0	0	0	0	0	0	0	0	0	0	0		0	0	0	0	0	0	0
1.3.4.1.2 Focusing Element	0	0	0	0	0	0	0	0	0	0	0	0	0	0	0	0	0	0	0	0	0		0	0	0	0	0	0
1.3.4.1.3 Keep workpiece at focal length	0	0	0	0	0	0	0	0	0	0	0	0	0	0	0	0	0	0	0	0	0	0		0	0	0	0	0
1.3.4.1.3.1 Move workpiece in Z-direction	0	0	0	0	0	0	0	0	0	0	0	0	0	0	0	0	0	0	0	0	0	0	0		0	0	0	0
1.3.4.1.3.2 Control workpiece velocity	0	0	0	0	0	0	0	0	0	0	0	0	0	0	0	0	0	0	0	0	0	0	0	0		0	0	0
1.3.4.1.3.3 Positional accuracy of 0.002"	0	0	0	0	0	0	0	0	0	0	0	0	0	0	0	0	0	0	0	0	0	0	0	0	0		0	0
1.3.4.1.3.4 Provide method of triggering movement	0	0	0	0	0	0	0	0	0	0	0	0	0	0	0	0	0	0	0	0	0	0	0	0	0	0		0

Table 3: FR-DP design table for FR3: provide energy

Energy is delivered using a laser. At this level of decomposition, there is no coupling.

2.3 Design Hierarchy

Tabular representation of data is ideal for two-dimensional data. This study has created hierarchical data that cannot be easily represented using tables. Since commercially available software designed to represent hierarchical relationships was not available at the time of writing, rudimentary software tools were created for the purpose. The software represents data in a more intuitive tree-format. Branches of the trees may be opened to show items of interest or collapsed to hide items that clutter the issue. Since the branches are indented, the level of the data and its relationship to other elements are visible simultaneously.

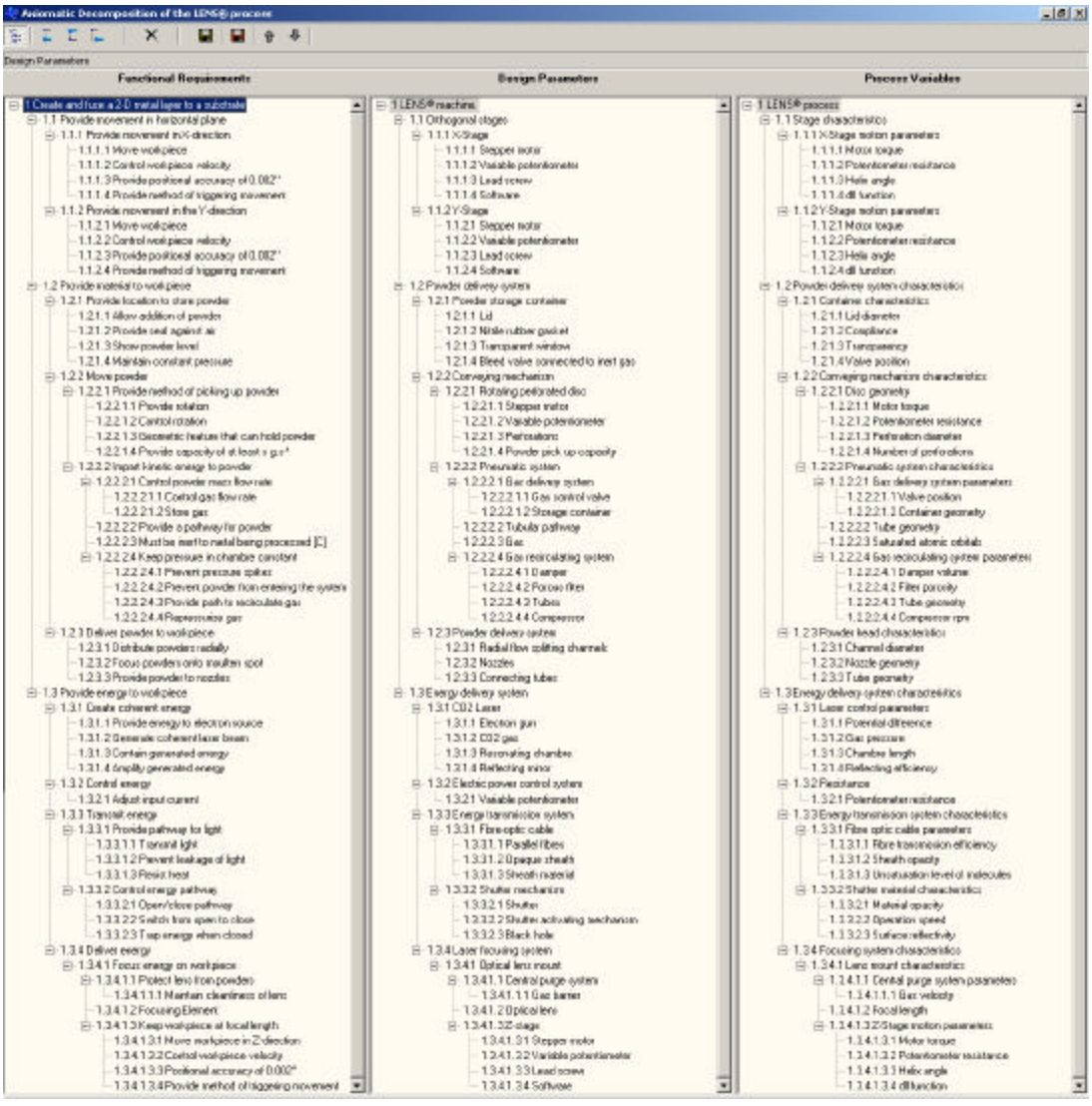

Figure 2: Complete FR-DP-PV hierarchy for the LENS Ô process

The figure shows a screen shot of the software developed for this project. The tree-view represents data hierarchically. The tree-views are coupled, so an operation on one is reflected in the others.

Figure 2 shows the hierarchical decomposition using the developed software. The figure shows all nodes expanded, but the software allows individual nodes to be opened and closed and automatically opens and closes associated nodes in the heirarchy. The following paragraphs discuss the heirarchy in more detail.

2.3.1 Level 0:

The top-level functional requirement of the LENS™ machine is to create and fuse a 2-dimensional metal layer to a substrate. The corresponding design parameter is the LENS™ machine and the process variable is the LENS™ process.

2.3.2 Level 1:

This and succeeding levels study the design parameters first, find appropriate functional requirements based on the capability of the design element and then identify process variables from the physics or engineering principles behind the design element. Figure 5 shows the level-1 decomposition of the LENS™ equipment. The major design parameters are the orthogonal stages, the powder delivery system and the energy delivery system. The functional requirements of these design parameters are to provide motion in the horizontal plane, provide material to the workpiece and to provide energy to the workpiece respectively. The process variables that control how this happens are the characteristics of the stages, the powder delivery system and the energy delivery system, respectively.

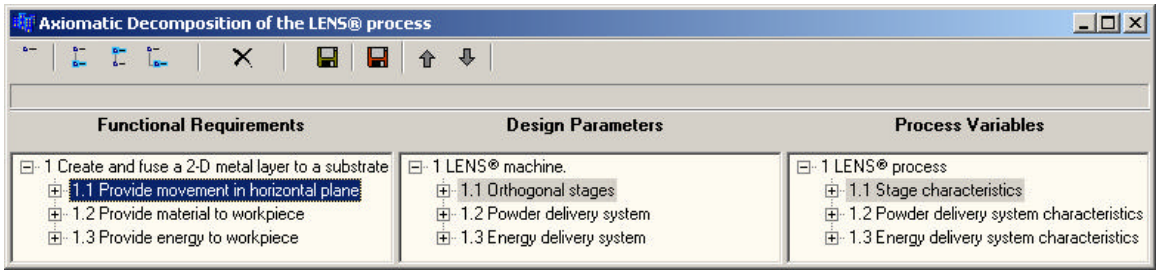

Figure 3: Level-1 functional decomposition of the LENS™ equipment

A screen shot, showing the level-1 FR-DP-PV relationship for the LENSÔ process.

2.3.3 Level 2:

Figure 6 shows the level-2 decomposition of the LENS™ equipment. Decomposition of the stages is relatively simple – two stages are required, one moving in the x-direction and another moving in the y-direction. The process variables are the parameters that

control them. The powder delivery system may be broken down into a storage location, a conveying system and a delivery system for the powder. The storage location allows quantities of powder to be stored locally, enabling the machine to build large components. The conveying mechanism provides a means of transporting the powder to the head and the delivery mechanism allows the powders to reach the melt pool. The energy delivery system is composed of a CO_2 laser, a control system that regulates the current the laser receives, a pathway for the energy to reach the substrate and a focusing system, to direct the energy to the substrate surface.

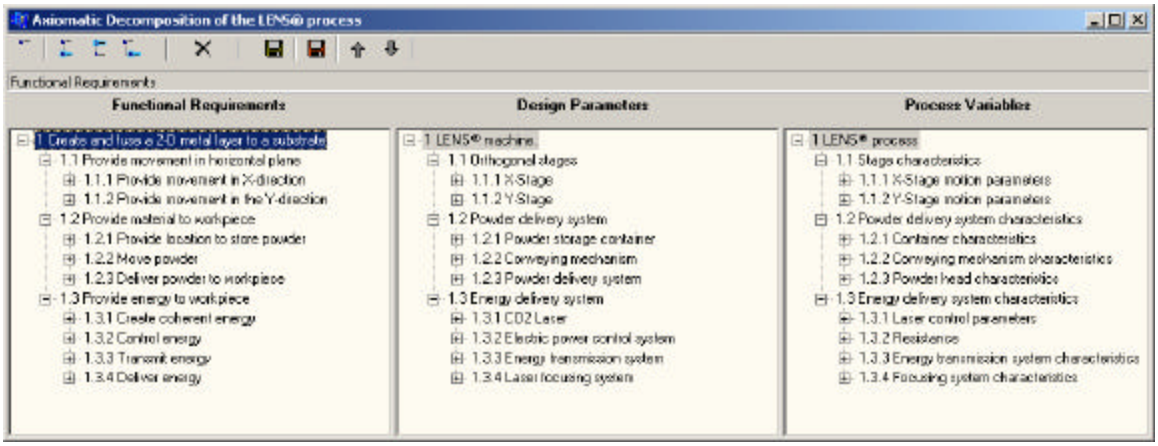

Figure 4: Level-2 functional decomposition of the LENS™ equipment

The figure shows a screen-shot, showing the level-2 FR-DP-PV relationships for the LENSÔ process.

2.3.4 Level 3:

The level-3 decomposition represents the leaf-level of decomposition for the stages. The stages are composed of a stepper motor, a variable potentiometer, a lead screw and a software function that provides a trigger for the motion. The stepper motor is required to move the stage. The variable potentiometer is used to control the workpiece velocity. The lead screw determines how far the stages move and the software function determines when the stages move. The process variable for the stepper motor is the motor torque, which determines how much of a load the motor is capable of moving. The potentiometer resistance determines how much power is supplied to the motor and how fast the stage moves. The helix angle of the lead screw determines stage velocity.

The powder storage container has a lid to allow the operator to add material, a window, to allow the operator to see how much material is present, a gasket, to provide a seal against air, and a bleed valve to provide inert gas to replace the volume of powder removed during machine operation. The compliance of the gasket determines how efficiently it seals, while the position of the bleed valve determines how well the internal pressure is maintained constant. The powder conveying mechanism must provide a means of picking up the powder and a means of imparting kinetic energy to it. The powder

delivery system must distribute the powders radially around the melt pool, focus the powders on the melt pool and provide a method of bringing the powder to the focusing mechanism.

The laser is made up of an electron gun, which energizes CO_2 gas in a resonating chamber that has a reflecting mirror at either end. The power control system has a variable potentiometer that controls the energy provided to the laser and hence the power of the laser. As a potential difference is applied across the electron gun, electrons are emitted. The electrons excite the CO_2 gas to a higher energy state from which they descend to the ground state, emitting energy. This energy excites other molecules and the process repeats. After all the molecules have reached the excited state, the energy released is reflected off the mirrors. The mirrors are spaced at an integral multiple of the wavelength of the radiation and resonance conditions are quickly reached. The energy begins to leave the chamber through a small window coupled to a flexible fiber-optic cable, which directs the radiation to the optical lens, by total internal reflection. The fiber-optic cable is gated by a shutter, which controls whether or not the radiation is allowed to interact with the workpiece. The focusing system has an optical mount that focuses energy on the workpiece.

2.3.5 Level 4:

The rotating perforated disc used to pick up the powder is decomposed further at this level. It requires a stepper motor to rotate it, a variable potentiometer to control the rpm, a geometric feature (the perforations) to hold powders, and enough of these geometric features to provide the required powder delivery capacity. The pneumatic system that is used to impart kinetic energy to the powders can also be decomposed at this level. It requires a gas delivery system, a tubular pathway, a carrier gas and a recirculating system to maintain the pressure of the chamber constant. The fiber-optic cable, which forms part of the energy delivery system, can be decomposed further. It has parallel fibers to increase the flexibility of the cable, an opaque sheath so radiation is not lost and can resist heat. The shutter is opaque to the radiation, is able to switch from open to closed, and has an energy sink (a black hole) to dissipate the energy when the shutter is closed. The optical lens mount has several purposes. It holds the optical lens and protects it from flying powders and splashing molten fluid. It is movable in the z-direction to keep the workpiece at the focal length of the optical lens. The central purge system protects the optical lens from damage and the z-stage provides vertical motion.

2.3.6 Level 5:

The gas delivery system used to control the mass flow rate of the powders has a storage container for the gas and a gas control valve to control the volumetric flow rate of the gas. The gas re-circulating system has a damper to prevent pressure spikes, a porous filter to prevent powder from entering the system, and a compressor to re-pressurize the gas. The central purge system can also be decomposed at this level. Its primary

requirement is to protect the optical lens from powders, and it uses a stream of inert gas to achieve this goal. The z-stage can be decomposed exactly as the orthogonal stages discussed previously.

Section 2.4 contains the design matrix that shows the complete FR-DP functional decomposition of the LENS™ process. Diagonal cells are coupled because the design parameter satisfies the corresponding functional requirement. The off-diagonal coupled regions are highlighted and will be explained in detail.

2.4 Design Matrices

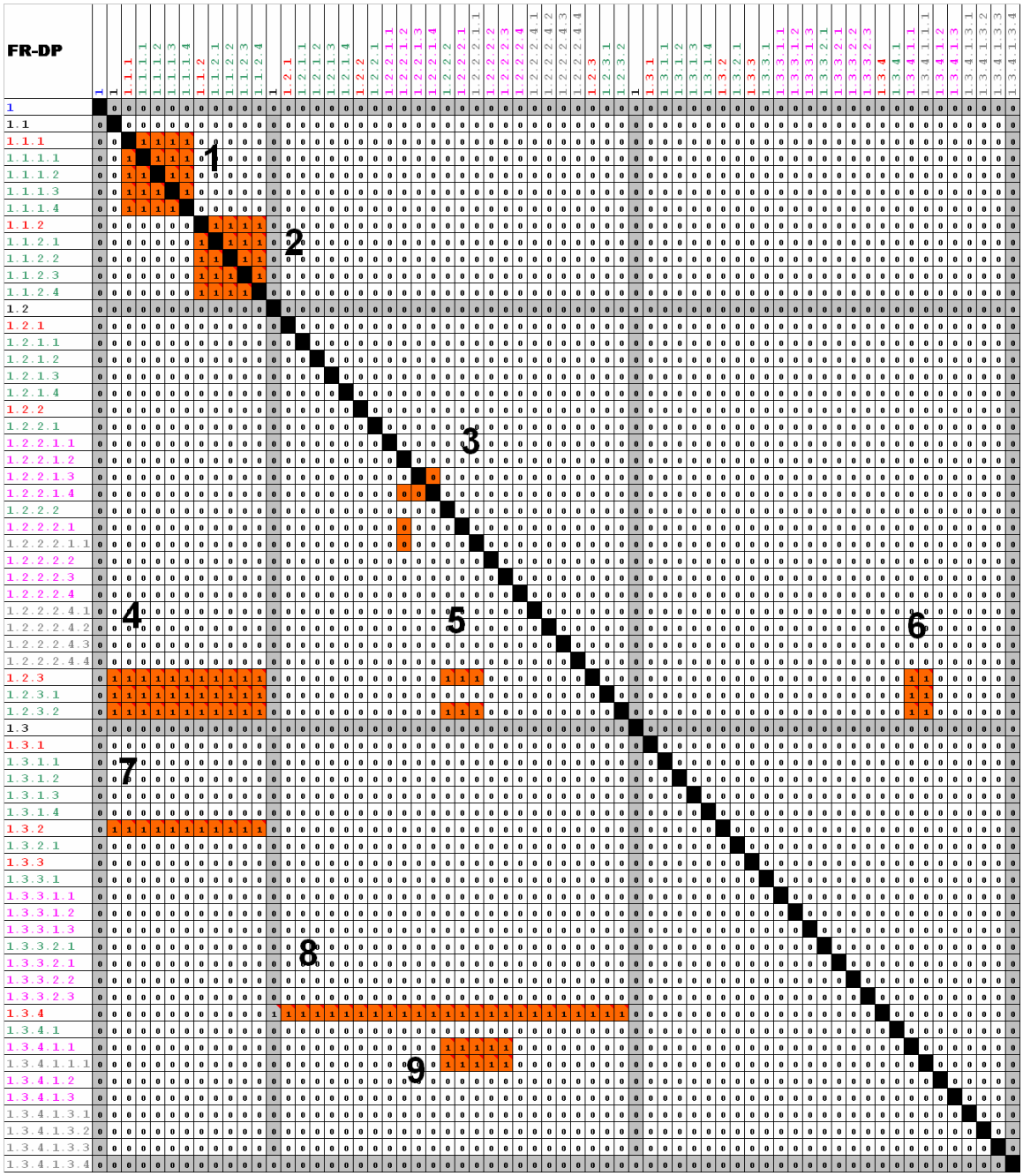

Table 4: The complete FR-DP matrix for the LENS Ô process

This figure is intended to show the coupling between the various systems in the LENS™ equipment. Coupled regions are discussed in detail later. The DP-PV matrix is identical to this figure and has not been shown.

2.5 Coupled Matrix Elements

The coupled regions of the FR-DP design matrix are numbered for convenience and discussed in the next few paragraphs.

2.5.1 Regions 1 & 2: Stages

The coupling in this region occurs because the stage is of no use without all its constituent components. In essence, the stage itself is a leaf-level node and further functional decomposition is pointless.

2.5.2 Region 3: Powder carrier – gas flow rate

The coupling in this region occurs because of the method of picking up powder. Since powders must collect in perforations on a disc, the gas flow rate is affected, as the perforations and powders block its flow.

2.5.3 Region 4: Stage motion – powder focal point

It is not immediately apparent that the motion of the head relative to the workpiece should affect the distribution of powders around the melt pool, but this is indeed the case. Assume that the powders have attained a steady state flow focused on the substrate before the stages start moving. When the stages move, they accelerate as fast as possible to reach the desired velocity. Due to inertia, the powder stream can behave like a curtain and billows in the direction opposite the stage motion. The process is reversed when the stages stop, effectively varying the material available at the start and the end of lines.

Coupling can be avoided by moving the component instead of the laser head, though this solution may be impractical when building components larger than the laser head.

2.5.4 Region 5: Carrier gas flow rate – powder focal point

Coupling between the carrier gas and the powder focal point occurs because the inert gas imparts kinetic energy to the powders. At extremely low carrier gas flow rates, the powders have such low momentum that they fail to reach the melt pool. Therefore, the carrier gas flow rate is coupled with the delivery of the powder to the melt pool.

2.5.5 Region 6: Center purge system – powder focal point

The center purge is a stream of inert gas that travels along the path of the radiation, keeping powders from bouncing vertically and damaging the optical lens. Since the center purge provides a net downwards force, it forces the powders away from the focal point. This is an inherently coupled system, since powders need a minimum kinetic energy to reach the melt pool.

2.5.6 Region 7: Stage motion – laser energy

The motion of the stages necessarily affects the amount of energy available to the sample. The faster the stages move, the less time a particular point is exposed to the radiation.

2.5.7 Region 8: Powder delivery – laser energy

Powders partially obscure the laser as they approach the melt pool. Even when tightly focused using nozzles, they bounce off each other, and their path quickly becomes unpredictable. Some fraction of the powders travels through the path of the laser and dissipate energy by melting, or by reflecting the energy. According to other researchers (Schneider, 1998), this effect is marginal and accounts for only 2-5% of the laser energy.

2.5.8 Region 9: Powder kinetic energy – lens cleanliness

The kinetic energy of the powders is sometimes enough to let them bounce off the substrate surface and impinge on the optical lens, which can damage its coating. Sometimes, powder particles splash into the melt pool with sufficient kinetic energy to drive molten drops of metal upward. In some cases, these droplets have enough kinetic energy to reach the lens before they solidify. In such instances, they stick to the lens, obscuring the laser energy and damaging the surface. Since delivering powder to the melt pool this way requires the particles to move fast as they leave the nozzles, the functional requirement of optical lens cleanliness is coupled to powder delivery.

2.6 Controlled and Uncontrolled Variables

The functional decomposition carried out on the equipment design shows that three major systems on the machine providing motion, material and energy are coupled. Coupling is not always bad – coupling between the laser and the powders is a necessary condition for material deposition. In this section, process variables in the design hierarchy are compared to those known to affect deposition and classified according to the level of control imposed on them in Figure 8.

Examining the list of process variables governing motion in Figure 2 indicates that the closed loop control is imposed on velocity and position using the hardware and software components of the stages. For example, the “dll function” adjusts the “potentiometer

resistance" to command the stages to move into position, constantly polling the encoder to ensure that it knows where it is. Thus, position-related variables such as velocity, hatch spacing, beam offset and hatch shrink may be considered under closed-loop control. These are all variables that inversely affect deposition: increasing velocity, keeping other variables constant, reduces deposition.

Examining the list of process variables governing the material delivery system indicates that there is inherent coupling between the motor rpm and the carrier gas flow rate. The relationship between the two has been experimentally observed to vary from day to day, perhaps because of the powders settling due to vibrations and changes in relative humidity. Though closed-loop control exists over the powder motor rpm and the center purge mass flow rate, the interaction between the two is coupled. Thus, powder motor rpm and center purge mass flow rate are listed as being under closed-loop control, but the mass flow rate of the powders is listed as being under indirect control.

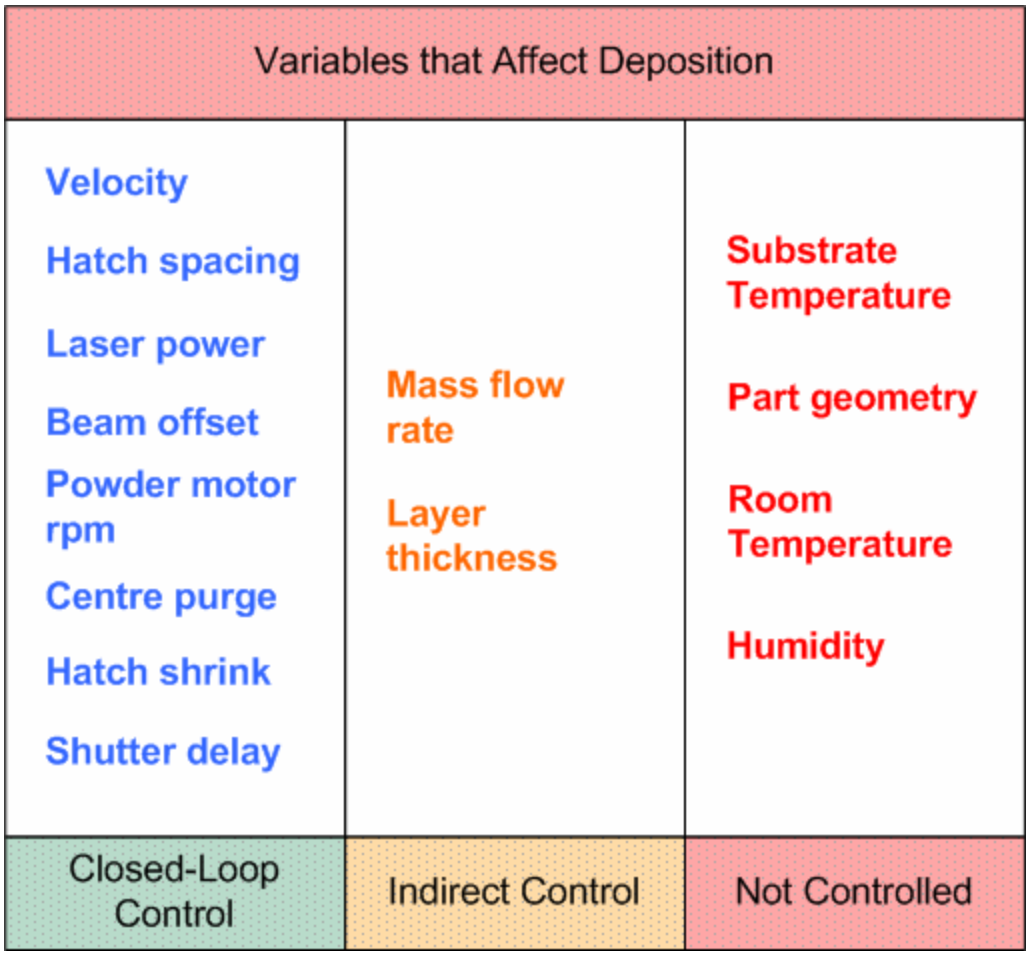

Figure 5: Design inadequacy - no temperature monitoring

Closed loop control is imposed on most variables that affect deposition, but mass flow rate and layer thickness are, at best, under indirect control. Some variables that affect deposition such as the substrate temperature and the part geometry are not controllable in this design.

Examining the list of process variables governing energy delivery indicates that energy delivery is coupled with motion when a standard hatch pattern is drawn, causing an increase in substrate temperature as the build progresses. Since deposition varies with substrate temperature, continual control of the laser power based on substrate temperature is desirable. No provisions have been made to control laser power based on substrate temperature, so it is listed as being not controlled.

2.7 Conclusions

The functional decomposition technique borrowed from axiomatic design indicates that:

- Functional requirements of material and energy delivery are necessarily coupled, and axiomatic design theory is not adequate to deal with such situations.
- Not all variables that affect deposition are under closed-loop control. Some variables are not even measured.
- Substrate temperature is neither measured nor controlled. It is variable because of coupling between the hatch pattern being drawn and the laser power.
- Layer thickness is neither measured nor controlled, though uneven substrate temperature causes uneven layers.
- Mass flow rate is variable due to coupling between the carrier gas and the powder motor rpm. It is under indirect control, though it affects deposition.
- Process models claiming to predict deposition must incorporate the uncertainty due to indirect control over mass flow rates and the effect of substrate heating.

3 Model Development

3.1 Introduction

When building components using LENS™, the laser is always retracted by a user-defined layer thickness between each layer, irrespective of the thickness of the layer actually deposited. If there is a mismatch between the distance retracted and the deposited thickness – as there often is – the laser is no longer focused on the surface in subsequent layers, making it impossible to achieve dimensional accuracy or, in extreme cases, even making it impossible to continue building. Therefore, a key requirement when building components using LENS™ is that the thickness of the deposited layer matches the user-defined layer thickness. Being able to estimate the deposited thickness for a given set of process variables could reduce the difference between the user-specified layer thickness and the actual deposition thickness, potentially resulting in better and more efficient builds.

The LENS™ machine is designed so several process variables can be adjusted, which would make a model incorporating all of them unnecessarily complicated. Therefore, only process variables that are likely to create a significant impact on deposition are considered in the models developed in this chapter. Two models for deposition are developed here; both based purely upon these build parameters, part geometry and material properties. The first model is designed to predict the ***average*** deposition over an entire layer and the second is designed to predict ***spatial*** deposition within a layer. The average deposition model would ignore the tendency of edge-heating to increase deposition at the edges while the spatial deposition model would attempt to incorporate edge-heating effects.

A conclusion of the previous chapter is that substrate temperature rise is not controlled and can affect deposition. This is true for all builds, but the effect may be insignificant for large builds in which the substrate has time to cool down before the laser returns. Therefore, neglecting the edge heating that occurs when the laser reverses direction may be not be a serious omission. In such cases, a simple model that can quickly relate the average deposited thickness to the build parameters chosen can be useful. The average deposition model fits this niche.

For small builds, the rise in substrate temperature can cause increased deposition at the edges that tend to overheat due to the rastering pattern used. This is because the laser retraces its path near a previously heated location before it has time to cool down. A model that incorporates the effect of substrate heating can be useful in such situations. The spatial deposition model fits this niche.

The two models developed in this chapter are therefore intended to handle a variety of build situations, the spatial deposition model being more widely applicable.

The approach followed while developing the models is to study the effect of the four most important process variables controlling deposition in terms of the energy and mass they provide to the melt pool. The variables studied are:

- Laser Power
- Velocity
- Hatch Spacing
- Mass Flow Rate

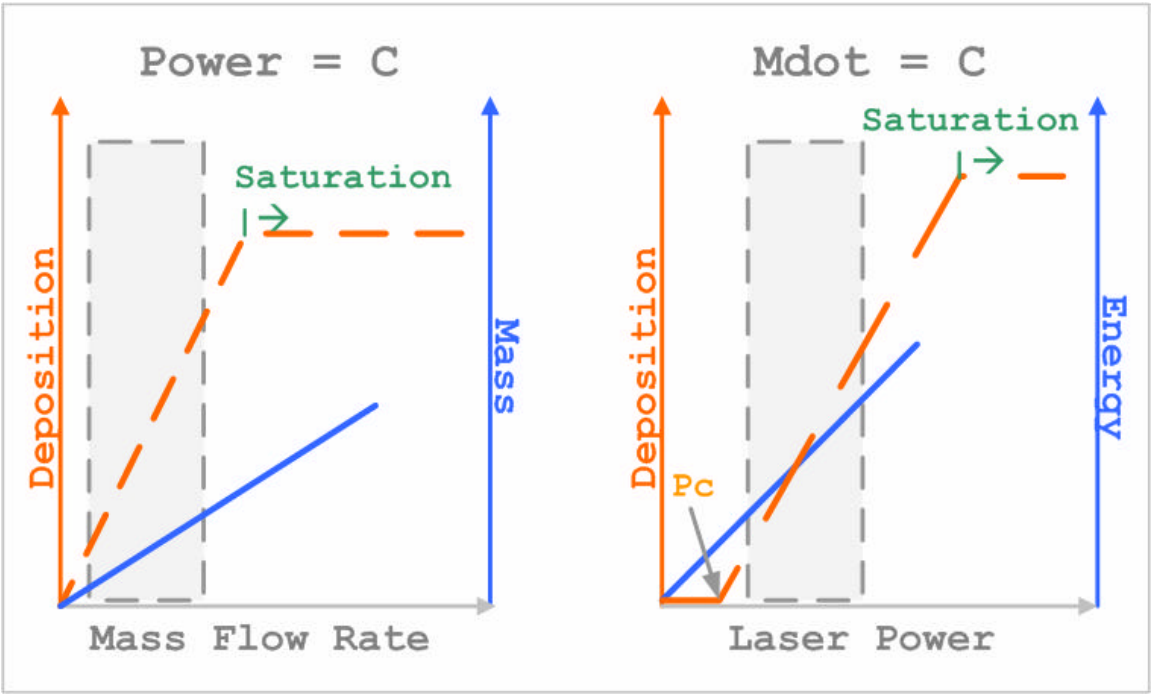

Figure 6: Assumed effect of Mass Flow Rate and Laser Power on Deposition

Left: Mass flow rate is assumed to be linearly related to mass per unit area. Deposition is assumed to vary linearly with mass per unit area until the laser power is exhausted. Right: Laser power is assumed to be linearly related to the energy per unit area. Deposition is assumed to vary linearly with energy per unit area until the mass is exhausted.

All models use simplifying assumptions. The major assumptions used are discussed in the following paragraphs.

Both models assume the existence of a region within which deposition is directly related to the mass flow rate and the laser power, as shown in Figure 6. The experiments conducted were designed to lie in this region.

An implicit assumption made is that the mass can be calculated from the mass flow rate and that the energy available can be calculated from the laser power. Since neither of these variables is directly controllable on the LENS™ machine, the challenge is to calculate them from controllable build parameters.

The energy provided to the melt pool is assumed directly proportional to laser power and inversely proportional to the velocity and the hatch spacing. Increasing laser power increases the energy, but increasing velocity and hatch spacing decreases energy. The mass provided to the melt pool is assumed proportional to the mass flow rate.

It seems logical to assume that increasing mass flow rate at constant laser power would result in increased deposition until the energy absorbed from the laser was completely exhausted. Increasing mass flow rate beyond this point should have no effect on deposition, as there is no energy left to cause melting. Similarly, it seems logical to assume that increasing laser power at a constant mass flow rate would increase deposition until all the available material was deposited. Further increase in laser power would have no effect on deposition as there is no mass left to deposit.

3.2 Sources of Uncertainty

Experimental results are always subject to some level of uncertainty, and must be interpreted against the backdrop of experimental realities. Four major sources of uncertainty that could affect the models are:

- Degree of control that the equipment imposes over process variables.
- Simplifying assumptions.
- Process window chosen for experiments.
- Measurement techniques.

The following sections discuss the major sources of uncertainty for these models in detail.

3.2.1 Mass Input

Mass input is changed indirectly by varying the mass flow rate, $\dot{m}$. The mass input into the build chamber for a build that takes time, t, is

$$m = \int_0^t \dot{m} dt \tag{1}$$

Since the mass enters the chamber as a stream of powders carried by a fast-moving stream of argon, powder spheres inevitably collide with each other and with the substrate. The exact spatial distribution of mass is not known, but a Gaussian distribution centered over the melt pool is expected. Given that deposition can only occur in the vicinity of the melt pool, the distribution of mass may be assumed invariant over the melt pool if its size is small compared to the region in which the powders fall. Figure 2 illustrates the assumption of an invariant distribution of mass and energy.

There is some uncertainty in the mass flow rate, inherent in the powder delivery method. Since fluctuations in the mass flow rate during a build affect the deposition thickness, some understanding of this uncertainty is required when evaluating the models. Both models use the same material delivery model, which assumes that the mass available is linearly related to the mass flow rate raised to some power through a constant of proportionality that is assumed to be some function of build parameters.

3.2.2 Energy Input

Energy input is controlled by changing the laser power, P. The energy input into the build chamber for a build that takes time, t, is

$$Q = e\int_0^t \left(P - P_c\right) dt \qquad (2)$$

In this equation, P_c is the critical power required to initiate melting under the experimental conditions and $0 \le e \le 1$ is the absorptivity of the substrate material at the laser wavelength.

The radial power distribution of a laser source is probably Gaussian, but we assume that it is constant to simplify calculations. Figure 2 shows the assumptions made in the development of these models regarding the distribution of mass and energy.

The path of the laser to the substrate is partially obscured by fast moving powder particles, which attenuate its power. Both models neglect this attenuation, based on experiments performed by other researchers (Schneider, 1998) studying laser cladding, a conceptually similar process, that suggest that attenuation of power is negligible.

Only a fraction, e of the laser power is absorbed by the surface and increases the energy at that point. This fraction is reported by other researchers as 0.37 for Ti-6Al-4V (Xie and Kar, 1999). Both models use this scaling factor in their estimation of available energy. Radiation reflected off other metal objects can contribute to substrate heating, but this is assumed negligible.

The average deposition model assumes that deposition is linearly related to the absorbed energy raised to some power. It ignores the effect of substrate heating as the build progresses, and is therefore unable to predict spatial changes in deposition due to the raster pattern used. Consequently, the model performance is weakest at the edges of a build, which are known to overheat. On the other hand, the edge regions of a large build form a small fraction of the deposited volume, and the errors may be insignificant. Therefore, this simple model is best used for large builds on a relatively massive substrate, where the substrate has plenty of time to cool before the laser returns.

The spatial deposition model also assumes that the deposition is directly proportional to the absorbed energy, but attempts to account for the effect of substrate heating. To that extent, this model should be more applicable to smaller builds, in which substrate temperature changes significantly.

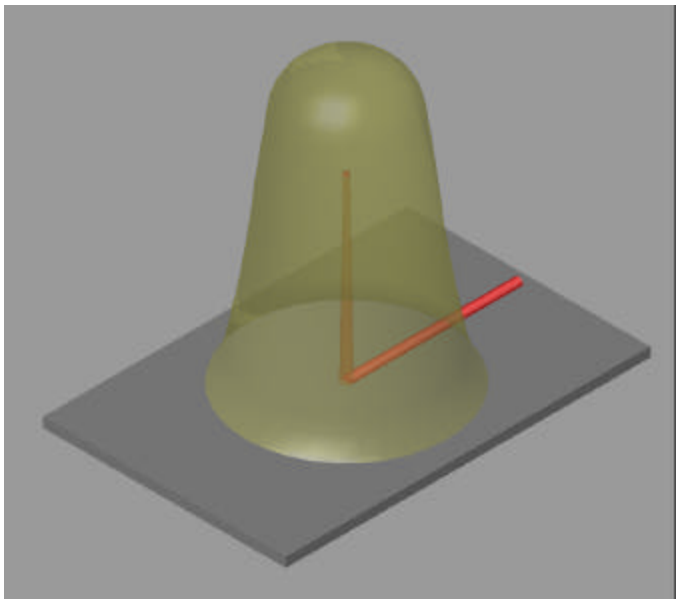

Figure 7: Assumed distribution of mass and energy

It is assumed that the probable distribution of mass and energy in the vicinity of the melt pool is Gaussian. The melt pool region is much smaller than the region into which the powders fall. Over this small region, laser power and mass may validly be assumed invariant.

3.2.3 Parameter Window

Having decided to model the system based on the laser power and the mass flow rate, a decision on the range of values to test the models must be taken. This window must be appropriate for the material being used in the tests and must lie well within the capabilities of the machine.

The laser delivers enough power to melt the substrate at about 100 W. Though power can be increased to about 900 W (see Figure 3), increasing it much beyond 500 W tends to overheat the material, allowing the carrier gas to blow molten material out of the melt pool and deposit it on the nozzles. The material stuck to the nozzles absorbs the reflected radiation and stays molten and powders that would otherwise have bounced off the nozzles stick to it. This could effectively lower the mass available to the melt pool, forcing an upper bound on laser power for layer builds.

A lower limit of about 250 W and an upper limit of 350 W, a predictable region in which the power is high enough to deposit Ti-6Al4-V, was chosen for the layer tests. Since single line tests take far less time than 1 and 2-layer builds, the probability of material

sticking to the nozzles is smaller. This allowed single line tests to be run using a wider range of parameters. The maximum power used in the single line tests was 558 W.

Controlling the mass flow rate is notoriously difficult, as the correlation between the powder motor rpm and the amount delivered to the build chamber appears dependent on relative humidity, temperature, powder size distribution and, potentially, upon a host of other factors. A window within which the powder was known to be stable was chosen (see Figure 3). The mass flow rate for layer tests was varied between 0.0310 gs^{-1} and 0.0855 gs^{-1}. Single line tests allowed higher mass flow rates to be used as they finished quicker, reducing the chance of powders sticking to the nozzles. The mass flow rates were changed from 0.1749 gs^{-1} to 0.2288 gs^{-1} in these tests.

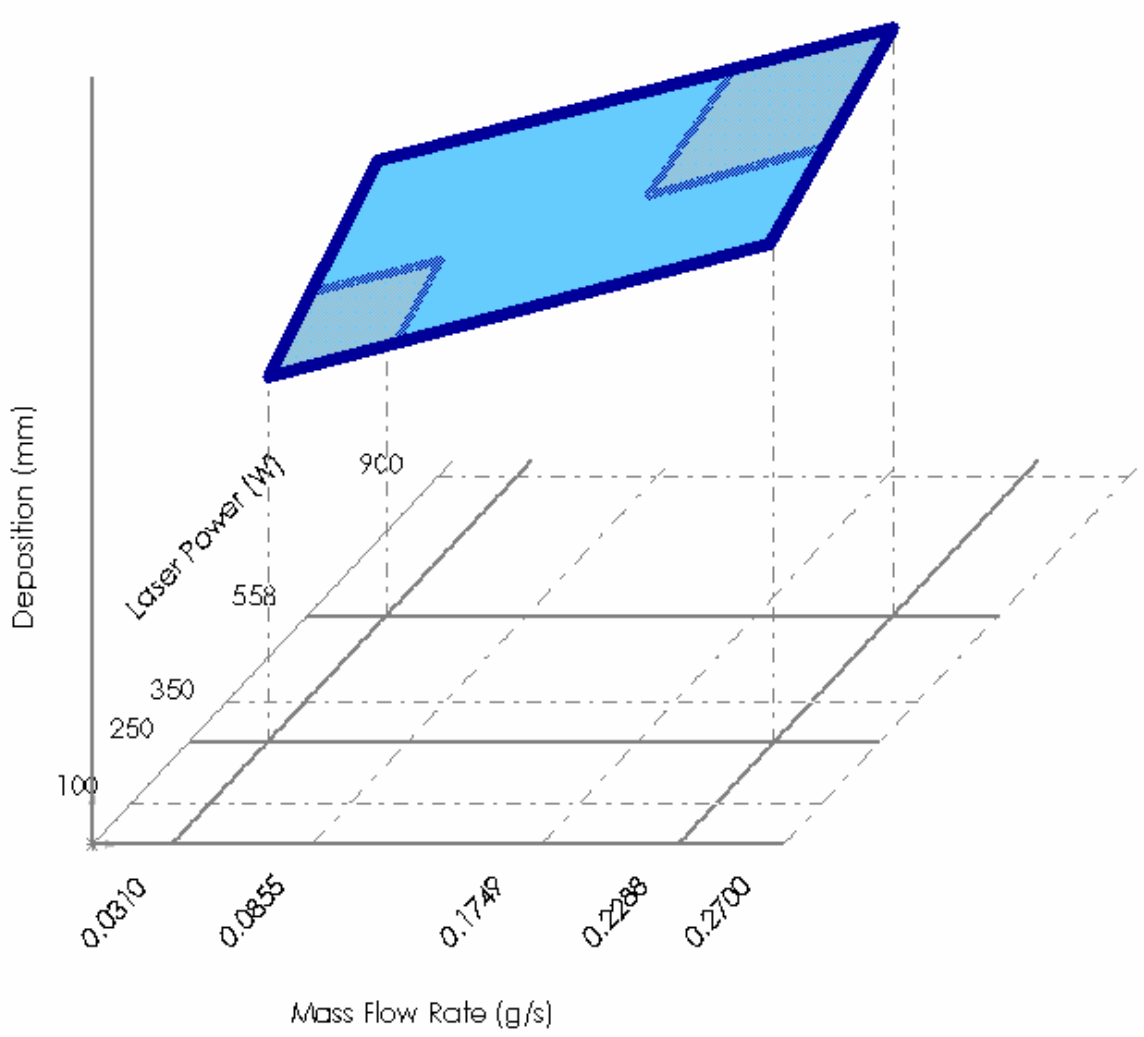

Figure 8: Process Limits of the LENS™ 850

The parameter range was restricted in the layer tests to prevent particles from sticking to the nozzles. Single line tests could be run using a wider parameter window as they took less time.

3.2.4 Measurement Technique

The deposition thicknesses measured for all experiments lie below 300 µm. The measurement instruments used must necessarily span this range. Three types of measuring instruments were used for thickness measurements. The UBM and the SLM, non-contact profilometers, were used for the layer builds and an optical microscope was used for the line builds.

The range of the UBM sensor was 1000 µm, over three times the range of values being measured. The average difference between predictions for single line builds was 2.22 µm requiring the use of an optical microscope with a resolution of 2.9 µm/pixel. The average difference between predictions for 1-layer and 2-layer builds was 13.8 µm and 20.22 µm, respectively. The UBM, with a resolution of 1.0 µm was used to make these measurements.

The following sections develop models for material delivery and average and spatial deposition. The models are tested experimentally, using values for parameters that span most of the usable range of the machine.

3.3 Material Delivery Model

The objective of this section is to develop a model to predict the mass of material available for deposition based upon build parameters and material properties. The assumption is that the mass deposited can be related to the build parameters via a constant of proportionality which is some function of material properties and geometry.

$$z = K_M \left(\text{Build Parameters}\right)^a$$
$$K_M = f\left(\text{Material Properties}\right) \tag{3}$$

In this equation, z is the deposited thickness and K_M is a function of material properties.

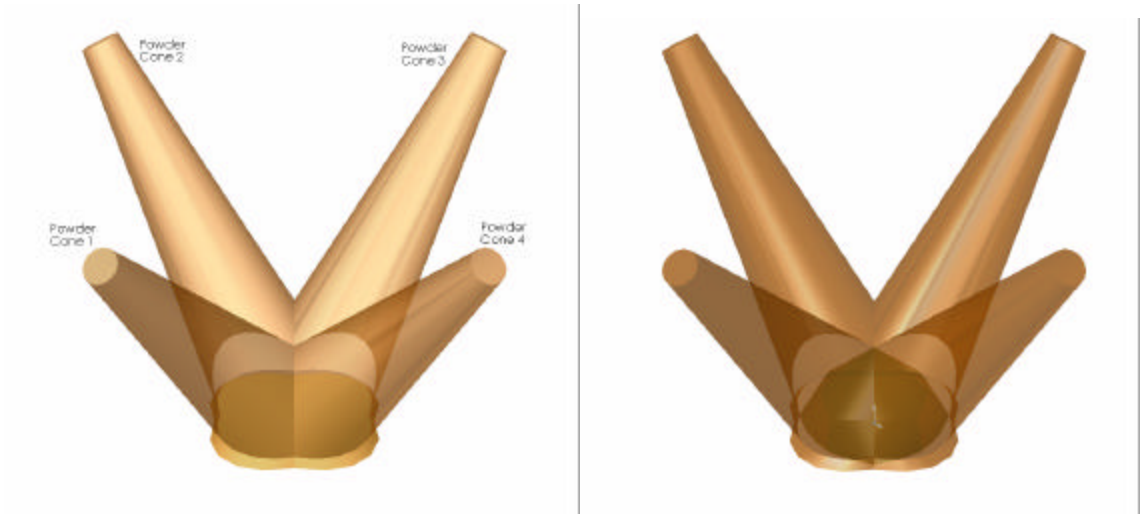

Figure 9: Powder stream cones from the nozzle

Left: Four powder cones intersecting over the melt pool. Right: Intersection region of the cones, highlighting the region in which random particle velocity and density is assumed.

Powder is conveyed from the container, carried by a stream of inert gas, and passes through four nozzles focused on the melt pool as shown in Figure 9. The powder streams diverge somewhat when they leave the nozzles, forming conical streams of powder. These powder cones intersect in the vicinity of the melt pool – the highlighted region in the figure on the right – making inter-particle collisions inevitable. Since the dominant velocity component of the powders and gravity both act in the $-z$ direction, there is a net downward component to particle velocity. Velocity components in the other coordinate directions may validly be assumed random, since particles should be equally likely to travel in these directions after collision. Therefore, inter-particle and particle-substrate collisions effectively reduce the amount of material available for deposition by some unknown, but constant factor, $0 \le f_1 \le 1$. If $\dot{m}$ is the mass flow rate of material crossing a horizontal plane at the substrate surface, $z = 0$, the reduced mass flow rate would be

$f_1\dot{m}$. If the mass crosses the plane $z = 0$ in a region of unknown geometry characterized by a length d_{pwdr}, the area of the region would be:

$$A_M = C_{AM}\left(d_{pwdr}\right)^2 \tag{4}$$

C_{AM} is a constant relating the area to the characteristic length. If the melt pool is enclosed within A_M and characterized by a length d_{melt}:

$$A_L = C_{AL}\left(d_{melt}\right)^2 \tag{5}$$

C_{AL} is a constant relating the area to the characteristic length. Therefore, the mass flow rate available to the molten region would be:

$$\dot{m}_{\text{Melt Pool}} = \left(\frac{A_L}{A_M}\right) f_1\dot{m} = \frac{C_{AL}d_{melt}^2}{C_{AM}d_{pwdr}^2} \times f_1\dot{m} \tag{6}$$

Since the nozzles travel over the substrate with a velocity u, the mass per unit length is:

$$m_y = \frac{dm}{dt}\frac{dt}{dy} = \frac{C_{AL}d_{melt}^2}{C_{AM}d_{pwdr}^2} \times \frac{f_1\dot{m}}{u} \tag{7}$$

As $m_y = \frac{Vr}{dy} = A_{CS}\,r$ where the cross sectional area of the bead, $A_{CS} = C_{CS}z^2$, $m_y = C_{CS}\,r\,z^2$.

$$z = \sqrt{\frac{m_y}{C_{CS}\,r}} \tag{8}$$

Substituting for m_y,

$$z = \sqrt{\frac{C_{AL}d_{melt}^2}{C_{CS}C_{AM}d_{pwdr}^2} \times \frac{f_1}{r}} \times \sqrt{\frac{\dot{m}}{u}} \tag{9}$$

Equation (9) can be used to calculate the upper limit on material available to a volume element on the surface of the substrate and has been arranged in the format suggested by Equation (3). The first term on the right hand side is expressed as a function of build parameters and material constants, and is equivalent to K_M and has units $\sqrt{L^3.M^{-1}}$. The power a to which the build parameters have been raised is 0.5.

3.4 Average Deposition Model

3.4.1 Introduction

The objective of this section is to develop a model to predict the mass of material available for deposition based upon build parameters and material properties.

The average deposition model (ADM) assumes that build parameters ultimately affect the values of two variables at the substrate surface:

1. Energy absorbed and
2. Mass of material available.

Therefore, these two variables must ultimately control deposition. Unfortunately, neither the energy nor the mass available can be altered directly – they must be altered indirectly through some combination of build parameters. Therefore, the model must individually relate deposition to energy and mass through process parameters.

Experimental observations indicate that increasing laser power increases deposition. They also indicate that increasing mass flow rate increases deposition. As boundary conditions, if no energy is supplied or if no mass is supplied, deposition becomes zero. A model for deposition must incorporate these observations.

3.4.2 Modeling Energy Delivery

The assumption made in modeling energy delivery is that the energy available for deposition can be related to the build parameters via a constant of proportionality which is some function of material properties and geometry.

$$\begin{aligned} z &= K_{EA}\left(\text{Build Parameters}\right)^{a} \\ K_{EA} &= f\left(\text{Mateial Properties}\right) \end{aligned} \tag{10}$$

If ΔT_m is the difference between the melting temperature and room temperature, the energy required to melt a mass m is (Halliday and Resnick, 1966):

$$Q = m\left(c_p \Delta T_m + h_f\right) \tag{11}$$

If P is the power of the laser, P_c is the critical power that must be supplied to initiate melting and $e = 0.37$ is the absorptivity of the Ti-6Al-4V substrate at a laser wavelength of 1.06 μm (Xie and Kar, 1999), the energy provided by the laser is:

$$Q = e\int_0^t (P - P_c).dt = e\,(P - P_c)t \tag{12}$$

Equating Equations (11) and (12), using $m = V\,r$ and dividing both sides by t:

$$\frac{V\,r\left(c_p \Delta T_m + h_f\right)}{t} \le e\,(P - P_c) \tag{13}$$

Since $V = A_{CS}\,y$, where A_{CS} is the cross-sectional area of the bead, and since $A_{CS} = C_{CS}\,z^2$, where C_{CS} is a shape factor for the cross-sectional area of the bead, $V = C_{CS}\,yz^2$. Substituting and solving for z:

$$z = \sqrt{\frac{e}{C_{CS}\,r\left(c_p \Delta T_m + h_f\right)}}\sqrt{\frac{(P - P_c)}{u}} \tag{14}$$

Equation (14) is applicable for $u > 0, P \ge P_c$ and ΔT_m greater than the melting point. The term within the curly braces is equivalent to K_{EA} and has units $\sqrt{L^3.J^{-1}}$.

3.4.3 Combining Energy and Material Delivery

Equations (14) and (9) provide relationships between deposition and the major parameters that are thought to govern it. Any model for deposition must reconcile both equations and incorporate the experimental and intuitive observation that deposition becomes 0 if either mass or power is 0.

One possible mathematical relationship between the equations is multiplicative. In such a relationship, deposition will become 0 if either parameter is 0 and will increase if either parameter increases, matching experimental observations.

Since both these equations have units of length, their product would have units of area. Taking the square root of the product would restore the relationship to length. Therefore, we hypothesize that a relationship between build parameters and deposited thickness for N layers could be described by:

$$z = N \times K_A \sqrt[4]{(\text{Build Parameters})} \tag{15}$$

Substituting Equations (14) and (9) in Equation (15) and segregating build parameters gives the average deposition model.

$$z = N\sqrt[4]{\frac{C_{AL}d_{melt}^2}{C_{CS}^2 C_{AM} d_{pwdr}^2} \times \frac{f_1 e}{r^2\left(c_p \Delta T_m + h_f\right)}} \times \sqrt{\frac{\left(P - P_c\right)\dot{m}}{u^2}} \tag{16}$$

Equation (16) expresses the deposited thickness as a function of build parameters, part geometry and material properties, fulfilling the stated objective of this section and is valid when $u > 0$ and $P \geq P_c$. The term within the curly braces is K_A and has dimensions of $\sqrt[4]{L^6.M^{-1}.J^{-1}}$, which, when multiplied by the term outside, having units of $\sqrt[4]{L^{-2}.M^1.J^1}$, results in a length dimension. For Ti-6Al-4V, the value of this constant term is $1.9436\ \sqrt[4]{mm^6.g^{-1}.J^{-1}}$. Table 1 explains the constant terms in the equation, listing values used in the simulation.

3.4.4 Effect of Temperature

The LENS™ process is not 100% efficient, so only a fraction of the absorbed energy is used for melting. The remainder of the absorbed energy is dissipated by various mechanisms such as substrate heating, radiative and convective cooling. Since the effect of temperature on deposition is not considered in the above treatment, any test should keep the sample dimensions small with respect to that of the substrate to minimize its effect.

An upper bound for substrate temperature may be obtained by assuming all absorbed energy is used to heat the substrate and neglecting all heat losses including the heat of fusion. This can be justified because the material deposited is in intimate contact with the substrate material (it is fused to it) and is likely to lose a large part of its heat by conduction through the substrate.

The time taken for the laser to build a layer at a velocity u is:

$$t = \frac{XY}{(\Delta x)u} \tag{17}$$

The total energy absorbed from the energy supplied by the laser during that time is:

$$Q = e\int_0^t \left(P - P_c\right).dt = e\left(P - P_c\right)t = \frac{e\left(P - P_c\right)XY}{(\Delta x)u} \tag{18}$$

The temperature rise in the substrate caused by building a layer may be calculated from:

$$\Delta T_s = \frac{Q}{m_s c_p} = \frac{e\left(P - P_c\right)XY}{(\Delta x)u m_s c_p} \tag{19}$$

In this equation, m_s is the mass of the substrate, neglecting the incremental mass of the deposit and c_p is the specific heat capacity of the substrate material. Equation (19) provides the average substrate temperature at the end of the build and is not indicative of the substrate temperature just below the laser, which may be higher. The temperatures calculated using this approach should be lower than, but consistent with temperatures measured using embedded thermocouples. For this model to be valid, deposition should be linear with all combinations of build parameters used in Equation (16), provided the substrate temperature does not change appreciably. Therefore, the 1-layer builds should be differentiable from the 2-layer builds. Since this model ignores temperature rise in the substrate, it is applicable only to large builds in which the substrate has had time to cool down as the laser rasters across the part. Since the effect of temperature is not incorporated into the model, building multiple layers should reveal its sensitivity to changes in substrate temperature.

Table 5: Explanation of Constant Terms in ADM

Term	Explanation
$C_{AL} = 1.0$	Dimensionless constant relating the area of the melt pool to the square of the diameter. **Value unknown**.
$C_{AM} = 1.0$	Dimensionless constant relating the area of the region on the substrate within which the material falls to the square of the diameter. **Value unknown**.
$C_{CS} = 1.0$	Dimensionless constant relating the cross-sectional area of the melt bead to the thickness. **Value unknown**.
$c_p = 0.546 \ \left(J.g^{-1}.K^{-1}\right)$	Specific heat capacity of Ti-6Al-4V at 25 $^{\circ}C$, (Mills, 2002).
$\left(\frac{d_{melt}}{d_{pwdr}}\right)^2 = 1.0$	Dimensionless ratio of areas. Numerator is related to the area of the molten region and denominator is related to the area of the region on the substrate into which material falls. **Value unknown**.
$e = 0.37$	Dimensionless absorptivity of Ti-6Al-4V at a laser wavelength of 1.06 µm. (Xie and Kar, 1999).
$f_1 = 1.0$	Dimensionless fraction of mass available to the melt pool, the remainder being lost by scattering. **Value unknown**.
$h_f = 440 \ \left(J.g^{-1}\right)$	Value for Titanium, obtained from Metals Handbook, IX Ed., Vol 3, page 816. Source lists value as "estimated".
$P_c = 65\left(J.s^{-1}\right)$	Critical power required to initiate melting. Dependent on mass of substrate, ambient conditions. Value estimated from Material Delivery Model.
$r = 0.00442 \ \left(g m m^{-3}\right)$	Density of Ti-6Al-4V at 25 $^{\circ}C$, (Mills, 2002).
$\Delta T_m = 1625 \ \left(^{\circ}C\right)$	Difference between melting temperature and room temperature. Melt temperature taken as 1650 $^{\circ}C$ (Mills, 2002), room temperature assumed to be 25 $^{\circ}C$.

3.5 Spatial Deposition Model

3.5.1 Introduction

The objective of this section is to develop a model that can predict the deposition thickness at any location during the build based on build parameters, part geometry and material properties. Since deposition is a function of temperature, the model takes into account the temperature rise in the substrate due to the rastering pattern as the build progresses.

3.5.2 Modeling Energy Delivery

The only source of energy is the laser, which supplies energy into the system at a constant rate throughout the build. In this model, energy input is modeled as a series of equally spaced heating events that occur along the path of the laser as the build progresses. The path of the laser can be discretized into intervals of length d, a heating event occurring at each of these intervals.

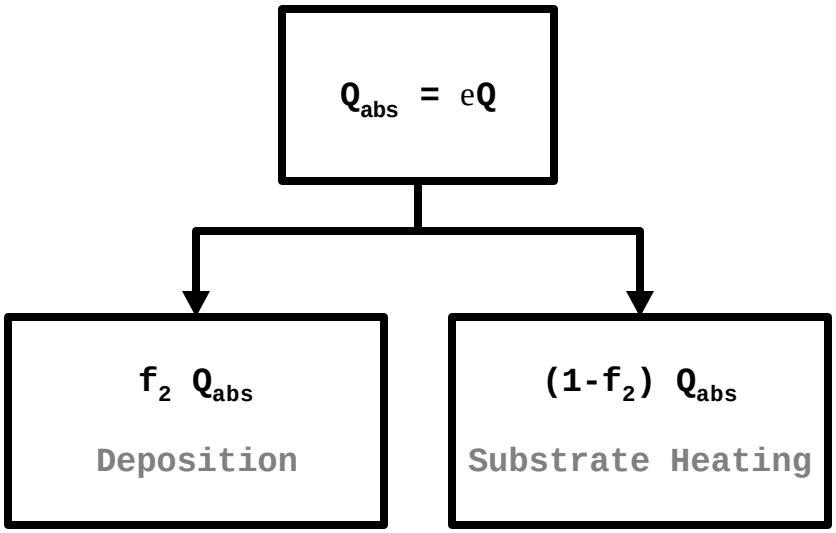

Figure 10: Partition of Absorbed Energy

Only a fraction of the absorbed energy is used for deposition – the balance is used to heat the substrate.

Only a fraction of the supplied energy is absorbed, depending on the absorptivity of the material. Some of the absorbed energy is expended by depositing material, while the rest raises the temperature of the substrate by some temperature differential, ΔT. Consequently, substrate temperature is higher than the initial temperature for all but the

first heating event. If $0 \leq f_2 \leq 1$ is the unknown fraction of energy used for deposition, $(1-f_2)$ must be the fraction that causes substrate heating, as shown in Figure 10.

Since raising temperature is analogous to raising energy, there are effectively two energy sources at every location the laser passes over. The energy available at any location, $Q(x,y,z,t)$, is a combination of the time-independent energy delivered by the laser to that location, Q_L, and the cumulative energy available at that location due to substrate heating from previous heating events, $Q_T(x,y,z,t)$. Figure 6 illustrates this concept.

$$Q(x,y,z,t) = Q_L + Q_T(x,y,z,t) \tag{20}$$

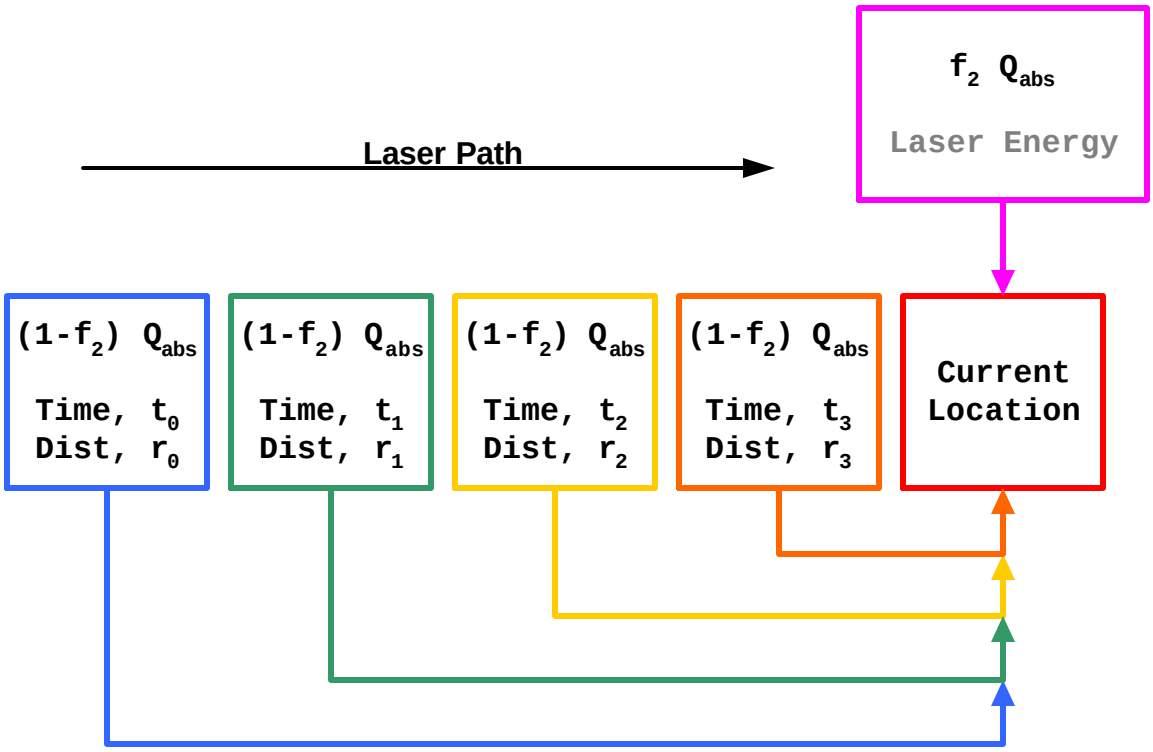

Figure 11: Energy Available at a Location

The energy available at a location is the fraction of energy directly provided by the laser, used for deposition plus the cumulative energy available from previous substrate-heating events.

The laser covers an area XY in $\frac{XY}{(\Delta x)u}$ units of time, as it builds a layer, so it can cover and area of d^2 in $\frac{d^2}{(\Delta x)u}$ units of time. Since $Q = e(P - P_c)t$, the fraction of energy available from the laser at each heating event is:

$$Q_L = \frac{f_2 e (P - P_c) d^2}{(\Delta x) u} \tag{21}$$

And the fraction, $Q_h(x, y)$, used to heat the substrate at each heating event is:

$$Q_h(x, y, z, t) = \frac{(1 - f_2) e (P - P_c) d^2}{(\Delta x) u} \tag{22}$$

The cumulative contributions of each individual, timed heating event $Q_h(x, y, z, t)$ along the laser path can be converted to an equivalent energy. This energy is the excess energy, $Q_T(x, y, z, t)$, available due to substrate heating at that point. For the i^{th} heating event,

$$\begin{aligned} Q(x_i, y_i, z_i, t_i) &= Q_L + Q_h(x_0, y_0, z_0, t_0) + Q_h(x_1, y_1, z_1, t_1) + \ldots \\ &\quad \ldots + Q_h(x_{i-1}, y_{i-1}, z_{i-1}, t_{i-1}) \\ &= Q_L + \sum_{n=0}^{i-1} Q_h(x_n, y_n, z_n, t_n) \end{aligned} \tag{23}$$

Substituting $Q_h(x_n, y_n, z_n, t_n) = d^3 \rho c_p \Delta T(x_n, y_n, z_n, t_n)$, gives

$$Q(x_i, y_i, z_i, t_i) = Q_L + \sum_{n=1}^{i-1} d^3 \rho c_p \Delta T(x_n, y_n, z_n, t_n) \tag{24}$$

$\Delta T(x_n, y_n, z_n, t_n)$ is the only unknown in the equation, and is dependent on where the location i lies on the path of the laser.

The temperature at any point at any time due to a single, instantaneous input of Q_h units of heat from a point source can be calculated using Equation **(25)**, the Carslaw Equation for an instantaneous point source of heat of strength $Q_h / \rho c_p$.

$$\Delta T(x,y,z,t) = \frac{Q_h}{8\pi c_p (\pi k t)^{\frac{3}{2}}} e^{-\left\{\frac{(x-x_0)^2+(y-y_0)^2+(z-z_0)^2}{4kt}\right\}} \tag{25}$$

The term $(x-x_0)^2+(y-y_0)^2+(z-z_0)^2$ is the square of the radial distance of the point from the heat source, and is abbreviated as $r(t)^2$. Since temperature is the cumulative contribution of every previous heating event, and since heating events take place at intervals of $t_d = d/u$,

$$\sum_{t=t_0}^{t-t_d} \Delta T(x_n, y_n, z_n, t_n) = \frac{(1-f_2)e(P-P_c)d^2}{8\pi c_p u(\Delta x)(\pi k)^{\frac{3}{2}}} \sum_{t=t_0}^{t-t_d} \left[\frac{e^{-\left\{\frac{r(t)^2}{4kt}\right\}}}{t^{\frac{3}{2}}} \right] \tag{26}$$

All constant factors can and have been removed from the summation (Piskunov, 1981). The term $r(t)^2$ must be calculated for every heating event that occurs during the build. After some algebra, the total energy available at the volume element is obtained by substituting Equation (26) in Equation (20):

$$Q(x,y,z,t) = \frac{e(P-P_c)d^2}{(\Delta x)u} \left\{ f_2 + \frac{d^3(1-f_2)}{8(\pi k)^{\frac{3}{2}}} \sum_{t=t_0}^{t-t_d} \left[\frac{e^{-\left\{\frac{r(t)^2}{4kt}\right\}}}{t^{\frac{3}{2}}} \right] \right\} \tag{27}$$

Equation (27) provides a means to calculate $Q(x,y,z,t)$, the effective energy available at the volume element. Since the effect of substrate heating has already been incorporated into this term, it is analogous to each volume element receiving different amounts of energy, all of which is used to create the melt bead. If the energy calculated from Equation (27) is entirely used to melt a bead of volume $V = d^2 z$, raising it through $\Delta T_m = (T_m - T_0)$ and fusing it:

$$Q(x,y,z,t) = z d^2 \rho \left(c_p \Delta T_m + h_f \right) \tag{28}$$

Solving for z and grouping build parameters:

$$z = \frac{e}{\rho \left(c_p \Delta T_m + h_f \right)} \left\{ f_2 + \frac{d^3(1-f_2)}{8(\pi k)^{\frac{3}{2}}} \sum_{t=t_0}^{t-t_d} \left[\frac{e^{-\left\{\frac{r(t)^2}{4kt}\right\}}}{t^{\frac{3}{2}}} \right] \right\} \frac{(P-P_c)}{(\Delta x)u} \tag{29}$$

Equation (29), valid for $d > 0$; $u > 0$ and $\Delta x > 0$, predicts the deposition thickness as a function of build parameters, part geometry and material properties and attempts to account for the heating of the substrate due to the rastering pattern used.

3.5.3 Combining Energy and Material Delivery

The same reasoning used in developing the average deposition model applies to the spatial deposition model, and the energy and material delivery models are combined as before. Consequently, the spatial deposition model for N layers is:

$$z(x,y,t) = N \times K_S \sqrt{\frac{(P - P_c)}{(\Delta x)u}} \sqrt[4]{\frac{\dot{m}}{u}} \tag{30}$$

$K_S = \sqrt[4]{\left(\frac{C_{AL}}{C_{CS}C_{AM}}\right)\left(\frac{d_{melt}}{d_{pwdr}}\right)^2 \frac{f_1}{r}} \sqrt{\frac{e}{r\left(c_p \Delta T_m + h_f\right)}\left\{f_2 + \frac{d^3(1-f_2)}{8(pk)^{\frac{3}{2}}} \sum_{t=t_0}^{t-t_d}\left[\frac{e^{-\left\{\frac{r(t)^2}{4kt}\right\}}}{t^{\frac{3}{2}}}\right]\right\}}$, has dimensions, $L^{2.25}.M^{-0.25}.J^{-0.25}$, and must be calculated recursively along the path of the laser. The combination of build parameters at the right extreme of the equation has units $L^{-1.25}.M^{0.25}.J^{0.25}$, resulting in dimensions of length, when multiplied by K_S. Equation (30) is valid for $P \geq P_c$; $\Delta x > 0$ and $u > 0$. The table below lists terms in the SDM that are not in the ADM.

Table 6: Explanation of Constant Terms in SDM

Term[1]	Explanation
d	The incremental length between heating events. Used $d = \Delta x$ in the calculations.
Δx	The hatch spacing, or the distance between consecutive, parallel lines.
$f_2 = \frac{A_{Bead}}{A_{HAZ}} = 0.0851$	Energy partition term. The fraction of absorbed laser energy used for deposition, the balance being used for substrate heating. Obtained from the cross-sectional areas of the melt bead and the heat affected zone for the 64 single line tests.
$k = \frac{K}{r\,c_p} = 2.9006 \frac{mm^2}{s}$	The thermal diffusivity of Ti-6Al-4V calculated using the formula shown. Values from (Mills, 2002)
t_d	Time required to travel the distance d.
$t - t_d$	Current time minus time since the last heating event.

[1] The reader is referred to Table 1, where terms common to the ADM and SDM are described.

The only unknown in Equation (30) is $r(t)$. The location of the laser at any time during the build (the laser path) must be known to calculate $r(t)$. Since the laser is turned off during indexing operations, the periods during which the laser is on (the laser status) must also be known. The following sections derive equations for the laser location as it follows a serpentine path, based on build parameters.

3.5.4 Generating the Laser Path

3.5.4.1 Defining Laser Status

Consider a rectangular area being built using the LENS™ process using the standard hatch pattern. Let us define a line to consist of one drawing action followed by an indexing action. Thus:

$$1\ Line = 1\ Draw\ Operation + 1\ Index\ Operation \tag{31}$$

In Figure 7, the laser starts moving at (x_0, y_0). It travels a distance, Y, the y-coordinate of the rectangle being drawn, before shutting off and indexing over by the hatch spacing, h, to the start of the next line. The N_i's mark the end positions of the i^{th} line and the laser is at $P(t)$ at any time, t. Let the line contain n intervals of size d per draw operation and 1 interval of size Δx for the indexing operation. The time taken to complete each of these operations can be calculated from the velocity of the laser relative to the substrate, neglecting acceleration and deceleration effects and assuming that it is equal for drawing and indexing operations. Thus, if the time per element is $t_d = d/u$,

$$\begin{aligned} &\frac{\text{Time}}{\text{Draw Operation}}, t_d = nd/u = nt_d \\ &\frac{\text{Time}}{\text{Index Operation}}, t_{ndx} = \Delta x/u \\ &\frac{\text{Time}}{\text{Line}}, t_L = \frac{(nd + \Delta x)}{u} \end{aligned} \tag{32}$$

The line number may be calculated as shown below, where the operator, (int) returns the mantissa of the division and where 1 is added to convert it to a 1-based number.

$$N = (\text{int})\left[\frac{ut}{(nd + \Delta x)}\right] + 1 \tag{33}$$

Table 3 lists the intervals during which the laser is drawing and indexing.

Table 7: Drawing and Indexing Times

Line #	Draw Operation		Index Operation	
	t_{start}	t_{end}	t_{start}	t_{end}
1	0	$\left(1nt_d + 0t_{ndx}\right)$	$\left(1nt_d + 0t_{ndx}\right)$	$1nt_d + 1t_{ndx}$
2	$1nt_d + 1t_{ndx}$	$\left(2nt_d + 1t_{ndx}\right)$	$\left(2nt_d + 1t_{ndx}\right)$	$2nt_d + 2t_{ndx}$
3	$2nt_d + 2t_{ndx}$	$\left(3nt_d + 2t_{ndx}\right)$	$\left(3nt_d + 2t_{ndx}\right)$	$3nt_d + 3t_{ndx}$
⋮	⋮	⋮	⋮	⋮
⋮	⋮	⋮	⋮	⋮
N	$\left(N-1\right)\left[nt_d + t_{ndx}\right]$	$\left[Nnt_d + \left(N-1\right)t_{ndx}\right]$	$\left[Nnt_d + \left(N-1\right)t_{ndx}\right]$	$N\left[nt_d + t_{ndx}\right]$

If we adopt the convention of using inequalities for drawing but not in indexing,

$$Operation\begin{cases} Drawing; \forall \left(N-1\right)\left[nt_d + t_{ndx}\right] \le t \le \left[Nnt_d + \left(N-1\right)t_{ndx}\right] \\ Indexing; \forall \left[Nnt_d + \left(N-1\right)t_{ndx}\right] < t < N\left[nt_d + t_{ndx}\right] \end{cases} \tag{34}$$

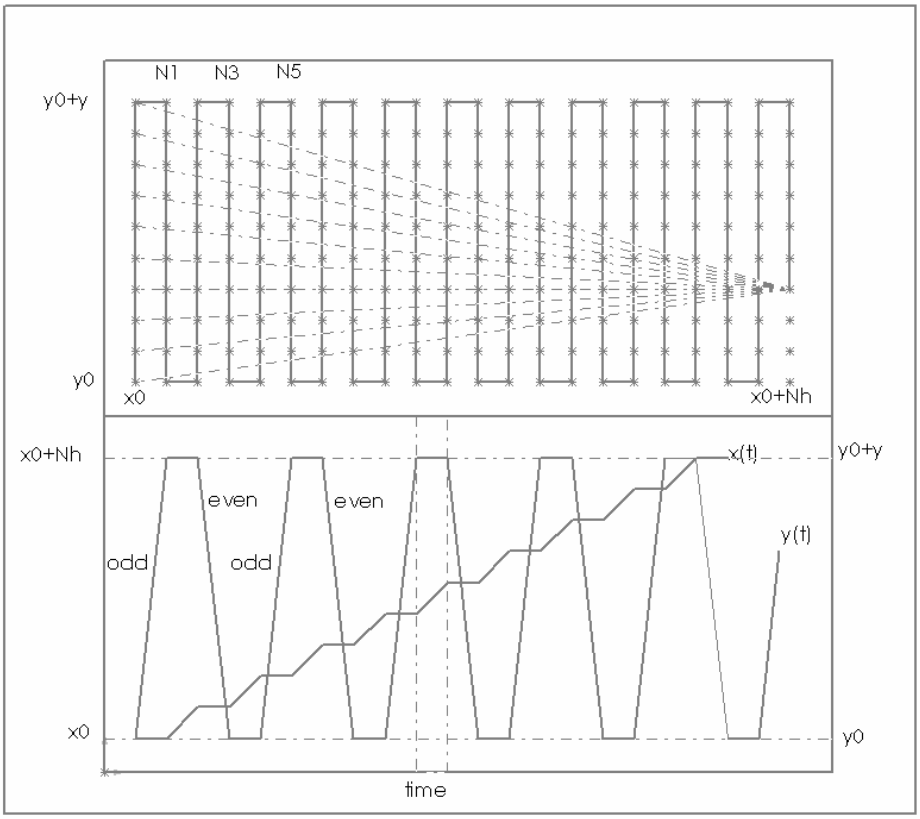

Figure 12: Laser Path during a rastering operation

Top: The path of the laser, showing the location of heating events. Dotted lines denote $r\left(t\right)$*, the distance of previous heating events from the point under the laser. Bottom: The graph of* $x\left(t\right)$ *and* $y\left(t\right)$.

3.5.4.2 Defining Laser Path

The individual components of the laser path are shown in Figure 12. The figure is intentionally not drawn to scale: the hatch operation has been highly magnified to show the laser movement that would otherwise have been masked. In both cases, the horizontal axis represents time and the vertical axis shows the x-position and the y-position of the laser. The ends of the first and second lines are marked on the graph.

The x-position of the laser during drawing is easily obtained, knowing the line number.

$$\overbrace{x(t)}^{Drawing} = x_0 + (N-1)(\Delta x) \tag{35}$$

During the hatch operation, the laser position must be determined from the time since the end of the last draw operation.

$$\overbrace{x(t)}^{Indexing} = x_0 + (N-1)(\Delta x) + \overbrace{\left\{t - \left[Nnt_d + (N-1)t_{ndx}\right]\right\}}^{\text{Time since the end of last Draw Operation}} u \tag{36}$$

The y-position of the laser during the drawing operation is more difficult to determine, as it is based on a reference y-coordinate that is dependent on whether the line number is even or odd, a $\pm$ term also dependent on whether the line number is even or odd and the time since the start of the current draw operation.

$$\overbrace{y(t)}^{Drawing} = \overbrace{\left\{y_0 + \left[(N-1)\%2\right]y\right\}}^{\substack{y_0,\forall \text{ odd N} \\ y_0+y,\forall \text{ even N}}} + \overbrace{(-1)^{(N-1)}}^{\substack{-1,\forall \text{ odd N} \\ +1,\forall \text{ even N}}} \times \overbrace{\left\{t - (N-1)(nt_d + t_{ndx})\right\}}^{\text{Time since the start of current Draw Operation}} u \tag{37}$$

The first term on the RHS takes one of two values $\forall N$: either y_0 or $(y_0 + y)$. The second term is a composite of two factors. The first factor takes one of two values $\forall N$: either -1 or +1, depending on the line number, and the second factor is the time since the start of the current draw operation.

During indexing, the y-position remains fixed at either y_0 or $(y_0 + y)$, depending on whether the line being drawn is even or odd.

$$\overbrace{y(t)}^{Indexing} = \overbrace{\left\{y_0 + \left[(N-1)\%2\right]y\right\}}^{\substack{y_0,\forall \text{ odd N} \\ y_0+y,\forall \text{ evenN}}} \tag{38}$$

The position of the laser during indexing operations is of academic interest and is not considered further. The position of the laser beam during drawing operations may be determined using the distance formula.

$$\overbrace{P(t)}^{Drawing} = \sqrt{x(t)^2 + y(t)^2} \tag{39}$$

Equation (39) may be expanded by substituting Equation (35) and Equation (37).

$$\overbrace{P(t)}^{Drawing} = \sqrt{\begin{aligned}&\left\{x_0 + (N-1)(\Delta x)\right\}^2 + \\ &\left\{\left\{y_0 + \left[(N-1)\%2\right]y\right\} + \left\{(-1)^{(N-1)}\left[t - (N-1)nt_h\right]u\right\}\right\}^2\end{aligned}} \tag{40}$$

Equation (40) defines the path of the laser relative to the origin as it fills a generic rectangular region using the $0-90^\circ$ hatch pattern commonly used in rapid prototyping purely in terms of the build parameters, component geometry and time. The equations of the upper bound, $P_{\max}(x,y,t)$, and the lower bound, $P_{\min}(x,y,t)$ are:

$$\begin{aligned}P_{\max}(x,y,t) &= \sqrt{\left(x_0 + N(\Delta x)\right)^2 + \left(y_0 + y\right)^2} \\ P_{\min}(x,y,t) &= \sqrt{\left(x_0 + N(\Delta x)\right)^2 + \left(y_0\right)^2}\end{aligned} \tag{41}$$

A computer program can be used to generate the discrete x and y -positions of the laser as it traverses a serpentine path across the sample. The rise in substrate temperature can be calculated by recursively running through the path.

Figure 8 shows the x and y -positions of the laser as it progresses through the build, as calculated using Equations (35) and (37). It also shows the position of the laser relative to the origin, as calculated using Equation (40), the equation that must be solved recursively to obtain the distance of the heating event from the location just under the laser. The path followed by the laser as it traverses the substrate, as calculated using Equations (35) and (37). Note that if the hatch spacing is not an integral multiple of the part dimension, the last heating event does not occur at a line end. Since this is often the case in real builds, no corrections were made for it.

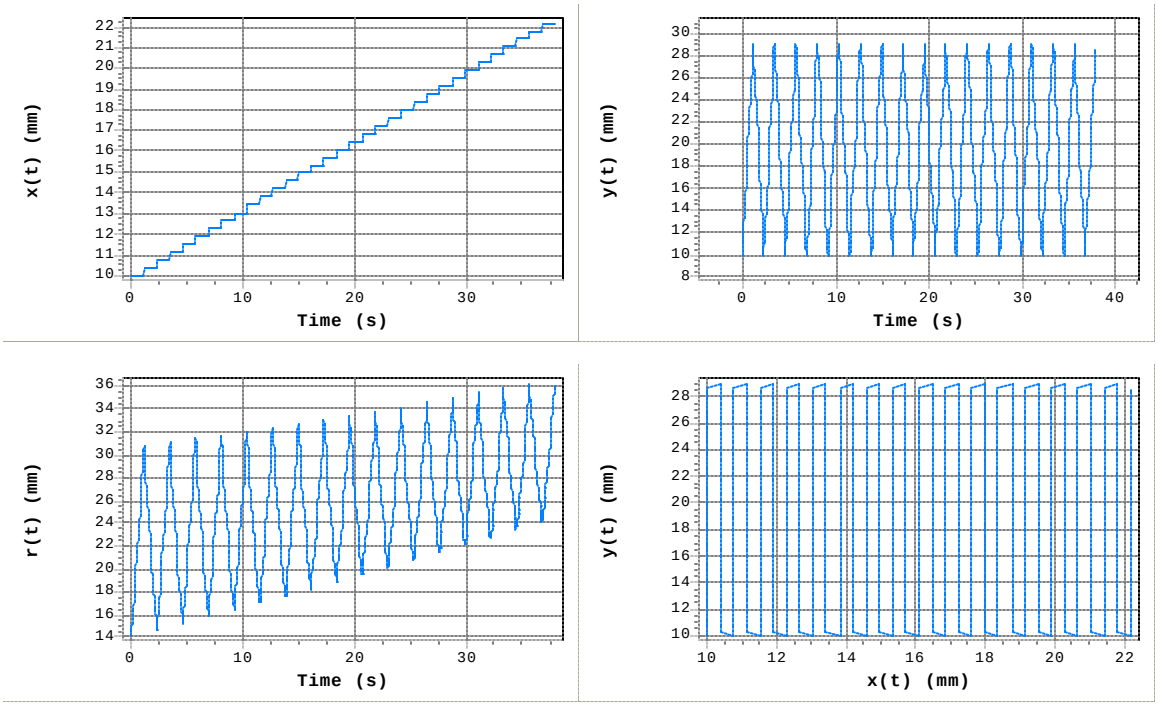

Figure 13: Laser Position

Top Left: $x(t)$ *calculated using Equation (35). Top Right:* $y(t)$ *calculated using Equation (37). Bottom Left:* $r(t)$ *calculated using Equation (40). Bottom Right:* $x(t)$ *vs* $y(t)$.

4 Experimental Methods

This section discusses the experimental methods used to validate the models. Three types of experiments were conducted to test the models: single line, 1-layer and two-layer samples were built. Single line builds allowed a wider choice in parameters because they could be conducted quickly. Since the tests take such little time, the probability of molten material sticking to the nozzles is lower than it would be for layer builds. It was not possible to use a relatively massive substrate for this set of tests, so the substrate temperature increased.

The average deposition model does not account for substrate temperature changes, so the samples built to test this model were small relative to the substrate, to ensure that substrate temperature changes were minimal during the build. The sample volume was over 1000 times smaller than the substrate volume. Since these tests took longer than single line tests, the parameter window was restricted to ensure that molten material did not stick to the nozzles and affect deposition. The two-layer experiments were performed to test the effect of substrate heating on deposition.

All experiments and measurements have some uncertainty associated with them. The first set of experiments was designed to quantify the two major sources of uncertainty – mass flow rate and height measurements.

4.1 Quantifying Uncertainty

4.1.1 Mass Flow Rate

The objective of these tests is to determine how steady the mass flow rate is on the time scale of the 1-layer and 2-layer tests. The study was designed to study the following:

- The relationship between powder motor rpm and mass flow rate.
- The repeatability of this relationship over time.
- The sensitivity to previous powder motor rpm settings.
- The sensitivity to machine shutdown and restart.
- The time required for mass flow readings to equilibrate.

To achieve these objectives, mass flow was measured in one-minute intervals for 36 minutes at every motor setting shown in Table 1. The one-minute time intervals allow several readings over the timescale of the one-layer and two-layer experiments. The builds span about 8 hours from start to finish, which is similar to the time required to carry out the single line, 1-layer or 2-layer test series. Consequently, the experiment tests the stability of mass flow rate over the term of the experiments.

Table 1 shows the powder motor rpm used in the experiment. The runs spanned just under 8 hours in total. The powder used was Ti-6Al-4V, manufactured by Pyrogenesis, Lot # 2286S-10,-22,-32, Particle Size 45-150 µm and the carrier gas used was argon at $5\,L.\mathrm{min}^{-1}$.

The one-minute time intervals allow several readings over the timescale of the one-layer and two-layer experiments. The builds span about 8 hours from start to finish, which is similar to the time required to carry out the single line, 1-layer or 2-layer test series. Consequently, the experiment tests the stability of mass flow rate over the term of the experiments.

Table 8: Order of trials testing mass flow rates

Trial	Run 1 Powder Motor rpm	Run 2 Powder Motor rpm
1	10.04	10.05
2	12.94	12.92
3	16.06	15.95
4	19.07	19.02
5	22.11	-
6	15.99	16.02
7[2]	15.99	16.02

The trials are listed in the order in which they were performed, Run 1 being performed prior to Run 2. In each run, powder motor settings were incrementally increased to a high value and then dropped to an intermediate value to test for repeatability. The final test in each run was performed after cycling the power to the machine.

4.1.2 Height Measurements

Deposition measurements for layer builds were made on multiple instruments and plotted against each other to verify whether the measurements were consistent. The substrate was washed to remove loosely adhering powders before each measurement, dried and clamped to the stages on the measuring instrument. Figure 1 shows the measurement details.

A Scanning Laser Microscope (SLM) fitted with at Keyence LC-2200 laser sensor was used to make measurements on a strip across the layer samples, taking care to include the substrate on either side. The area scanned was $22\ \mathrm{mm}$ by $1\ \mathrm{mm}$. The scan resolution was 100 µm in the measurement direction and the distance between successive scans was 41 µm. Measurements were taken at $5\ \mathrm{mm.s}^{-1}$ with an acceleration of $25\ \mathrm{mm.s}^{-2}$.

[2] The power was cycled before running these trials.

The scans were averaged to provide an "average scan" that included the substrate on either side of the sample. Ten points on either end of the sample were averaged to provide a location of a datum line, with respect to which the data points were leveled. One hundred points about the center of the scan were averaged to provide the height.

A UBM Microfocus non-contact profilometer (Solarius Development, Inc., Sunnyvale, CA) was used to make measurements on a strip 20 mm by 1 mm in the center of the sample. The scan resolution was 50 µm in the measurement direction and the distance between successive scans was 50 µm. Measurements were taken at 5 $mm.s^{-1}$ with an acceleration of 25 $mm.s^{-2}$. The measurement started on the substrate, ran across the sample width and ended on the substrate on the far side of the sample.

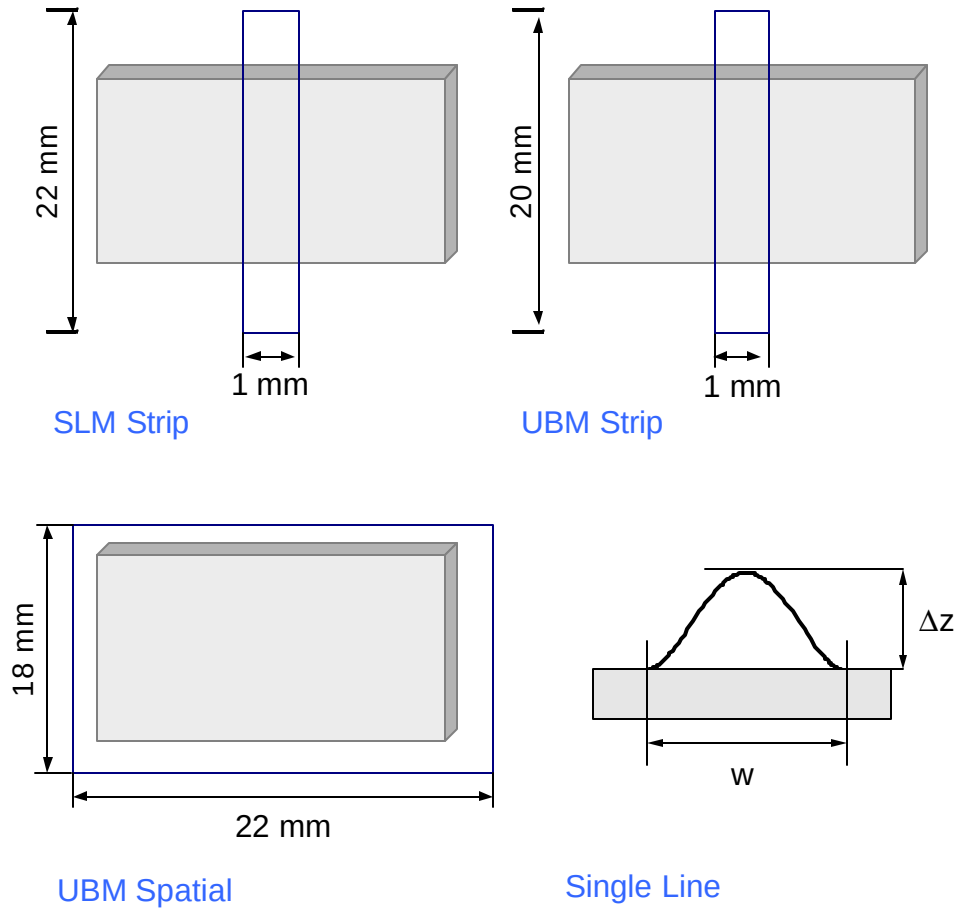

Figure 14: Measurement Details

Sample dimensions were 19.05 mm by 12.70 mm. Strip and spatial measurements were made on layer builds using a SLM and an UBM. Beads were measured once, using an optical microscope.

The thickness measurements were leveled to establish a datum on the uncoated regions of the substrate using SolarMap Universal™ software (Solarius Development, Inc., Sunnyvale, CA). The data used were taken near the center of the sample to avoid line

ends, where the stages might not have attained the set velocity. A best-fit plane was identified for the measured points on either side of the deposit (points on the substrate). The measured points for the sample were then leveled with respect to this plane. The average thickness of the points on the build surface was determined from two sets of points: one set from an arbitrary region on the surface, but away from the edges and another set from the substrate. The average distance between each set of points was reported as the deposited thickness.

Spatial deposition measurements were made for each of the 1-layer and 2-layer builds on the UBM non-contact profilometer. The measurements were made over the whole sample at 30 μm intervals. The scan velocity used was 5 $mm.s^{-1}$. The data was leveled with respect to the substrate and rotated, if necessary, to keep the sample aligned with the scan. Step height measurements were made by measuring the average z-height of an arbitrary area in the center of the sample relative to the average z-height of an arbitrary area on the substrate.

The spatial deposition measurements were saved as xyz triplets for comparison with the spatial deposition model results. The surfaces were rotated as necessary using software. A $z, z-$plot was made to compare corresponding locations on the simulated surface and the sample.

Single line builds were measured using optical methods. A cross section of the sample was photographed under a known magnification. A reticule was photographed under the same magnification to provide a pixel-distance conversion factor of 2.90 μm per pixel. The peak height of the sample was measured from the cross sections.

4.2 Deposition Experiments

All experiments were performed on a LENS™ 850 (Optomec, Inc., Albuquerque, NM). A titanium alloy; Ti-6Al-4V (Lot # 2322-SB, Pyrogenesis, Inc., Montreal, Quebec, Canada) was chosen as the material for the experiment. The material was in the form of spherical powders sieved to particle diameters between 45 μm and 150 μm .

Two sets of layer builds were made: one layer was deposited for the first set of builds, while two were deposited for the second set. The parameters were chosen so they spanned the range most often used while working with Ti-6Al-4V. Table 2 and Table 3 show the parameters used for 1-layer and 2-layer builds respectively. In all, 37 samples were made.

The geometry built for the layer tests was a rectangular block, with a width of 12.70 mm (0.5 inches), a length of 19.05 mm (0.75 inches), and a height dependant on the number of layers desired. The volume of the deposited material was intentionally kept small with respect to the substrate to provide a stable thermal mass while building and to minimize

substrate heating. It was over 1000 times smaller, for the 1-layer builds, and over 500 times smaller, for the 2-layer builds.

Laser power was measured using a hand-held power meter at both low and high power settings. The power measurements were carried out while running powder through the lines, to ensure that the readings were relevant under build conditions. The maximum power used was varied between the 1-layer builds and the 2-layer builds.

It was not possible to use the exact values for mass flow rate across builds due to current constraints in the design of the LENS™ equipment. Thus, mass flow rate measurements were taken at the start of the builds, at the end of the builds and after every set of four samples. The material was allowed to flow into a container for a period of 4 minutes and the mass of material collected was measured using a Mettler PM600 weighing balance.

In both sets of layer builds, the velocity was varied between16.9 $mm.s^{-1}$ (40 inches per minute) and 25.4 $mm.s^{-1}$ (60 inches per minute), well within the capability of the stages. In both sets of builds, the hatch spacing was varied between 0.381 mm (0.015 inches) and 0.457 mm (0.018 inches), the former value allowing significant overlap between adjacent beads and the latter value being the upper bound used in practice. In all cases, the argon center purge used to protect the optics was set at 20 $L.min^{-1}$ and the argon carrier gas used to convey the powders through the nozzles was set at 5 $L.min^{-1}$.

Single line builds were done on a rectangular sample of length 44.6 mm (1.75 inches), width 36.6 mm (1.43 inches) and height 3.2 mm (0.125 inches). Sixty four lines were drawn under different processing variable combinations. The parameter combinations used are shown in Table 4. A wider range of test parameters was possible as the tests took less time, reducing the probability of material adhering to the nozzles.

4.2.1 One-Layer Builds

Table 2 shows the parameters used during the 1-layer builds. Sixteen builds were carried out, using high-low sets of values for the parameters. The laser power was varied between 250 W and 350 W and the mass flow rate was varied between 0.038 $g.s^{-1}$ and 0.076 $g.s^{-1}$.

4.2.2 Two-Layer Builds

Table 3 shows the parameters used in the 2-layer builds. This set of sixteen builds was performed to study substrate heating. The geometry used was the same, but two layers were deposited, one over the other. The layer thickness used while slicing the files was obtained from the deposition results of the 1-layer builds. A 0°-90° pattern was used for the hatch, i.e., the direction of the fill lines in the second layer was perpendicular to those in the first layer. Samples labeled "b" are repeats because the layer thickness used was

incorrect by a small amount when building the second layer. If the error in layer thickness was indeed inconsequential, as supposed, the samples would have essentially the same height, a fact that can be verified using the height measurements.

The maximum power – $310\ W$ in this set of builds – was chosen to lie roughly mid-way between the minimum and maximum values used in the 1-layer builds. The minimum power setting was the same. The mass flow rate was varied between $31\ mg.s^{-1}$ and $76\ mg.s^{-1}$. Note that the low mass flow rates differ slightly between the two sets of builds as it was not possible to set the precise mass flow rate value on the equipment.

4.2.3 Single Line Builds

Table 4 shows the parameters used in the single line builds. This set of sixty four builds was performed to study deposition over a broader range of processing variables that would not be usable when building layers. The power was varied between $343\ W$ and $559\ W$ in this set of builds. The mass flow rate was varied between $174.9\ mg.s^{-1}$ and $228.8\ mg.s^{-1}$, well outside the usable range for layer builds. Hatch spacing was not applicable, as a single line was drawn.

4.2.4 Build Parameters

Table 9: 1-layer build parameters

Experimental Assembly	Hatch Spacing (mm)	Laser Power (W)	Mass Flow Rate (g/s)	Scan Velocity (mm/s)
1	0.381	250	0.0381	16.9
2	0.381	250	0.0381	27.5
3	0.457	250	0.0380	16.9
4	0.457	250	0.0380	27.5
5	0.381	350	0.0380	16.9
6	0.381	350	0.0380	27.5
7	0.457	350	0.0383	16.9
8	0.457	350	0.0383	27.5
9	0.381	250	0.0855	16.9
10	0.381	250	0.0855	27.5
11	0.457	250	0.0734	16.9
12	0.457	250	0.0734	27.5
13	0.381	350	0.0734	16.9
14	0.381	350	0.0734	27.5
15	0.457	350	0.0735	16.9
16	0.457	350	0.0735	27.5

Table 10: 2-layer build parameters

Experimental Assembly	Hatch Spacing (mm)	Laser Power (W)	Mass Flow Rate (g/s)	Scan Velocity (mm/s)
1	0.381	250	0.0310	16.9
2	0.381	250	0.0310	27.5
3	0.457	250	0.0310	16.9
4	0.457	250	0.0310	27.5
5	0.381	310	0.0310	16.9
6	0.381	310	0.0310	27.5
7	0.457	310	0.0310	16.9
8	0.457	310	0.0310	27.5
9	0.381	250	0.0760	16.9
10	0.381	250	0.0760	16.9
11	0.457	250	0.0760	16.9
12	0.457	250	0.0760	27.5
13	0.381	310	0.0760	16.9
14	0.381	310	0.0760	27.5
15	0.457	310	0.0760	16.9
16	0.457	310	0.0760	27.5
5b[3]	0.381	310	0.0310	16.9
6b	0.381	310	0.0310	27.5
7b	0.457	310	0.0310	16.9
8b	0.457	310	0.0310	27.5

[3] Samples labeled "b" are repeats because the layer thickness used was incorrect by a small amount while building the second layer. Height measurements later revealed that the error was so small as to be inconsequential.

Table 11: Single line build parameters

Experimental Assembly	Hatch Spacing (mm)	Laser Power (W)	Mass Flow Rate (g/s)	Scan Velocity (mm/s)
1	n/a	343	0.1749	16.93
2	n/a	415	0.1749	16.93
3	n/a	487	0.1749	16.93
4	n/a	559	0.1749	16.93
5	n/a	343	0.1749	21.17
6	n/a	415	0.1749	21.17
7	n/a	487	0.1749	21.17
8	n/a	559	0.1749	21.17
9	n/a	343	0.1749	25.40
10	n/a	415	0.1749	25.40
11	n/a	487	0.1749	25.40
12	n/a	559	0.1749	25.40
13	n/a	343	0.1749	29.63
14	n/a	415	0.1749	29.63
15	n/a	487	0.1749	29.63
16	n/a	559	0.1749	29.63
17	n/a	343	0.1896	16.93
18	n/a	415	0.1896	16.93
19	n/a	487	0.1896	16.93
20	n/a	559	0.1896	16.93
21	n/a	343	0.1896	21.17
22	n/a	415	0.1896	21.17
23	n/a	487	0.1896	21.17
24	n/a	559	0.1896	21.17
25	n/a	343	0.1896	25.40
26	n/a	415	0.1896	25.40
27	n/a	487	0.1896	25.40
28	n/a	559	0.1896	25.40
29	n/a	343	0.1896	29.63
30	n/a	415	0.1896	29.63
31	n/a	487	0.1896	29.63
32	n/a	559	0.1896	29.63

Continued…

Table 11 Continued…

Experimental Assembly	Hatch Spacing (mm)	Laser Power (W)	Mass Flow Rate (g/s)	Scan Velocity (mm/s)
33	n/a	343	0.2092	16.93
34	n/a	415	0.2092	16.93
35	n/a	487	0.2092	16.93
36	n/a	559	0.2092	16.93
37	n/a	343	0.2092	21.17
38	n/a	415	0.2092	21.17
39	n/a	487	0.2092	21.17
40	n/a	559	0.2092	21.17
41	n/a	343	0.2092	25.40
42	n/a	415	0.2092	25.40
43	n/a	487	0.2092	25.40
44	n/a	559	0.2092	25.40
45	n/a	343	0.2092	29.63
46	n/a	415	0.2092	29.63
47	n/a	487	0.2092	29.63
48	n/a	559	0.2092	29.63
49	n/a	343	0.2288	16.93
50	n/a	415	0.2288	16.93
51	n/a	487	0.2288	16.93
52	n/a	559	0.2288	16.93
53	n/a	343	0.2288	21.17
54	n/a	415	0.2288	21.17
55	n/a	487	0.2288	21.17
56	n/a	559	0.2288	21.17
57	n/a	343	0.2288	25.40
58	n/a	415	0.2288	25.40
59	n/a	487	0.2288	25.40
60	n/a	559	0.2288	25.40
61	n/a	343	0.2288	29.63
62	n/a	415	0.2288	29.63
63	n/a	487	0.2288	29.63
64	n/a	559	0.2288	29.63

5 Results and Discussion

5.1 Quantifying Uncertainty

5.1.1 Uncertainty in Mass Flow Rate

Figure 1 shows the results of the mass flow rate consistency experiments. The compiled numbers are in Table 1. Note that the powder motor rpm's are close, but do not exactly match across runs, as there is no way to set a mass flow rate to a value.

Table 12: Results of the mass flow rate consistency tests

rpm	Run 1 (g/min)	Run 1 (g/s)	rpm	Run 2 (g/min)	Run 2 (g/s)
10.04	8.27	0.138	10.05	8.09	0.135
12.94	10.06	0.168	12.92	10.02	0.167
16.06	11.74	0.196	15.95	11.65	0.194
19.07	13.36	0.223	19.02	13.30	0.222
22.11	15.32	0.255	16.02	11.66	0.194
15.99	12.02	0.200	-	-	-
15.99	11.73	0.196	16.02	11.55	0.193

It is immediately apparent from the figure that the mass flow rate, once set, attains equilibrium after about 10 minutes, especially at lower mass flow rates. Thus, to be reasonably certain of the mass flow rate, a wait of 10 minutes is recommended after changing the powder motor rpm.

It is apparent that the mass flow rate is not constant with time. Taking Run 1 as an example, at mass flow rates above 0.22 g/s (~19 rpm), there appears to be a slight increase in mass flow rate with time. At a mass flow rate of 0.22 g/s, the mass flow rate increases at a rate of about 2.78E-05 g/s/min, which is a measure of the uncertainty in this parameter. The highest rate of change of mass flow was 1.42E-04 g/s/min at 0.25 g/s (~22 rpm), at the limits of the machine's ability to deliver material. This was reversed in Run 2, where the slope seems more pronounced at the lowest mass flow rate. This may have very little effect for small builds, but the increase in mass flow rate with time could cause an appreciable change in the material available over long builds.

It is also apparent that the relationship between powder motor rpm and mass flow rate is not entirely repeatable either between runs or between trials (see Figure 1: Transient behavior of mass flow rate. Considering Run 1, setting the motor rpm to 15.99 produces a mass flow rate between 0.1955 g/s and 0.2003 g/s depending on whether the motor rpm

was initially higher, lower, or zero before the change was made. The relationship also appears inconsistent between runs. For example, the mass flow rate measured at 10.05 rpm in run 2 is lower than the mass flow rate measured at 10.04 rpm in Run 1.

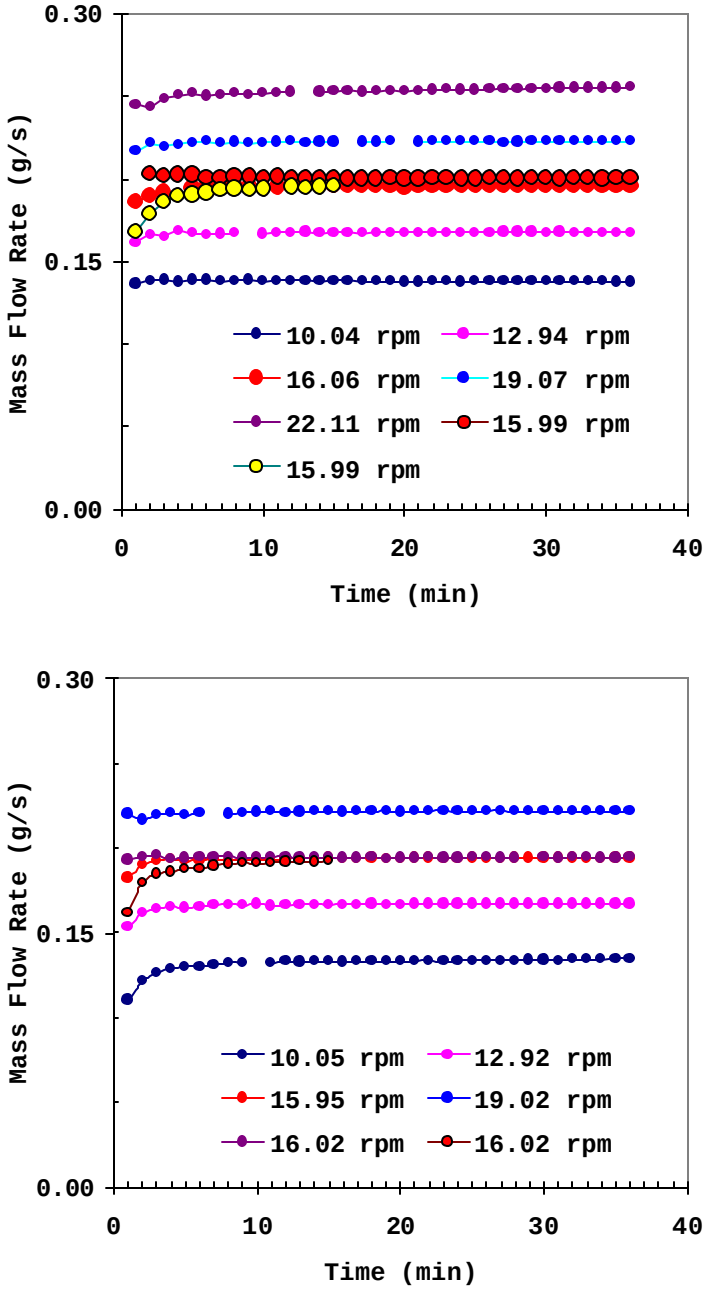

Figure 15: Transient behavior of mass flow rate

Top: Run 1, lasting a total of 4.2 hours. Last trial of 15.99 rpm was run after cycling machine power. Bottom: Run 2, lasting a total of 3.6 hours. Last trial at 16.02 rpm was run after cycling machine power. Weight measurements were taken at 1-minute intervals in all cases.

The equilibrium mass flow rate appears to be nearly independent of the previous motor rpm setting. In Run 1, when the motor rpm was increased from 13 to 16 rpm, the equilibrium mass flow rate was 0.196 g/s. When it was decreased from 22 to 16 rpm, the equilibrium mass flow rate was 0.200 g/s – an almost imperceptible change. Shutting the machine down and restarting it also appeared to have little effect.

One drawback of this experiment is that it cannot detect real-time fluctuations in mass flow rate, as the measurements were made periodically. Real-time oscillations in mass flow rate could cause variable deposition that result in uneven surfaces.

The following conclusions were drawn from the experimental results:

- Mass flow rate appeared to be nearly constant approximately 10 minutes after the command to change it had been made.
- The mass flow rate could change once this period has elapsed. The magnitude of the change appeared dependent on time.
- Mass flow rate appeared influenced by the previous motor setting.
- Mass flow rate measurements appeared influenced by machine shut down.
- The mass flow rate measurements appeared to vary between runs.

5.1.2 Uncertainty in Height Measurements

Figure 2 shows cross sections of single-lines laid down under increasing laser power. Re-melted regions lie below the plane of the substrate and newly deposited material lies above it. The re-melted volume appears larger than newly deposited volume, indicating that a significant amount of energy is expended in substrate heating. The height difference between the peak and the substrate is reported as the deposited height for single-line tests. This value is higher than the results for layer tests, because an average height is reported for the layer tests.

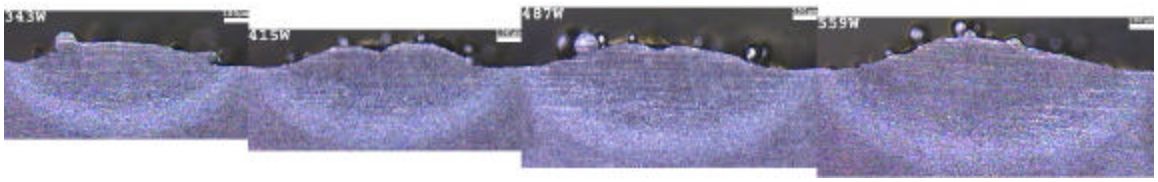

Figure 16: Typical deposition results for single-lines

Laser power increases from left to right. Increasing laser power increases deposition and the heat-affected zone. Samples have been lined up to aid comparison.

Figure 3 shows a typical surface as measured by the UBM profilometer. The sample is in the center of the image, surrounded by the substrate. The figure has been leveled with respect to the substrate. The laser traverses the sample in the east-west direction, resulting in hot regions at the ends of every line. Increased deposition occurs in these regions, which are colorized yellow or red.

The raised regions visible in the east-west direction are the beads laid down by the laser, since the number of beads on the sample match the number of beads calculated using $x/\Delta x$. Small islands are visible within each bead, which appear to be partially melted powders adhering to the surface.

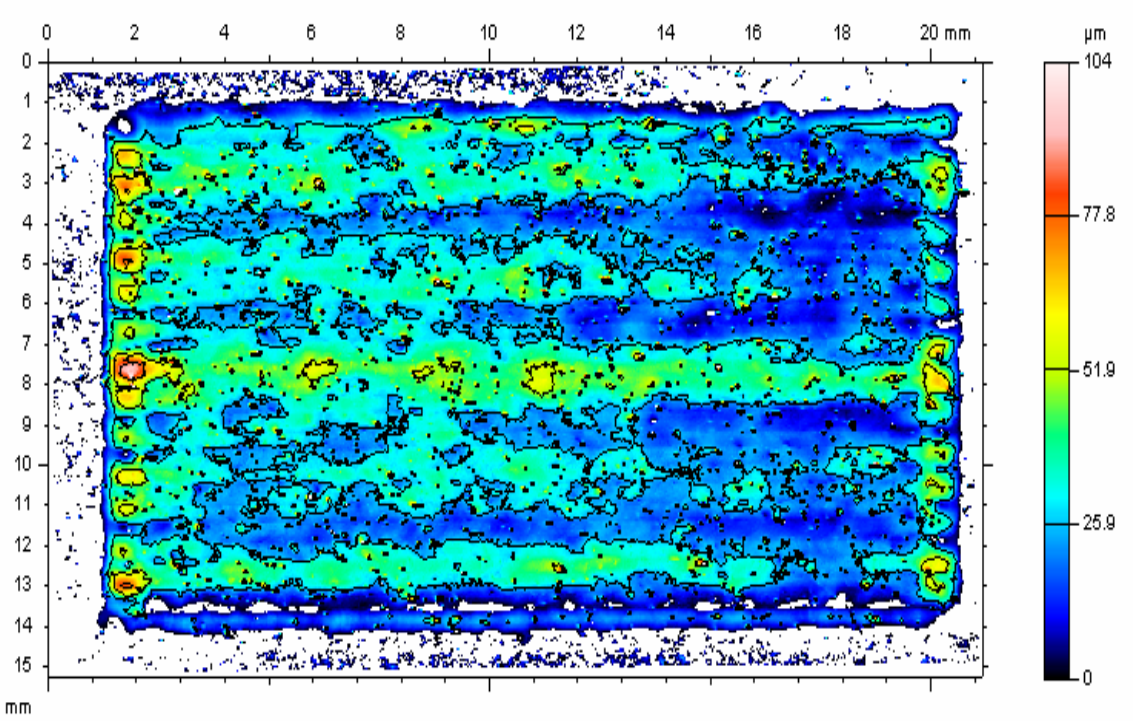

Figure 17: A typical surface measured using the UBM

The sample has been leveled with respect to the substrate. The raster lines are clearly visible, going from left to right. Note the increased deposition in the ends due to substrate heating. Also note the absence of the last raster at the bottom of the sample, probably due to a round off error in the slicing software.

As the deposited surfaces are highly reflective, the sensors were sometimes unable to take a reading at the desired point. These unmeasured points are not visible in this figure, but appear as sharp peaks in isometric views. They are clearly taller than any visible feature on the surface and are probably measurement artifacts. These artifacts were not removed by filtering to minimize loss of information. Since the reported thickness is averaged from several thousand points, the effects of these aberrations on the reported thickness are assumed small.

Since the deposition heights for the layer builds were under 300 µm, measurements were made on different instruments to reduce uncertainty. Figure 4 shows the comparison between these measurements. If the instruments agree with each other, a height-height plot should have unit slope, zero intercept and a correlation coefficient of unity.

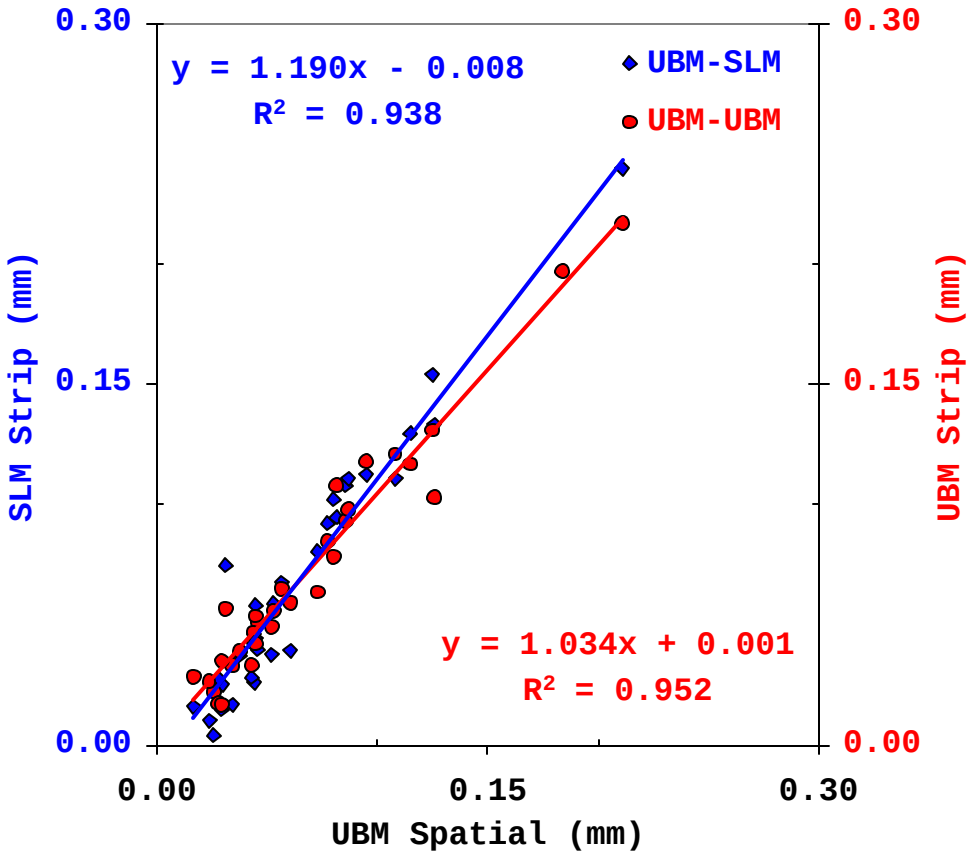

Figure 18: Deposition Height Comparison

The figure contains data from 1-layer and 2-layer builds. Left axis shows the comparison of UBM spatial measurements to the SLM strip measurements. Right Axis shows the comparison of UBM spatial measurements to UBM strip measurements.

A plot of UBM spatial measurements versus UBM strip measurements shows a straight line relationship with an intercept of 1 µm, which is identical to the vertical resolution of the UBM sensor. The correlation coefficient is above 0.95 and the slope of the line is 1.03, indicating that the measurements are almost identical.

A plot of UBM spatial measurements versus SLM strip measurements shows a straight line relationship with an intercept of 8 µm, just under the 12 µm vertical resolution of the SLM sensor. The slope of the line is 1.19 and the correlation coefficient is 0.94, indicating that the measurements are slightly scaled, but otherwise identical. The deposition results appear to correlate closely, indicating that an average measurement may be used to test the average deposition model.

5.2 Material Delivery Model

Figure 5 is a plot of z versus the mass for the single line builds. The ratio $\sqrt{\frac{\dot{m}}{u}}$ is plotted on the abscissa, and the average deposited height measured is on the ordinate. Deposition is expected to increase with this ratio under constant laser power, and the plots for single-line builds appear to confirm this. Data points seem to fall on lines segregated by the laser power and deposition appears to increase with this ratio.

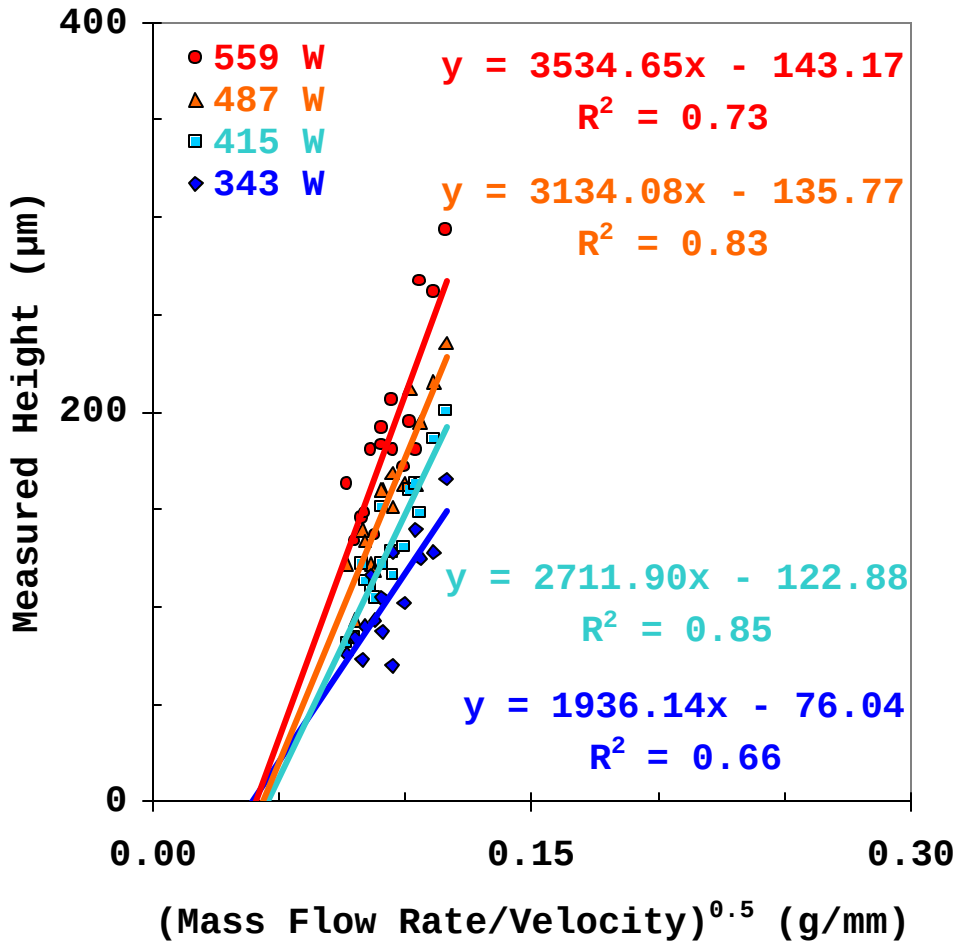

Figure 19: Build Parameters vs Measured Height – single line builds

Single Line Builds: The lines appear segregated by the laser power used.

Each line in the figure has 16 data points on it. Regression lines were drawn for each line. The correlation coefficients of these lines lie between 0.66 and 0.85. Examination of the outliers suggests that correlation coefficients are sometimes skewed by one errant data point. A possible reason for why the correlation coefficients are not higher is that it was not possible to let the mass flow rate stabilize for 10 minutes before each sample was

built. A 10 minute wait to allow mass flow rate to stabilize before each of the 64 tests would have added a prohibitive 11 hours to the experiment.

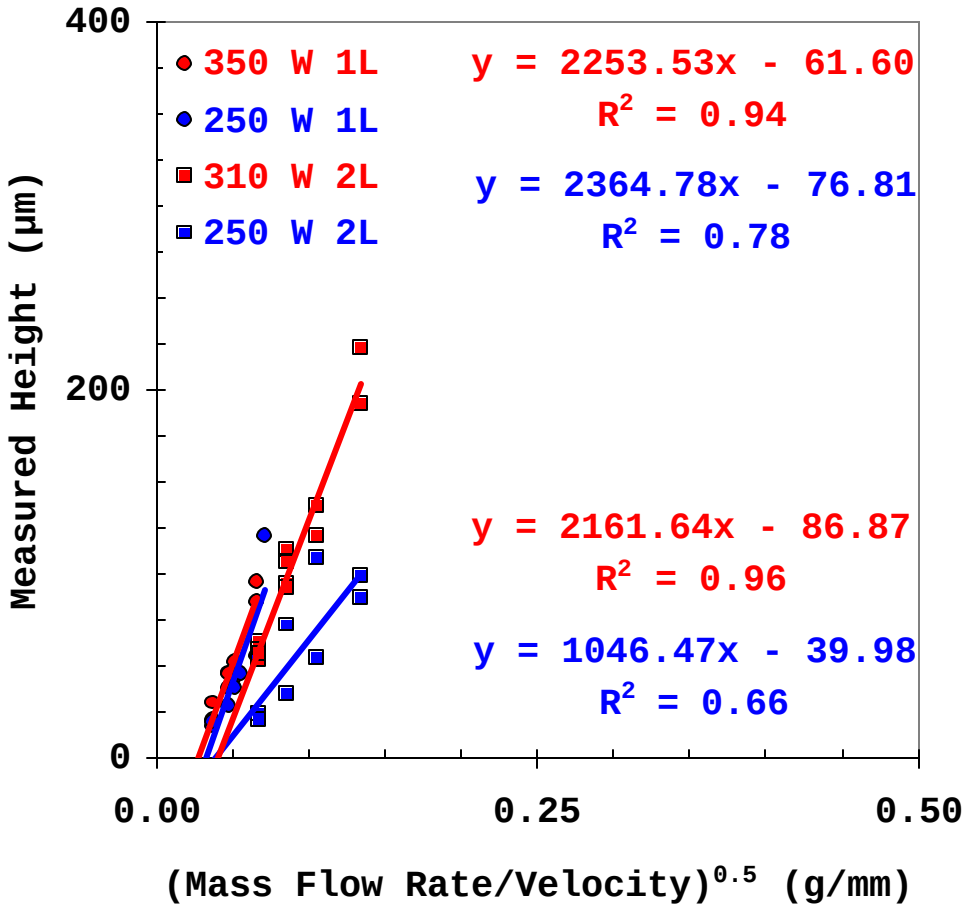

Figure 20: Build Parameters vs Measured Height – Layer builds

The lines appear segregated by both laser power and number of layers built. Segregation is expected because these variables affect the energy available.

Figure 20 shows the deposition measurements plotted against for the ratio $\sqrt{\frac{\dot{m}}{u}}$ for layer builds. As before, layer builds made under different laser powers are expected to lie on different lines. Additionally, since substrate heating can be significant for layer builds, the one-layer results should fall be differentiable from the two-layer builds, especially for two-layer builds. The data for the one-layer builds appears to segregate based on laser power, consistent with single line build results, but the lines are almost superimposed, because the builds were carried out under near-isothermal conditions. The regression coefficients are much higher than those for the single lines and fall between 0.66 and 0.96, the lower value being due to one outlier. The higher correlation coefficients relative to those for the single lines are probably because mass flow rate was allowed to

equilibrate for 10 minutes between tests. Since the one-layer builds were made under near-isothermal conditions, the lines are almost indistinguishable from each other.

Two-layer builds show the same trends as 1-layer builds. The data appear linear, as predicted, and segregate with laser power, though the line through the low power data points appears skewed by two outliers. As predicted by the material delivery model, data points within each line appear independent of whether or not a high mass flow rate was used. Since the mass flow rate varies by a factor of two during both sets of layer experiments, this observation lends support to the model.

The regression lines for both single line and layer builds appear to make a small, positive intercept averaging $0.038\ g m m^{-1}$ with the abscissa (see Table 2). Since zero deposition is expected at zero mass flow rates, the existence of an intercept appears contradictory. The magnitude of the intercept is small and could be explained by the fluctuations discussed in the Uncertainty in Mass Flow Rate section.

Table 13: X-Intercepts and Slopes for Material Delivery Model

Laser Power (W)	Build Type	X-axis Intercept (g/mm)	Slope = K_M $(mm^3/g)^{0.5}$
250	1-Layer	0.032	1046
250	2-Layer	0.038	2364
310	2-Layer	0.040	2161
343	Single Line	0.039	1936
350	1-Layer	0.027	2253
415	Single Line	0.041	2711
487	Single Line	0.043	3134
559	Single Line	0.045	3534
Average		**0.038**	

The slopes of the regression lines listed in Table 13 are equivalent to K_M, which is equal to $\sqrt{\left(\frac{C_{AL}}{C_{CS}C_{AM}}\right)\left(\frac{d_{melt}}{d_{pwdr}}\right)^2\frac{f_1}{r}}$, according to the material delivery model. Since the lines evidently have different slopes, one or more terms within K_M must be affected by laser power. Intuitively, the diameter of the melt pool, d_{melt} is expected to increase with the laser power, which could explain the steeper slopes at increasing laser powers. At the critical power required to create a melt pool, the diameter of the melt pool is zero, driving K_M to zero. Therefore, the critical power required to initiate melting can be obtained by plotting K_M versus laser power and extrapolating the regression line to zero, as shown in Figure 7. The intercept obtained for critical power is 65 W, low, but consistent with experimental observations. One outlier has been omitted from the chart.

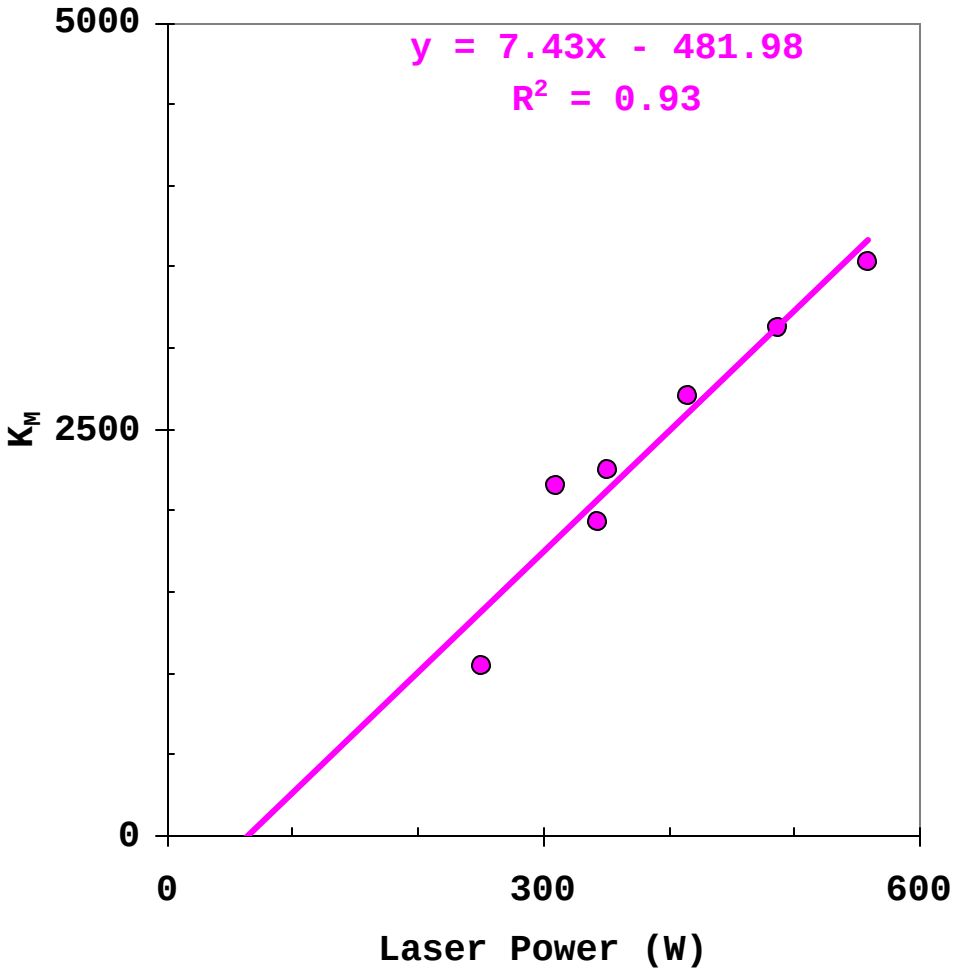

Figure 21: Determination of Critical Power to initiate melting

A plot of K_M *versus the laser power indicates a critical power of about 65 W is required to initiate melting under typical experimental conditions, a value consistent with experimental observations.*

5.3 Average Deposition Model

The average measured heights for single-line builds ranged between 70 µm and 294 µm. The average measured heights for the 1-layer builds ranged between 17 µm and 121 µm, and the average measured for the 2-layer builds ranged between 20 µm and 223 µm.

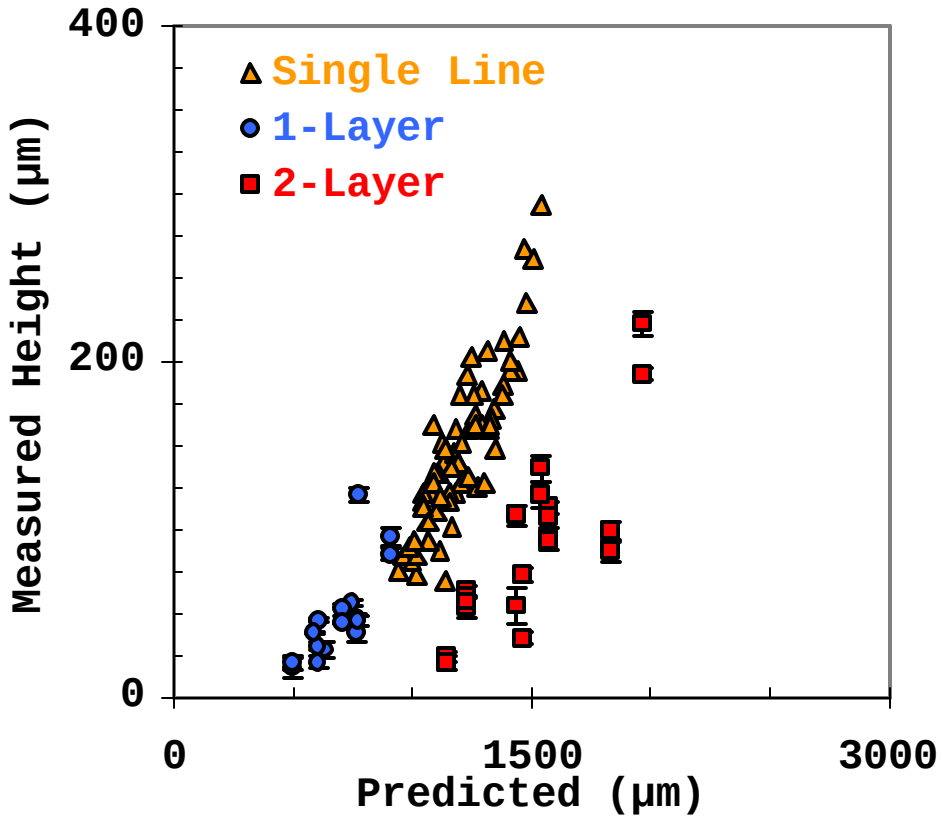

Figure 22: All data - Predicted versus Measured Deposition

As expected, the data appear to group with temperature-related variables in the single line and two-layer builds, because they were carried out under non-isothermal conditions

The predictions are plotted against the measured values in Figure 22. The scatter bars on the layer results span 2 standard deviations and represent the variation in measurements reported by the measurement instruments. Since single line results were measured only once, scatter bars are irrelevant. The largest range in standard deviations was 28 µm, for one-layer builds and 8 µm for two-layer builds.

Increasing substrate temperature would increase the energy available for deposition. Since this model does not account for increases in substrate temperature, predictions would be affected by non-isothermal conditions during the build. Lines that fall on top of each other indicate builds that were carried out in essentially isothermal conditions.

Regression lines are not shown in this figure to reduce clutter, but will be discussed for each set of builds individually. Since the two-layer builds are known to have non-isothermal conditions, predictions are expected to fall on separate lines.

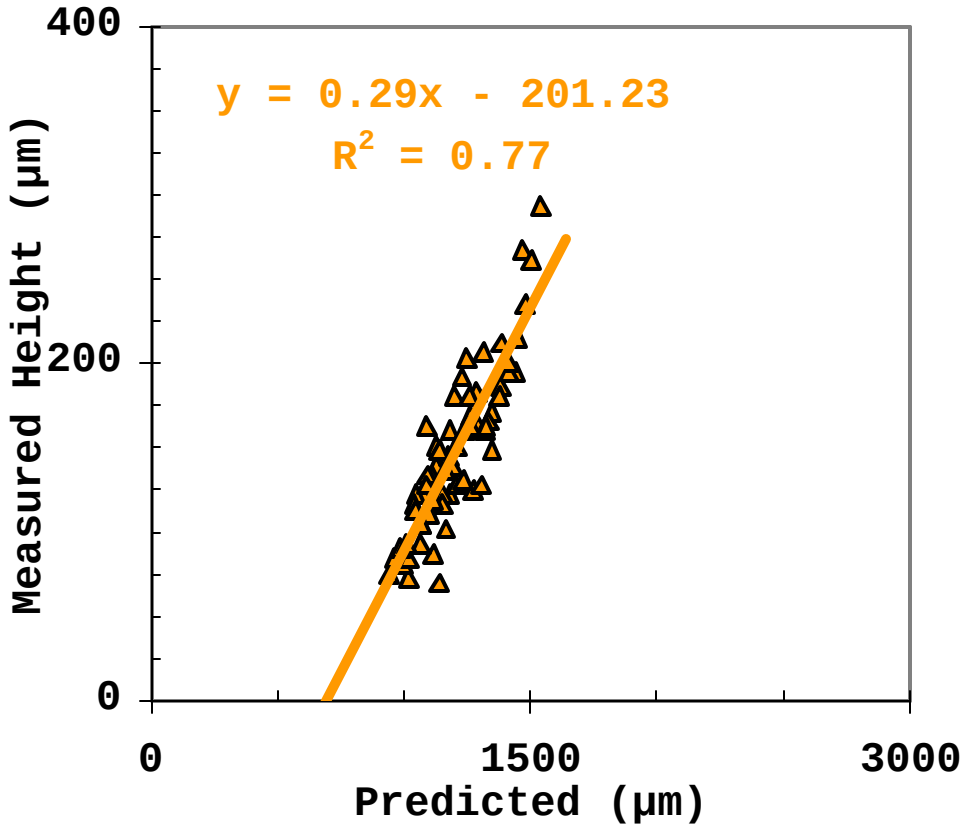

Figure 23: Single Line - Predicted versus Measured Height

The single-line data appear linear. Reasons for the scatter include non-isothermal build conditions and variations in the mass flow rate.

Figure 23 shows the performance of the ADM on the single line tests and the data shown is a subset of Figure 22. The regression line is based on 64 height measurements. The correlation coefficient is 0.77, which could be considered fair, and the line makes a positive intercept with the x-axis. The experimental method used may be responsible for some of the scatter. It was not possible to wait 10 minutes after changing the mass flow rate setting to ensure a constant mass flow rate, a time the previous section recommends. Doing so would have added a prohibitive 11 hours to the experiment. Thus, the variability in mass flow could account for some of the scatter.

Ideally, the line between the predicted and the measured values would have unit slope, zero intercept and a regression coefficient of 1.0. The slope is 0.29, is considerably lower than predicted and the intercept is positive. One reason for the positive intercept could be because neither radiative nor convective heat loss is accounted for by the model. Including these modes of heat loss would reduce the available power, lowering the

predictions and shifting the line to the left. Another reason the predictions are higher than the measurements is that the value of f_1, the fraction of material reaching the melt pool, is known to be less than the value 1.0 used to generate the prediction. Though f_1 is unknown, lowering it would lower the prediction, also shifting the line to the left.

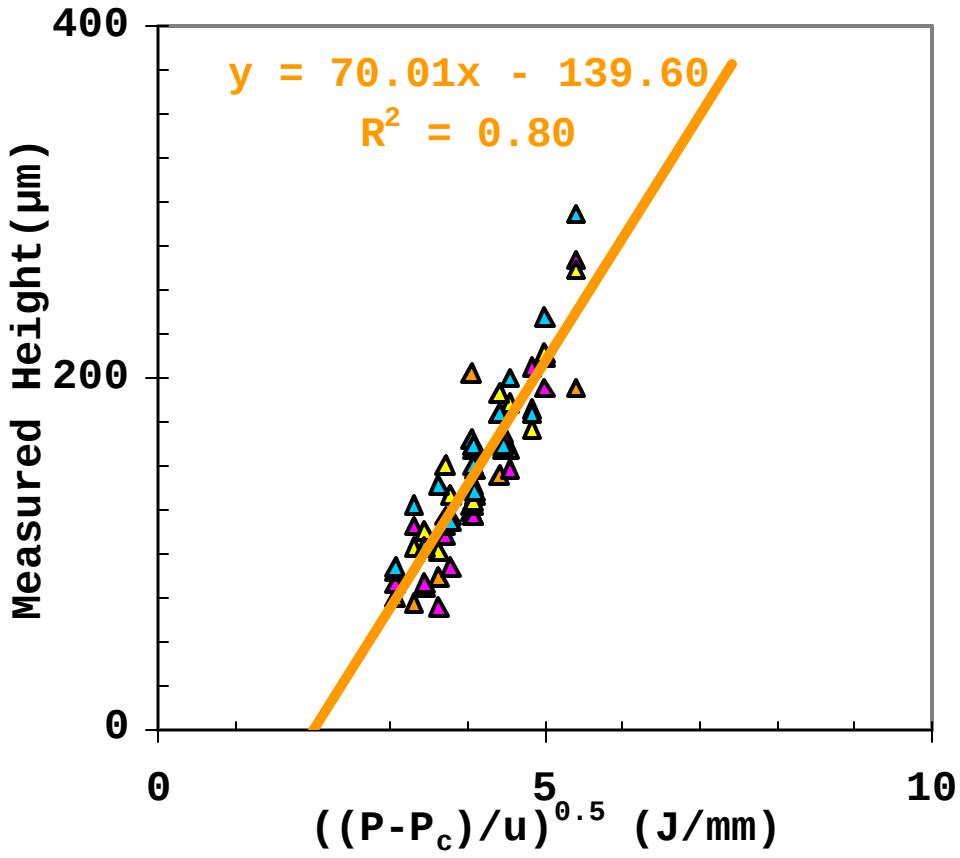

Figure 24: Single Line results plotted versus energy terms at different mass flow rates

The ADM predicts a linear relationship between deposition and $\sqrt{\frac{(P-P_c)}{u}}$. *The deposition measurements for single-line builds appear to support this. The slope is related to the reciprocal square root of the shape factor of the bead cross section. Since the data all appear to fall on a line, the bead cross section appears not to change and just scales uniformly with mass flow rate.*

Figure 24 shows the results for the 64 single line builds plotted against variables known to affect energy, and the results are expected to be linear. The line has a good correlation coefficient of 0.80, consistent with the predictions of the model. The slope of the line is proportional to $\sqrt{\frac{1}{C_{CS}}}$. Since the deposition measurements appear to fall on the same line irrespective of the mass flow rate in use, the shape factor relating the height of the deposition to the area of cross section of the bead is constant. In short, the bead geometry

does not change appreciably. Therefore, under increasing mass flow rates, the bead dimensions appear to scale uniformly in the $xz-$plane.

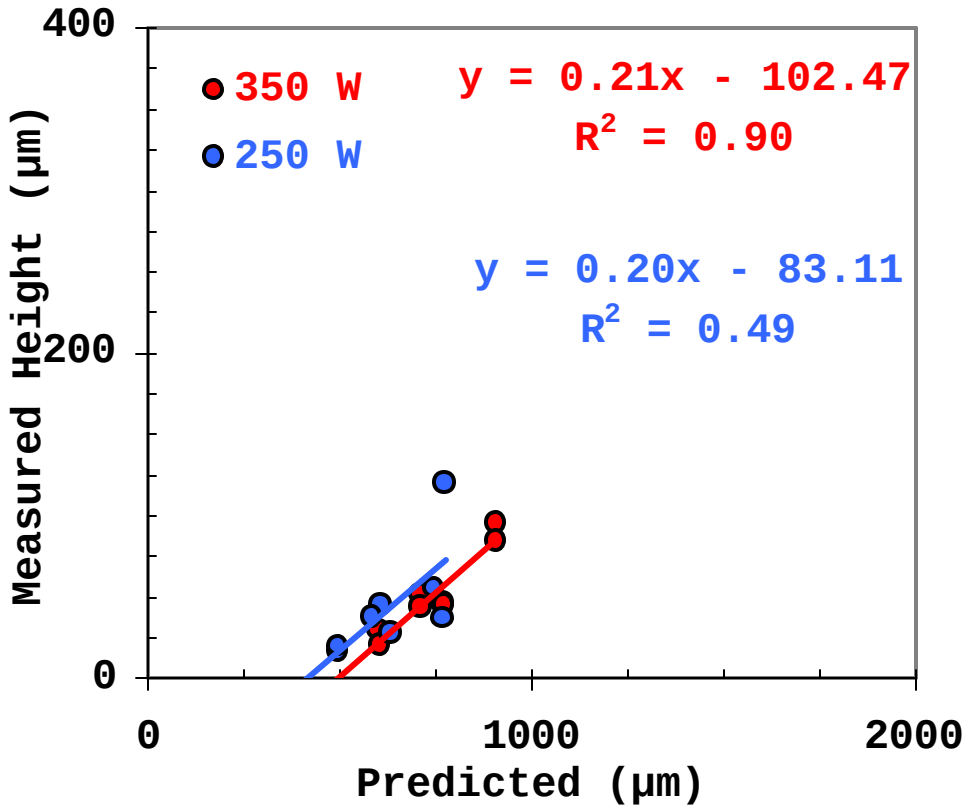

Figure 25: 1-Layer builds – Predicted versus Actual Deposition

The 1-layer data do not segregate with energy terms, consistent with substrate temperature being held relatively constant during the builds.

The average deposition model is expected to perform better on single layer builds, as they were made on a relatively massive substrate and should have experienced little temperature rise. The predictive performance of the model applied to the one-layer builds is shown in Figure 25. The results are shown segregated by laser power, but the lines are nearly identical, and a straight line could plausibly be drawn through the data. Indeed, the straight line could plausibly be drawn through all the data, consistent with the builds being carried out under essential isothermal conditions. As before, the lines make a positive intercept with the x-axis, probably for the same reasons.

The slopes in Figure 25 (approximately 0.21) are lower than those reported for the single line builds in Figure 23 (approximately 0.29). One reason for this is that the measurements used in Figure 23 report the peak height of a bead. In layer builds, the re-melting of beads as the laser makes successive passes lowers the peaks and fills the valleys.

Figure 12 shows the predictive capabilities of the model when applied to two-layer builds that necessarily experience substrate heating. The data segregate with laser power, as anticipated, indicating that the model cannot be applied in cases where substrate heating is significant. The correlation coefficient of the lower line is 0.56, which is poor. Closer inspection of the line indicates that it is thrown off by one outlier. The correlation coefficient of the upper line, in contrast, is 0.91.

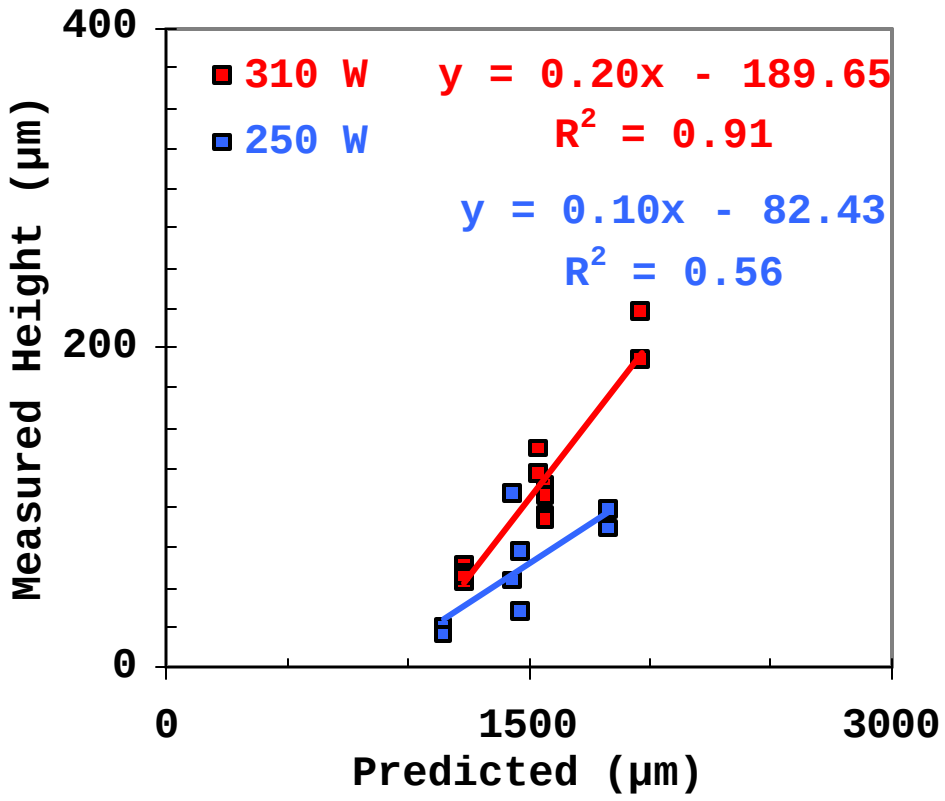

Figure 26: 2-Layer builds - Predicted versus Actual Deposition

The 2-layer data segregate with laser power, as expected, consistent with substrate temperature varying during the builds.

The ADM predicts a linear relationship between deposition and $\sqrt{\frac{(P-P_c)}{u}}$. The deposition measurements for layer builds appear to support this. The slope is related to the reciprocal square root of the shape factor of the bead cross section, which, unlike in single lines, appears to be dependent on the mass flow rate during the build (see Figure 13). This may be because consecutive lines overlap, causing re-melting of the previously deposited bead. The low correlation coefficient in the 1-layer builds at 74 mg/s is due to one outlier.

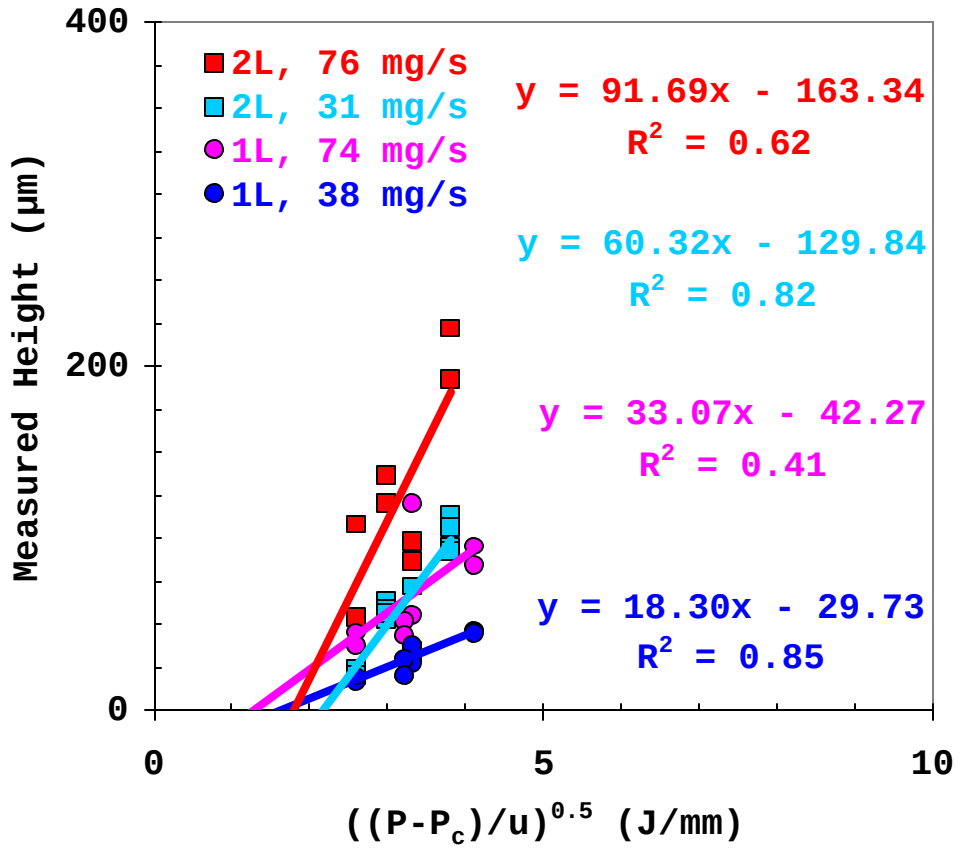

Figure 27: Layer Buildresults plotted versus energy terms at different mass flow rates

The ADM predicts a linear relationship between deposition and $\sqrt{\frac{(P-P_c)}{u}}$ *. Deposition measurements for layer builds appear to support this. The slope is related to the reciprocal square root of the shape factor of the bead cross section. The bead cross section appears affected by the mass flow rate, when consecutive lines overlap.*

The substrate temperature was not measured during the experiment, but can be estimated, using the thermal properties of the substrate and the build parameters. Figure 14 is a plot of the calculated substrate temperature rise versus deposition. At a given mass flow rate, deposition is expected to increase with temperature, an expectation that appears to be supported by the experimental results. This is especially true of the one-layer builds. The data appear to segregate with mass flow rate with just one outlier at 734 mg/s.

The two-layer builds show the same trend at 310 mg/s, with just one outlier. The results for two-layer builds at 760 mg/s are muddled, samples 9-12 inclusive apparently falling on a different line. These samples were built sequentially after restarting the machine and it could be that the substrate was cooler when those samples were built.

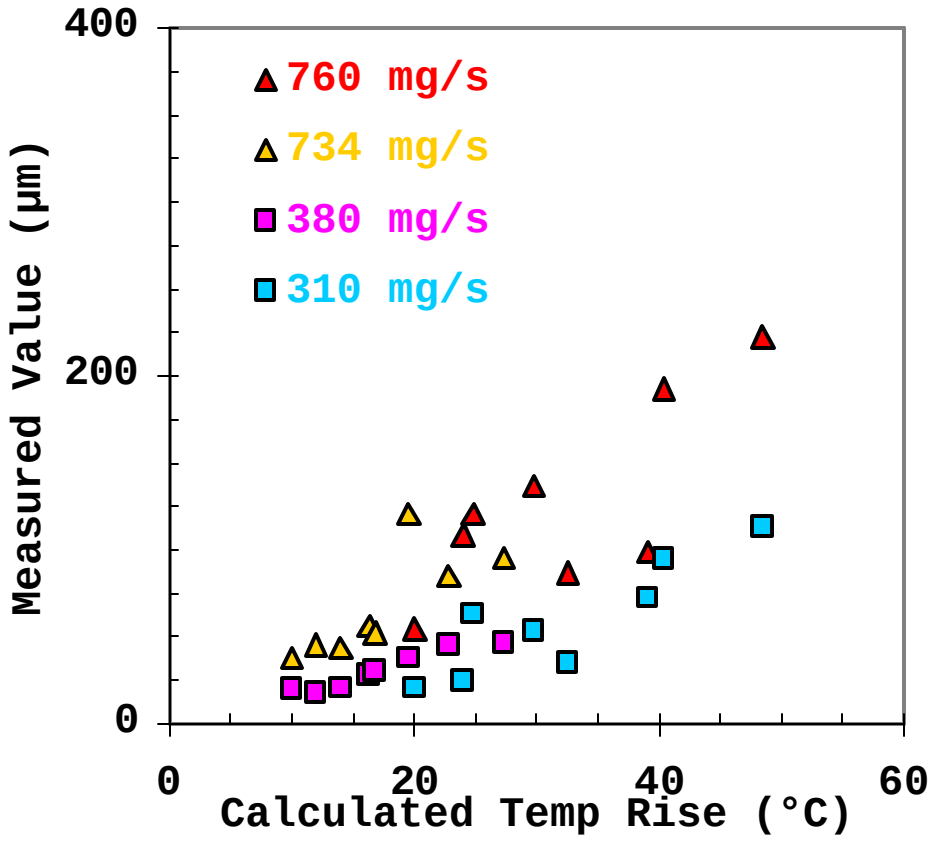

Figure 28: Effect of Calculated Substrate Temperature Rise

At constant mass flow rate, increasing temperature seems to cause an increase in deposition. The low mass low rate results are differentiable from the high mass flow rate results.

The following conclusions may be drawn from the experimental results:

1. The average deposition model appears capable of estimating deposition for single lines, one-layer builds and two-layer builds.
2. The predictions appear dependent on variables that affect substrate temperature, so the model performs better on builds with little change in substrate temperature.
3. Deposition seems related to the calculated average substrate temperature, at least below 60°C.

5.4 Spatial Deposition Model

Figure 15 shows a typical temperature profile predicted by the spatial deposition model. It is important to note that this is not the temperature of the layer at a fixed time. Rather, it is the temperature of the location just under the laser just before the laser passes over it.

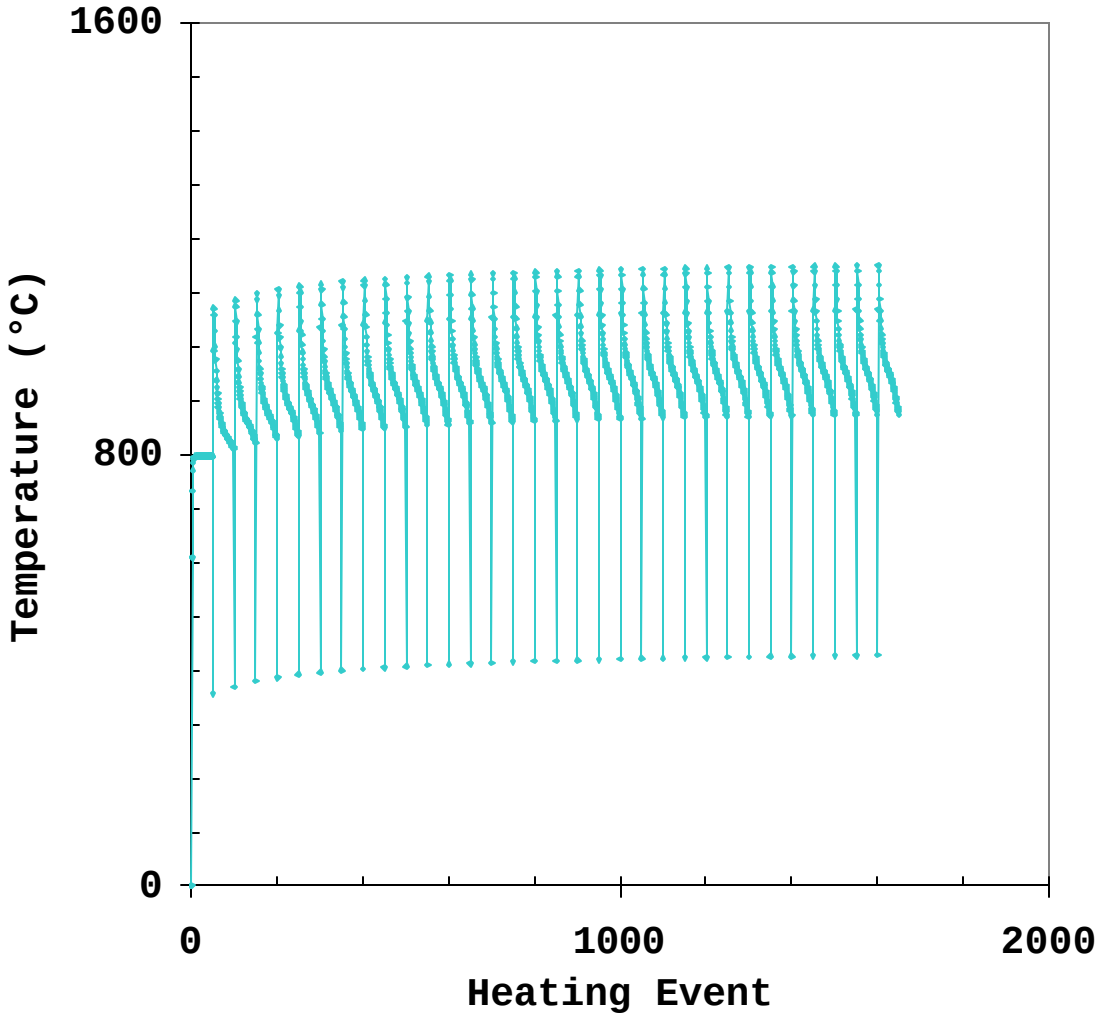

Figure 29: Calculated Temperature at Heating Event Locations

Each point on the chart is the calculated temperature of the substrate just before the laser reaches it. This is not the temperature of the layer at a fixed time; rather, it is the temperature of the location just under the laser at the time the laser reaches it. Each peak corresponds to the laser reversing direction at the end of a line. In this case, there are 32 lines (corresponding to 32 peaks) and a total of 1650 heating events.

The number of the heating event (its order in time) is plotted on the $x-$axis and the calculated temperature rise due to a combination of substrate heating and direct energy input from the laser is plotted on the $y-$axis. Peaks occur at the ends of lines, as the laser reverses direction. The sharp drops at the ends of each line are thought to be due to round off errors at line ends, since the hatch spacing is not necessarily an integral multiple of the sample dimension. In this respect, the simulation matches the build – examination of the deposited surface sometimes shows that a raster line was not drawn.

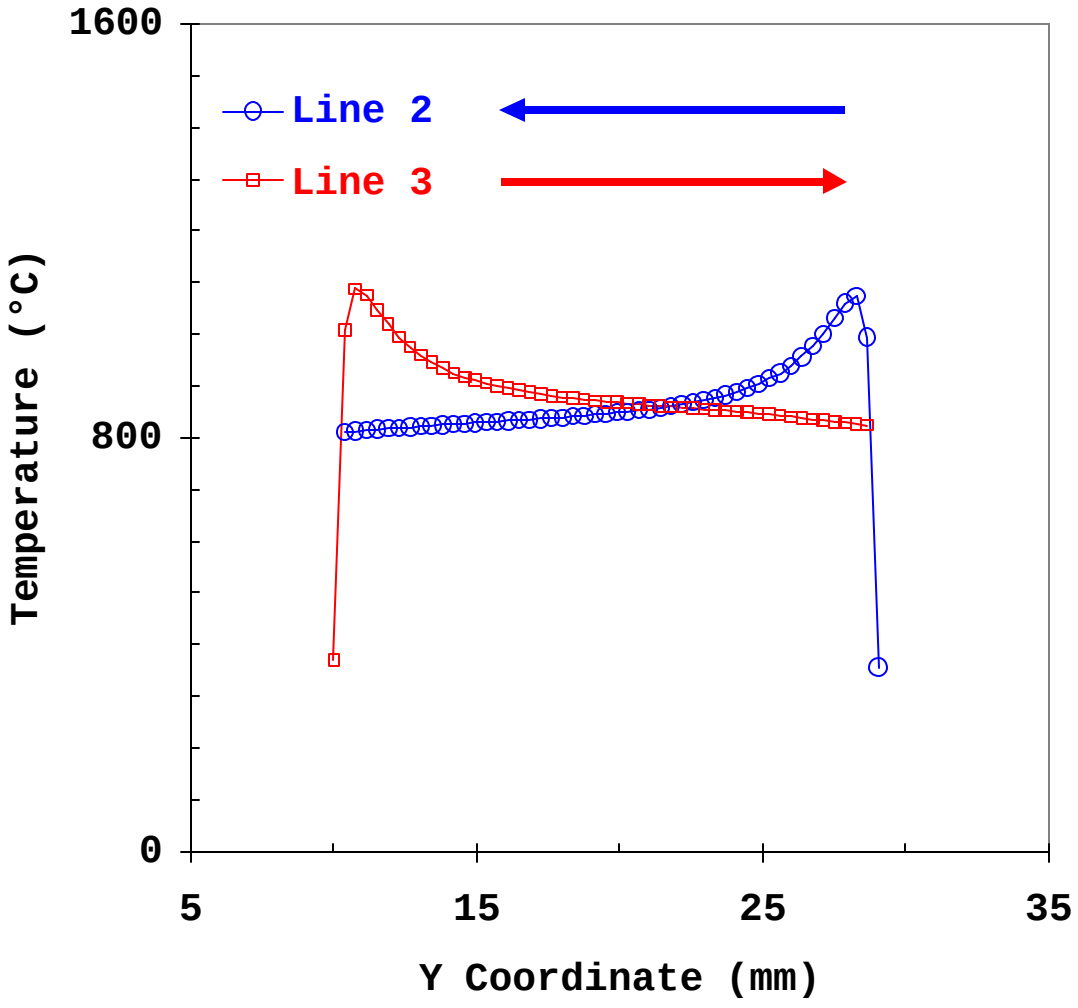

Figure 30: Calculated Substrate Temperature Increase for Two Lines

Each line represents the calculated substrate temperature at a y-coordinate just before the laser reaches it. Peak temperatures occur at the tail of the lines. Line 3 is marginally hotter than line 2. In this case, the y-coordinate is in the east-west direction.

Figure 30 shows the calculated substrate temperature under the laser at the time the laser passes over each point on lines 2 and 3. The laser has just drawn the first line and is returning in the $-y$ direction as it draws the second line. As expected, the tail of the line

is heated more than the end of the line (right peak). The laser reaches the border and reverses direction to draw the third line. Once again, the tail of the line is where peak temperatures occur – near the border. As expected, the peak temperature on line 3 is slightly higher than that of line 2 as the entire substrate has heated up.

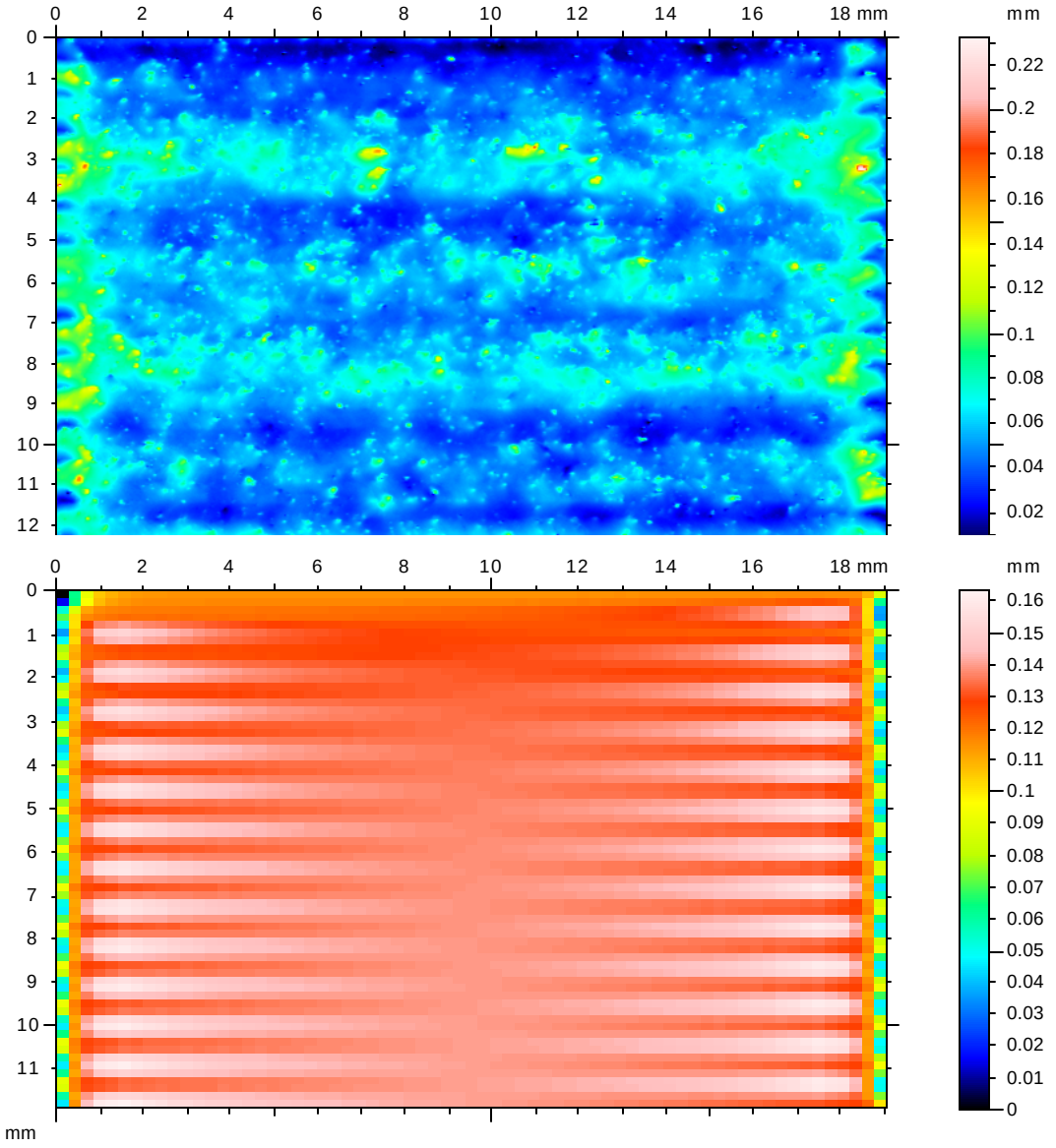

Figure 31: Measured and Simulated Surfaces (1-Layer Sample 01)

The measured surface compared to the simulated surface generated using the spatial deposition model. The laser moved from left to right, top to bottom while building the sample. The sample is coldest in the top center, and therefore, has the least deposition at that location. The simulation appears to match the measurement trends. Left and right edges show higher deposition in both the sample and the simulation.

The calculated average temperatures just before the laser passes over an element can be converted to energy. Consequently, even though the laser puts out constant energy to each location in the layer, each location has a different amount of energy available due to

substrate heating. This increase in energy translates into increased deposition. Figure 31 shows the predictive capability of the spatial deposition model applied to a layer sample.

The laser moved from left to right, top to bottom while building the sample. Therefore, the sample is coldest in the top center, and should have the least deposition in that region. The simulation matches the height measurements in this respect, correctly predicting the trend of increasing heights from top to bottom.

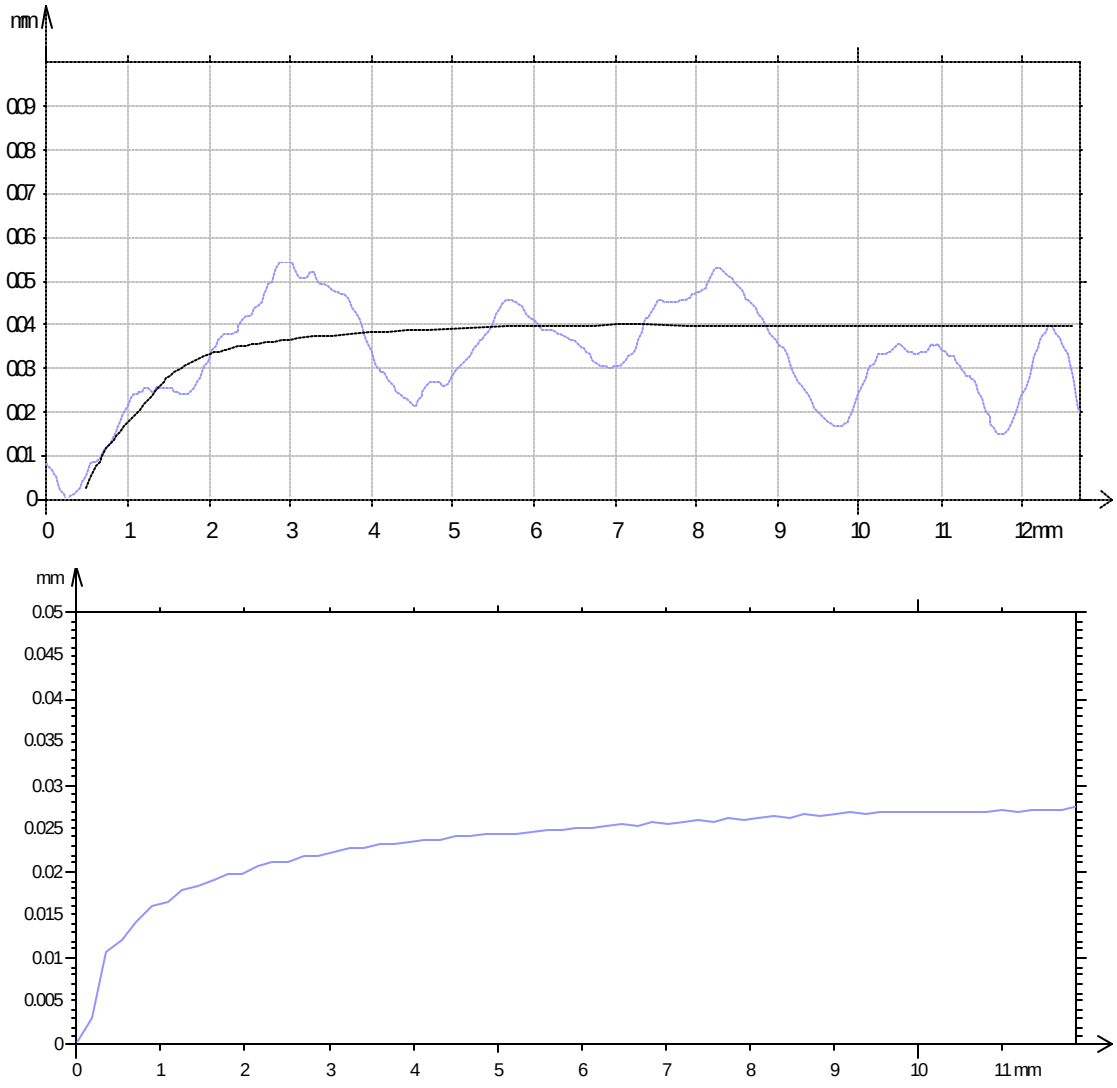

Figure 32: Average profile, north-south direction

The averaged profiles of the sample in the north-south direction are considerably more rugged than the simulation predicts, but the general trend of deposition increasing from left to right appears to match.

All profiles in the north-south direction on the sample were averaged and compared to corresponding averaged profiles from the simulation (see Figure 32). Deposition increases along the $y-$direction of the sample, since substrate temperature increases as

the build progresses in that direction. The averaged profile of the sample appears to be more jagged than that of the simulated surface. Figure 30 shows why this is so – the calculated temperature, energy or deposition has the same general profile along every line, mirrored about the center of the sample – averaging merely smoothes variations at line ends.

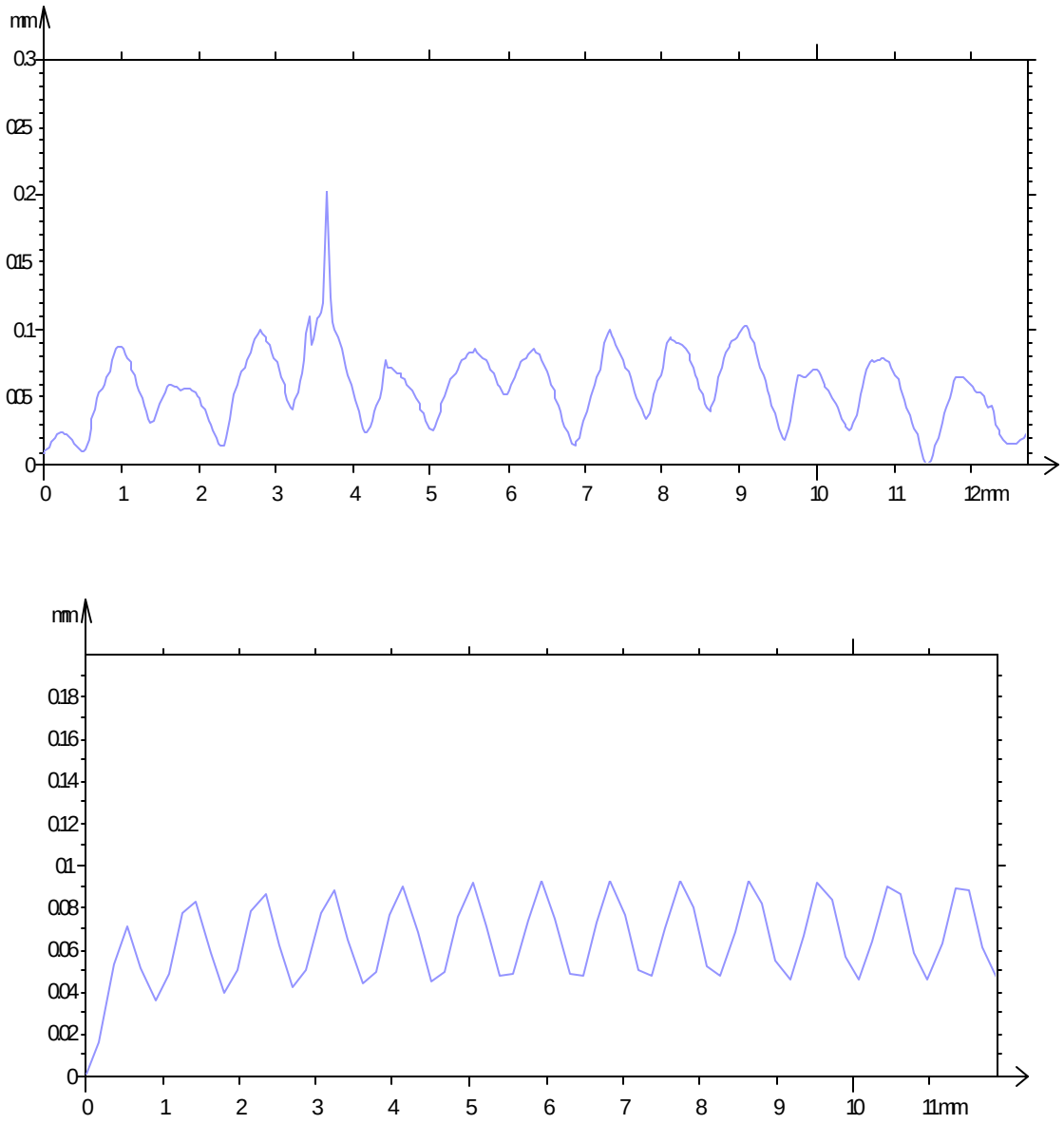

Figure 33: Single profile, north-south direction, 0.1 mm from left edge

A single profile in the north-south direction 0.1mm from the left edge appears to match the simulation closely. The spike about 3.5 mm from the left edge may have been caused by partially melted powder.

A similar comparison was made on a single profile, at a distance 0.1 mm from the left edge of the sample, to study the performance of the model at the edges of the sample, where substrate heating was the highest. Figure 33 shows the profile from the sample

above that from the simulated surface. Peaks appear whenever the laser reverses direction at that edge. There are half as many peaks as there are lines across the sample. The number of peaks on the sample, 13, matches the number of peaks on the simulated surface.

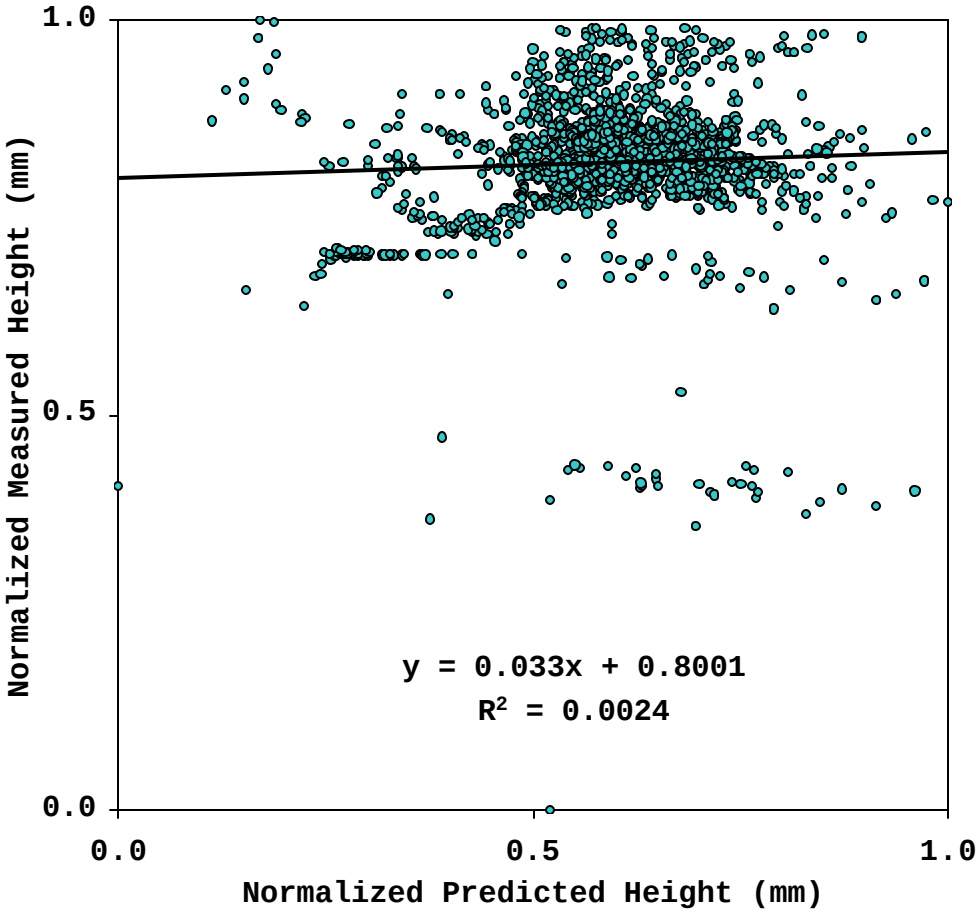

Figure 34: Thickness-Thickness plot for the SDM

There appears to be nearly no correlation between the measured and predicted deposit thickness, even after the measurements have been normalized to lie between 0 and 1. This is not necessarily indicative of poor model performance – similar metrics in the field of surface metrology sometimes show the same results.

The surfaces were normalized so the measurements lay between 0 and 1 and were plotted against the normalized predictions (Figure 34). The regression line indicates near-zero correlation between the predictions and the measurements. This unexpectedly poor correlation has been noticed in the field of surface metrology, when replicas are compared with the surfaces they were made from; slight errors appear to disproportionately affect the correlation.

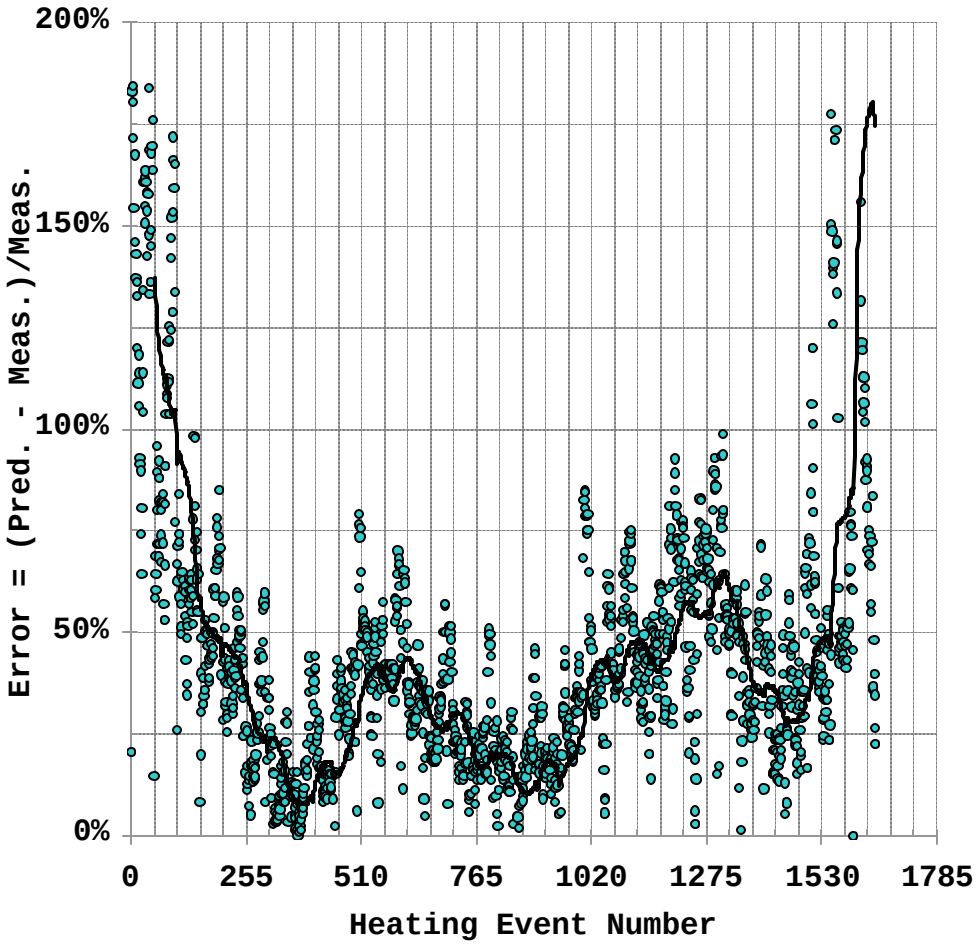

Figure 35: Error plot for the SDM

The figure shows the error as the build progresses. The model performance appears weakest at the start of the build and at the end.

The error between the predicted and the measured surface was calculated and is shown in Figure 35. The model clearly performs poorly at the start of the build and at the end of the build. The poor performance at the start of the build is easily explained, because the laser appears not to have drawn the first line. This is immediately apparent from a photograph of the surface. The weak performance of the model at the end of the build is probably because the recursive calculations of substrate heating stop at the location of interest. This implies that deposition stops as soon as the laser has past the point of interest. A more realistic approach must incorporate deposition at the location after the laser has passed it, since the location does not instantly freeze.

The predictions of the spatial deposition model can be averaged to compare them with the average heights measured. Figure 22 shows the averaged predictions of the spatial deposition model applied to the 1-layer builds. The results seem to parallel those from the average deposition model. The 1-layer build heights appear linear with the

predictions as they were built under relatively isothermal conditions and should be less affected by substrate heating.

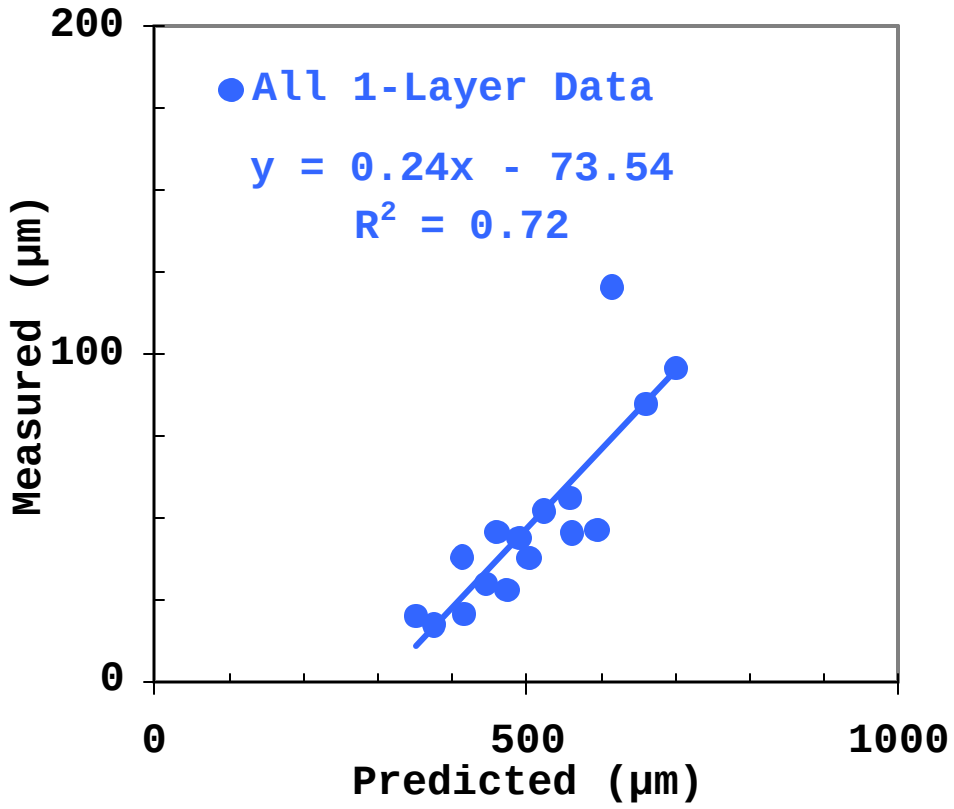

Figure 36: Spatial Deposition Model Applied to 1-Layer Builds

The average height reported by the spatial deposition model is plotted against the average heights measured. The data appear linear, for 1-layer builds where substrate heating is negligible.

Figure 23 shows the averaged predictions of the spatial deposition model plotted against the measured deposited heights for the 2-layer builds. The data for 1-layer builds indicates lie on a straight line as expected, since they were built under near-isothermal conditions. The data for 2-layer builds also appear to lie on a straight line with the same slope, indicating that the model is performing well. However, there appears to be some distinction between the builds that were carried out under lower laser power (shown in pink), indicating, perhaps, that the model is not capturing the entire extent of substrate temperature rise.

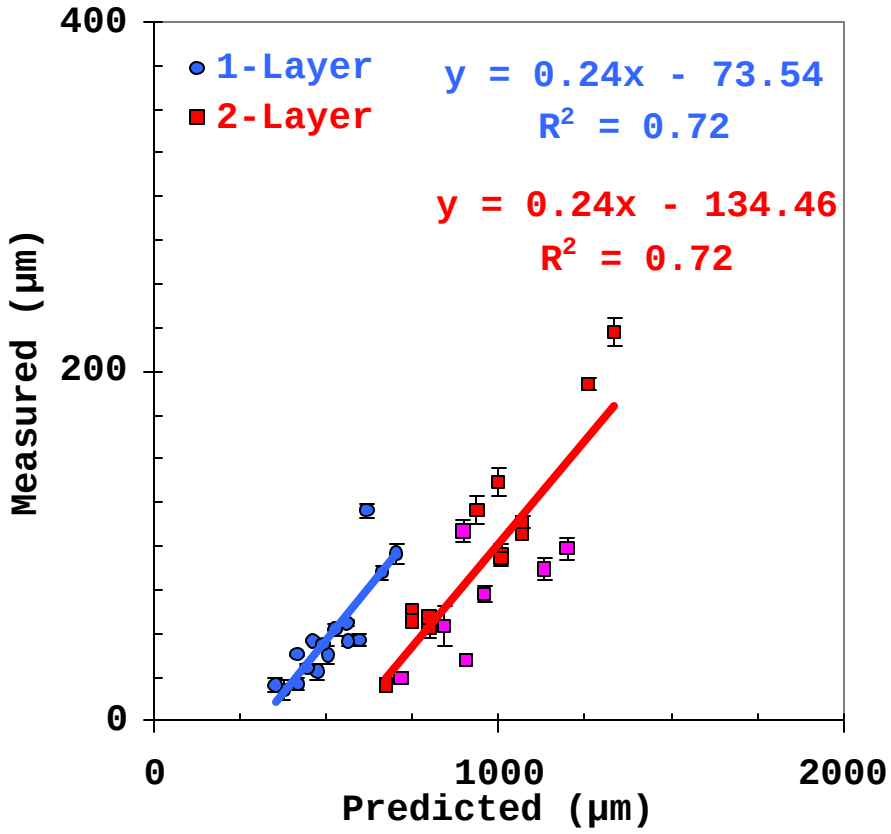

Figure 37: Spatial Deposition Model Applied to 2-Layer Builds

The average height reported by the spatial deposition model is plotted against the average heights measured. The data appear linear, for 2-layer builds, indicating that the model is performing well, but substrate heating causes the data to fall on separate lines (the pink points appear to lie on different lines).

6 Conclusions

6.1 Functional Decomposition

The functional requirements of delivering material and energy to a location are necessarily coupled. Axiomatic design theory suggests that matrix operations on design tables can reduce or eliminate coupling between functional requirements and design parameters but appears to be inadequate when dealing with functional requirements that are coupled.

Functional decomposition of the equipment design has indicated that not all variables that affect deposition are under closed loop control; in fact, some of these variables are not even measured.

In particular, substrate temperature, which is variable due to coupling between the hatch pattern being drawn and the laser power is neither controlled nor measured, even though it affects layer thickness. Consequently, process models designed to predict deposition must incorporate the effect of substrate heating.

6.2 Uncertainty

Uncertainty in certain key build parameters and measurements was studied to help interpret the results against the backdrop of experimental realities.

The uncertainty in height measurements appeared low. Inter-instrument comparisons were linear with a correlation coefficient of 0.94. Intra-instrument comparisons were linear with a correlation coefficient of 0.95. Therefore, any deviations in sample height from the predicted height were probably not caused by measurement errors and must be due to variations in other build parameters or deficiencies in the model.

The uncertainty in the mass flow rate was higher than that in height measurements. This knowledge was valuable in planning experimental protocol. In particular, mass flow rate appeared to be nearly constant approximately 10 minutes after the command to change it had been made, though it could deviate from the set value once this period has elapsed. The magnitude of the deviation appeared dependent on time. Mass flow rate also appeared influenced by the previous motor setting, by machine shut down and appeared to vary between runs.

These observations indicated that the relationship between motor rpm and mass flow rate cannot be encapsulated in an equation, and had to be reaffirmed before experiments.

6.3 Model Performance

Two process models were developed to predict deposition as some function of build parameters, material properties and geometry terms. The average deposition model was designed to predict deposition for builds in which substrate heating is minimal. The spatial deposition model was designed to predict deposition for builds in which substrate heating is significant. Both models used the same material delivery model and were tested using single line, 1-layer and 2-layer builds; totaling 101 experiments.

6.3.1 Material Delivery Model

The material delivery model predicted that the deposition would be linear with $\sqrt{\frac{\dot{m}}{u}}$. This relationship appeared valid for all builds in the experimental matrix. The correlation coefficients varied between 0.66 and 0.85, for single line builds, and between 0.66 and 0.96 for the layer builds, the lower values often being affected by just one outlier. According to the model, the constant of proportionality, K_M, was expected to be linear with the diameter of the melt pool. A plot of K_M versus laser power suggested that a critical laser power of $P_c = 65\ W$ was required to initiate melting, a value slightly lower, but consistent with experimental observations.

6.3.2 Average Deposition Model

The average deposition model predicted that deposition should be linear with $\sqrt[4]{\frac{(P-P_c)\dot{m}}{u^2}}$. The experimental data appeared to support this for all builds in the experimental matrix. Correlation coefficients for single line builds were 0.77, and varied between 0.49 and 0.91 for the layer builds. The low correlation coefficient for some of the layer builds was due to a single outlier. The model also predicted that deposition would be linear with $\sqrt{\frac{(P-P_c)}{u}}$, which seems to be supported by experimental results. In conclusion, the average deposition model developed in this dissertation appears to be capable of relating build parameters to deposited height for builds in which substrate heating is negligible.

6.3.3 Spatial Deposition Model

The predictions of spatial deposition model were averaged and compared with the measured deposition. The predictions appear to match measurements, suggesting that the approach followed in developing the model could be valid. The comparison of simulated

surfaces generated by the spatial deposition model with the experimental surfaces indicates that the model is able to predict broad trends – high and low locations in measured surfaces appear as high and low locations in the simulated surface. In conclusion, the spatial deposition model appears to be capable of predicting deposition trends due to rastering because it incorporates substrate heating.

7 Recommendations for Future Work

This dissertation represents a first step in modeling deposition in LENS™. The models derived may be refined by eliminating some of the assumptions and the uncertainty associated with them.

7.1 Refining Energy delivery models

Some omissions that could affect the calculation of energy in this model include:

- Energy loss mechanisms such as radiation, melt-pool convection and scattering by powder particles.
- The degree of superheat in the melt pool.
- The variation of thermal properties of many alloys with temperature.

Predictions can be refined if these omissions are addressed.

The spatial deposition model calculates the effect of all previous heating events to estimate the substrate temperature just before the laser reaches a location. The location is known to stay molten for some time after the laser passes, and is almost certainly re-melted when the laser passes by it when drawing the next line. Deposition probably continues as long as the location is molten, since mass is distributed so indiscriminately over the build. Future versions of the program might incorporate this into the calculation.

7.2 Refining Material delivery models

The material delivery model assumes an even distribution of mass in the powder cones. Mass probably varies from a maximum, along the axis to a minimum, along the boundaries of each cone. The region of intersection, therefore, will contain a greater fraction of the mass than expected. Future models might include equations that estimate the distribution of mass in the cone.

The powders are assumed to have a unimodal distribution of diameters. This is known to be an invalid assumption – the powders typically have a range of diameters. The distribution of powder diameters in the powder cone may be included in refinements.

8 List of References

3D Systems, 2001	*3D Systems Annual Report, 2001*; available on the web at: http://www.3dsystems.com/company/investor/annual_2001.pdf
Amon *et al*, 1993	"*Material Issues in Layered Forming*"; Solid Freeform Fabrication Symposium, 1993.
Arcella and Froes, 2000	"*Producing Titanium Aerospace Components from Powders Using Laser Forming*", Journal of Materials, May 2000, p 28-30.
Ashley, 1997	"*From CAD art to Rapid Metal Tools*"; Mechanical Engineering; 1997.
Boddu *et al*, 2001	"*Control of Laser Cladding For Rapid Prototyping – A Review*"; Solid Freeform Fabrication Proceedings, 2001, pp 460-467.
Brooks *et al*, 1999	"*Microstructure and Property Optimization of LENS Deposited H13 Tool Steel*", Solid Freeform Fabrication Proceedings, 1999, pp 375-382.
Brooks *et al*, 2000	"*Microstructures of Laser Deposited 304L Austenitic Stainless Steel*"; Materials Research Society Symposium Proceedings, Vol. 625; 2000.
Brown *et al*, 1982	"*Method for Fabricating Articles by Sequential Layer Deposition*"; 1982.
Carslaw and Jaeger, 1965	"*Conduction of Heat in Solids*"; University Press, Oxford, 1965.
Doumanidis, 1995	"*Thermal Analysis and Design of Scanned Rapid Prototyping*"; IMECE, Proceedings of the ASME Heat Transfer Division, HTD-Vol. 317-2, 1995.
Ensz *et al*, 1998	"*Software Development for LENSÔ*"; Solid Freeform Fabrication Symposium; 1998.
Ensz, 2000	"*Process Characterization and Increased Deposition Rates*"; LENS™ CRADA website, 2000.
Ensz, 2000	"*Modeling*"; LENS™ CRADA Website, October 2000.
Fadel *et al*, 2001	"*Manufacturing of a Heterogeneous Flywheel on a LENS Apparatus*"; Solid Freeform Fabrication Proceedings, 2001, pp 553-560.
Fessler *et al*, 1997	"*Functional Gradient Metallic Prototypes through Shape-Deposition Manufacturing*"; Solid Freeform Fabrication Proceedings, 1997
Froes, 2000	"*Laser Forming Titanium Components from Powder*"; Materials Technology and Advanced Performance Materials; 2000 15-1:6-33.
Gerekin, 1994	"*Rapid Prototyping of Metal Components by Laser Cladding*"; International Symposium on Automotive Technology and Automation, 1994, Aachen, Germany.
Gorka, 2000	"*Thermal Fields in Materials Irradiated with CO_2 Laser Beam; Laser Technology VI: Applications*"; Proceedings of SPIE, Vol 4238 (2000).
Griffith *et al*, 1996	"*Freeform Fabrication of Metallic Components Using Laser Engineered Net Shaping (LENS™)*"; Proc. Solid Freeform Fabrication Symposium, Ug12-14, 1996.
Griffith *et al*, 2000	"*Understanding the Microstructure and Properties of Components Fabricated by Laser Engineered Net Shaping*"; Materials Research Society Symposium Proceedings, Vol. 625; 2000.
Halliday and Resnick, 1966	*"Physics, Part I and II*", John Wiley and Sons, Inc., 1966.
Hammeck, 1988	"*Laser Spray Nozzle and Method*"; US Patent Number 4724299; 1988.
Hofmeister *et al*, 1999	"*Investigating Solidification with the Laser-Engineered Net Shaping (LENSÔ) Process*"; Journal of Materials, Vol. 51, No 7, (1999) available online from JOM-e online at: http://www.tms.org/pubs/journals/JOM/9907/Hofmeister/Hofmeister-9907.html
Hu, 1998	"*Direct Fabrication of Nano-Reinforced Metallic Foams*"; US Army Phase I Selections from 99_2 Solicitation, 1998.
Jacobs, 1992	"*Rapid Prototyping and Manufacturing: Fundamentals of*

Stereolithography"; Society of Manufacturing Engineers, 1992, ISBN: 0-87263-425-6.

Jacobs, 1996 "*Stereolithography and Other RP & M Technologies; From Rapid Prototyping to Rapid Tooling"*; Society of Manufacturing Engineers, 1996, ISBN: 0-87263-467-1.

Jacobs, 2000 "*The Evolution of the LENSÔ Number*"; Internal Communication, LaserFare, Inc., Warwick, RI, USA.

Jeantette *et al*, 2000 "*Method and System for Producing Complex Shaped Objects*", US Patent Number 6046426; 2000.

Kaplan, 2000 "*Mathematical Models of Laser Assisted Rapid Prototyping"*, Applied Physics Letters, 2000.

Keicher and Smugeresky, 1997 "*The Laser Forming of Metallic Components Using Particulate Materials*"; Journal of Materials, May 1997.

Keicher *et al*, 1999 "*Multiple Beams and Nozzles to Increase Deposition Rate*"; US Patent Number 5993554; 1999.

Keicher, 1998 "*Multi-Alloy Fabrication Method for Turboshaft Engines*"; US Army Phase I Selections from 99_2 Solicitation, Optomec Inc., 1998.

Kobryn and Semiatin, 2001 "*Mechanical Properties of Laser-Deposited Ti-6Al-4V*"; Solid Freeform Fabrication Symposium; 2001.

Kummailil, 2000 "*Functionally-Adapted Biomimetic Materials for Space Exploration; Year-I Report*", NASA Grant NAG5-8830, 2000.

Kummailil, 2001 "*Functionally-Adapted Biomimetic Materials for Space Exploration; Year-II Report*", NASA Grant NAG5-8830, 2001.

Lewis and Less, 1999 "*Deposition Head for Laser*"; US Patent Number 5961862; 1999.

Lewis *et al*, 1998 "*Laser Production of Articles from Powders*"; US Patent Number 5837960; 1998.

Li *et al*, 2000 "*Mechanical and Thermal Behavior of Laser-Deposited Metal Matrix Composites of Invar and TiC*"; Materials Science & Engineering A282 (1-2) 86-90, 2000.

Mazumder *et al*, 1997 "*The Direct Metal Deposition of H13 Tool Steel for 3-D Components*", Journal of Materials, 49 (5) (1997), pp. 55-60.

Mazumder *et al*, 2000 "*Closed Loop Direct Metal Deposition: Art to Part*"; Optics and Lasers in Engineering 34, (2000) 397-414.

Metals Handbook, 1979 *"Metals Handbook, Ninth Edition Volume 2 Properties and Selection: Non-Ferrous Alloys & Pure Metals*", pages 816, ISBN 0-87170-008-3; 1979.

Mills, 2002 "*Recommended Values for the Thermophysical Properties for Selected Commercial Alloys*", Woodhead Publishing Ltd., Cambridge, England, ISBN 0-87170-753-5, 2002.

Nguyen *et al*, 1999 "*Analytical Solutions for Transient Temperature of Semi-Infinite Body Subjected to 3-D Moving Heat Sources*"; Welding Research, Supplement to the Welding Research Journal, August 1999.

Nickel *et al*, 2001 "*Thermal Stresses and Deposition Patterns in Layered Manufacturing"*; Materials Science & Engineering A317 (59-64), 2001.

Nickel, 1999 "*Analysis of Thermal Stresses in Shape Deposition Manufacturing of Metal Parts*"; Ph. D Thesis, Stanford University, 1999.

Noecker, 2000 "*Functionally Graded Copper-H-13 Tool Steel using LENSÔ Process*"; Lehigh University; 2000.

Pinkerton, A.J. and Li, L. "*The significance of deposition point stanfdoff variations in multiple-layer coaxial laser cladding (coaxial cladding standoff effects)"*; International Journal of Machine Tools and Manufacture; Volume 44, Number 6; pg 573.

Piskunov, 1981 "*Differential and Integral Calculus*" Volume II, MIR Publishers, Moscow, page 255; IV Printing, 1981.

Rabinovich, 1996 "Rapid Prototyping System"; US Patent Number 5578227; 1996.

Resch *et al*, 2001 "*Laser-Assisted Generating of Three-Dimensional Parts by the Blown Powder Process*"; XIII International Symposium on Gas Flow and Chemical Lasers and High-Power Lasers Conference, Antonio Lapucci, Marco and

Ciofini, Editors, Proceedings of SPIE Vol. 4184 (2001).
Rolincik, 1998 "*Dual-Alloy Titanium Aluminide Technology for Turboshaft Engines*"; US Army Phase I Selections from 99_2 Solicitation, Triton Systems, Inc.; 1998.
Rostami and Raisi, 1997 "*Temperature Distribution and Melt Pool Size in a Semi-Infinite Body due to a Moving Laser Heat Source*"; Numerical Heat Transfer, Part A, 31:783-796, 1997.
Sachs, 2001 "*Manufacturing by Solid Freeform Fabrication*"; Solid Freeform Fabrication Proceedings, 2001, pp 596-618.
Schneider, 1998 "*Laser Cladding with Powder: Effect of Some Machining Parameters on Clad Properties*"; Ph. D. Thesis; University of Twente, Enschede, The Netherlands, 1998.
Suh, 1990 "*The Principles of Design*", Oxford University Press, Inc., 1990.
Suh, 2001 "*Axiomatic Design: Advances and Applications*"; Oxford University Press, Inc., 2001.
Whitney *et al*, 1991 "*Axial Flow Laser Plasma Spraying*"; US Patent Number 5043508; 1991.
Xie and Kar, 1999 "*Laser Welding of Thin Sheet Steel with Surface Oxidation*"; Welding Research Supplement, October 1999, p 345-s.

8.1 General References

Ogden, T.E. and Goldberg, I.A., 2002 "*Research Proposals, A Guide to Success*", III Ed.; Elsevier Science, ISBN 0-12-524733-8.

9 Appendices

Appendix A: Overview of the LENS™ Process

Metal deposition is achieved by feeding a powder stream into the molten pool created by focusing a high-powered laser on a metal substrate. The powder melts into the pool, increasing its volume. A raised melt bead is formed as the laser is moved along any path on the substrate. Partial superposition of adjacent melt beads creates a raised area; thus, moving the laser beam along a path while simultaneously feeding the pool with metal powder creates a raised shape. This raised area is usually thin compared to the other dimensions and is commonly termed a layer or a lamina. Griffith (Griffith *et al*, 1996) and Mazumder (Mazumder *et al*, 1997) provide excellent process overviews of a variety of SFF processes and Sachs (Sachs, 2001) details the factors that need to be overcome for them to mature into a manufacturing technology.

9.1 Major Sub-Systems

9.1.1 Translation

The current model being produced is called the LENS™ 850, which is a 3-axis machine. Later incarnations with 5 axes are in development, but several issues associated with the reliability of the 3-axis machine have not been resolved yet.

Translation is achieved using a typical heavy-duty xy – stage driven by servomotors. Travel is approximately 30 cm in the horizontal plane and positional accuracy is ±100 µm. A unidirectional stage provides translation in the z-direction and is used to maintain the substrate surface at the laser focus throughout the build.

The work-piece was attached to the stage in earlier incarnations of the equipment. This adversely affects the acceleration and deceleration characteristics of the stage due to inertia. Later models attach the laser to the stage and move it over the stationary work-piece, a technique that has the significant disadvantage of affecting the powder delivery.

9.1.2 Powder Delivery

This is the least reliable sub-system in the machine. Powder is stored in a hopper in which a perforated disc rotates at a controlled angular velocity. The powder collects in the perforations and is carried above the powder surface by the disc. An inert gas carries this powder along a tube and into the head, from which it flows through 4 symmetric

nozzles into the melt pool. A gas recycling system is used to maintain relatively constant pressure in the chamber.

9.1.3 Energy Delivery

The power source is a water-cooled 1000 Watt Nd:YAG laser, the output of which is fed into a fiber-optic cable and passed through focusing optics to obtain a focal point roughly 1 mm in diameter. A water chilling system is required to control and maintain temperature of the lasing elements.

9.1.4 Atmosphere Control

An inert atmosphere is required, as molten metals tend to react aggressively in the presence of air. In addition, they tend to dissolve atmospheric gases to the general detriment of their physical properties. The chamber is usually pumped down and back-filled with an inert gas such as argon. The inert gas is also used as a carrier gas for the powder and is used in the central purge coaxial with the laser beam, which keeps molten powders from depositing on the optics.

9.2 Equipment Design History

The earliest patent on the LENS™ process was obtained by Brown (Brown *et al*, 1982) and describes a process that uses an energy beam to fuse together powder or wire feedstock and form objects. It became apparent that powder delivery was the most problematic sub-system and a variety of attempts were made to improve upon it. Hammeck (Hammeck, 1988) obtained a patent on a coaxial nozzle design that focused powders into the path of the laser beam, followed by Whitney (Whitney *et al*, 1991), who described a process for melting the powders in the nozzle and depositing the melted material on the substrate. Rabinovich's 1996 patent (Rabinovich, 1996) did away with powder as a source of material and used rectangular metal wire instead, thus circumventing Brown's patent, which specified the use of wire as a source of material but did not specify its cross section.

Further development was carried out at the University of California where Lewis (Lewis *et al*, 1998) obtained a patent that focused on the specifics of the equipment design, followed by one in 1999 (Lewis and Less, 1999) that concentrated on the design of the head, underlying the intractability of the problem of conveying powder reliably. Optomec Inc. obtained a patent on increasing build rate using multiple nozzles and lasers and made the equipment commercially available. Their design used a single laser and multiple nozzles. Jeantette, (Jeantette *et al*, 2000) working at Sandia Corporation, obtained a patent that described "unique components to ensure uniform and continuous flow" of powders. The patent describes a rotating perforated disk that picks up

predictable quantities of powder as it rotates. This design is currently being used in Optomec's machines.

9.3 Major Process Variables

The LENS™ DMD™ machine is designed so several process variables can be adjusted. The paragraphs that follow list the major variables used to control the machine along with a brief description of their effect on the part quality.

9.3.1 Laser Power

This is the power of the laser (Watts) measured at the surface of the substrate.
The laser power controls the amount of energy that is transferred to the powder stream as individual particles pass through the laser beam. Higher power translates into higher powder temperatures and higher substrate temperatures.

9.3.2 Scan Speed

This is the velocity $mm.s^{-1}$ with which the substrate is moved in the $xy-$ plane. Higher scan speeds tend to lower the heat transferred to the substrate, but do not affect the heat transferred to the beads as the speed at which they move through the laser path is controlled by the powder feeder.

9.3.3 Hatch/Raster Spacing

This is the center-to-center spacing (mm) between successive, parallel scans. Closely spaced parallel lines are drawn to create 2D areas in a technique that is called rastering. A closer spacing of these lines would create a thicker layer.

9.3.4 Hatch/Rastering Technique

The rastering technique describes the pattern with which the hatch or raster lines are drawn. This affects the temperature distribution of the penultimate layer. Always starting or ending a hatch pattern in the same region would cause uneven heating of the substrate. An angle that does not exactly divide 360 will ensure that the hatch pattern does not repeat itself on alternate layers.

9.3.5 Powder Size/Size Distribution

The average diameter of the powder is the powder size and the diameter variation is the size distribution. Powders with larger diameters take longer to melt and partially melted powders retain heat longer. Large powder size distributions mean some particles would get much hotter than others would as they pass through the laser beam.

9.3.6 Powder Feed Rate

The mass flow rate of the powder as it leaves the nozzle is the powder feed rate. High powder feed rates increase the amount of metal deposited and dissipate the laser heat.

9.3.7 Layer Thickness

The laser retracts by the layer thickness after every layer. This moves the focal point to the surface of the layer just drawn and enables a part to be built up by one layer.

9.3.8 Beam Offset

The laser creates a molten pool of material that has a certain diameter. Powder particles impinging within this region will melt (either completely or partially) and contribute to material build up. An offset is applied to the centerline of the laser so that the material build-up falls within the contours of the part.

9.3.9 Contour Offset

A layer is drawn in two stages. The contour is traced first, in order to create crisp edges, followed by the rastering lines. In certain cases, it may be advantageous to create multiple contours. Increasing the number of contours creates better edge definition but increases the energy input into edge regions that are already predisposed to overheating. The center-to center distance between the contour lines is the contour offset. A smaller contour offset draws the contour lines closer together, creates a larger edge and reduces the likelihood of the edge re-melting from the laser heat during rastering operations.

9.4 Part Building in LENS™

LENS™, like all SFF techniques, makes use of the fact that it is relatively easy to fabricate two-dimensional (2D) laminae of considerable complexity. Since all 3D objects can be "sliced" into a series of 2D layers, each of which can be fabricated easily, aligning and bonding successive layers would form the 3D object.

The slicing technique used for part building is best illustrated using the simple example of a cone. Figure 1 shows the CAD model of a cone (a), which is "sliced" (b) in the horizontal direction. Since the cone has a regular geometry, all cross sections would be discs with varying diameters. The machine builds the cone one disc at a time, backing away by exactly one disc thickness after each disc is built to keep the laser in focus. Except for the first disc, which is built on the substrate, subsequent discs use the preceding one as their substrate.

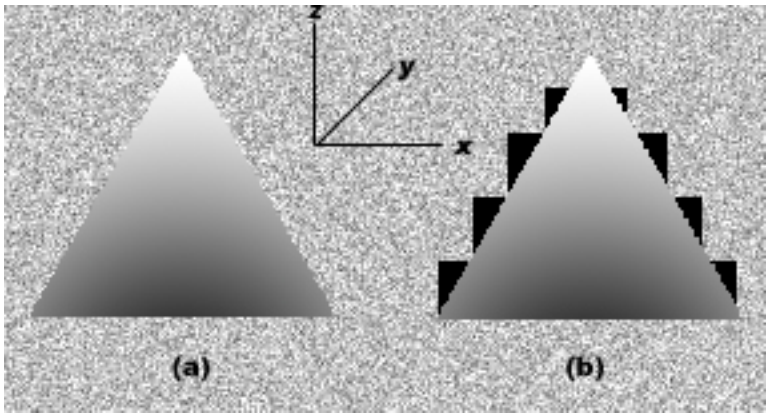

Figure 38: Slicing a cone

(a) A CAD model of a cone. (b) The "sliced" cone, showing steps that occur on angled surfaces. The dark area is the error due to over-building.

Obviously, this process creates some level of error on angled surfaces. The error can be reduced with judicious parameter choices, but can never be completely eliminated.

Comparisons with SFF and non-SFF Technologies

The LENS™ process has several advantages over other SFF technologies.

- It is the only technology that uses metal without binders.
- It uses the widest variety of metals and can dynamically create compositional gradients and alloys.
- Controlling cooling rates $\approx 10^3 K.s^{-1}$ can tailor microstructure.
- Using powder as a raw material obviates the need for an inventory of bar or sheet stock – useful in space and marine applications.
- It is scalable to high volume production.

There are, however, some disadvantages over other SFF technologies.

- Surface roughness is currently poor, usually requiring a secondary finishing operation.
- Dimensional tolerance is low; quoted values of 75 µm in the $xy-$plane and 400 µm in the $z-$direction are material-dependant and optimistic.
- Layers are typically thicker (~500 µm) leading to more pronounced stair-steps.

- Moving the heavy stage or laser causes vibration and inertia-related issues that negatively impact part accuracy.
- It is not possible to build overhangs greater than a certain material-dependent angle.
- Material utilization is currently poor (~ 10 % at best) necessitating a recovery system.

LENS™, like all SFF technologies, has unique capabilities compared to conventional manufacturing technologies. Its primary advantage is the capacity to build complex geometries in the metal of choice with minimal set up time. Other advantages being touted, such as imposing compositional gradients, repairing turbine blades and tailoring the microstructure by controlling the cooling rate are still under development.

It shares disadvantages common to all SFF technologies. There are always stair-steps on angled surfaces, which usually require a finish-machining operation to remove. The build rate is usually too low for use in large-manufacturing, but the minimal setup time makes it viable for prototyping or low volume runs. The dimensional tolerance is poor compared to conventional machining, but a finish machining operation is required in any case.

9.5 Potential LENS™ Applications

Research on the LENS™ process seems to be focused on technology improvements and application development. Application development is currently focused on producing low-volume or "bridge" tooling for injection molds. The market for bridge tooling has been estimated at "tens of billions a year" in 1997. Stucker discusses the manufacture of novel EDM electrodes using this process. Noecker (Noecker, 2000) attempted to identify LENS™ processing parameters to create copper-H-13 tool steels for high thermal conductivity tools. Other researchers focused on turbine blade repair, mold repair, gradient-material components and software development. Optomec and Triton Systems have received government grants to develop aircraft engine components and are pursuing research projects on gradient materials and metallic foams while Tensegra used a NASA grant to create biomimetic, functionally adapted structures using LENS™. Other applications envisioned include turbine blade repair, compositionally graded components, custom EDM electrodes, custom implantable devices and producing single crystal metal components.

Appendix B: Properties of Ti-6 Al-4 V, Ti-6 Al-4 V ELI

Table 14: Recommended Values for the Thermophysical Properties of 90 Ti/6 Al/4 V[4]

Temperature (°C)	Density ($kg.m^{-3}$)	Specific Heat Capacity ($J.g^{-1}.K^{-1}$)	Heat Capacity, Enthalpy ($J.g^{-1}$)	Thermal Conductivity ($J.s^{-1}.m^{-1}.K^{-1}$)
25	4420	0.546	0	7.00
100	4406	0.562	42	7.45
200	4395	0.584	99	8.75
300	4381	0.606	158	10.15
400	4366	0.629	220	11.35
500	4350	0.651	284	12.60
600	4336	0.673	350	14.20
700	4324	0.694	419	15.50
800	4309	0.714	489	17.80
900	4294	0.734	561	20.20
995	4282	0.753	636	22.70
995	4282	0.641	684	19.30
1100	4267	0.66	749	21.00
1200	4252	0.678	816	22.90
1300	4240	0.696	885	23.70
1400	4225	0.714	956	24.60
1500	4205	0.732	1028	25.80
1600	4198	0.750	1102	27.00
1650	4198	0.759	1184	28.40
1650	3920	0.831	1466	33.40
1700	3886	0.831	1508	34.60
1800	3818	0.831	1591	
1900	3750	0.831	1674	

Heat of Fusion for Titanium[5] (estimated): 440 $J.g^{-1}$. No information was available for the alloy.

[4] Recommended Values for the Thermophysical Properties for Selected Commercial Alloys, Kenneth C. Mills, Woodhead Publishing Ltd., Cambridge, England, ISBN 0-87170-753-5, 2002.
[5] Metals Handbook, Ninth Edition Volume 2 Properties and Selection: Non-Ferrous Alloys & Pure Metals, pages 816, ISBN 0-87170-008-3; 1979.

Appendix C: Single-Line Builds

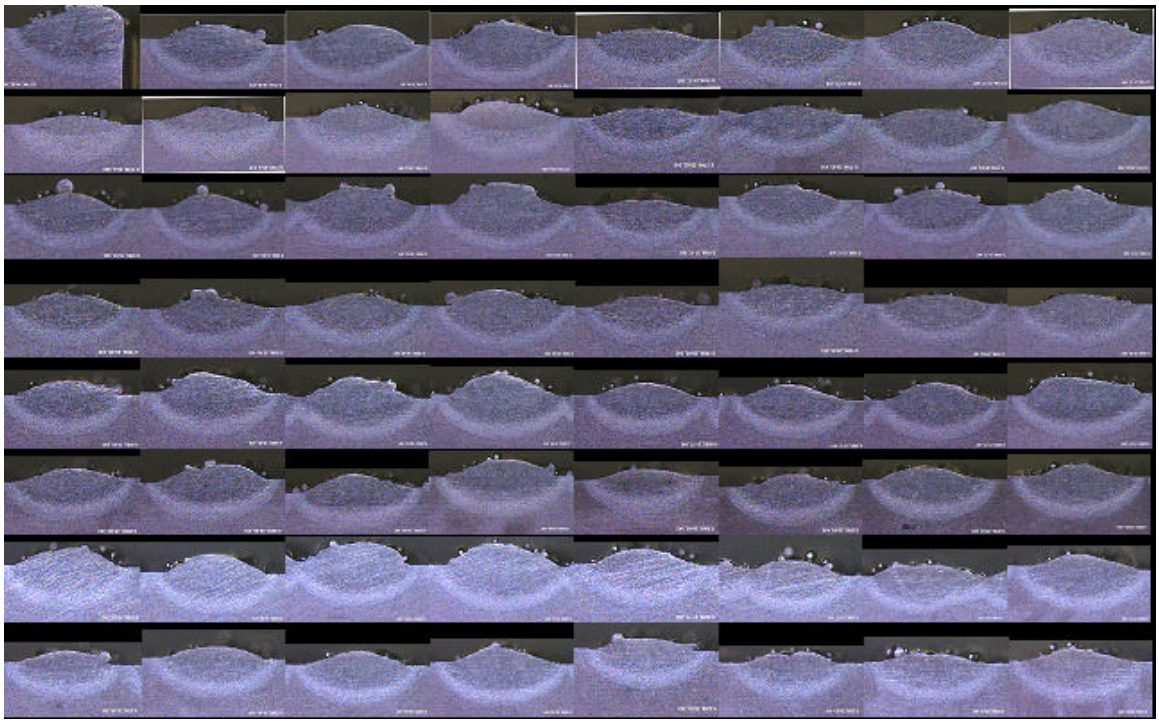

Figure 39: All line build cross-sections

Images are arranged Top to Bottom, Left to Right. There are 8 builds in each row and 64 builds in all. ***Table 11*** *in the Experimental Methods section lists the build parameters for each build.*

Appendix D: 1-Layer Builds

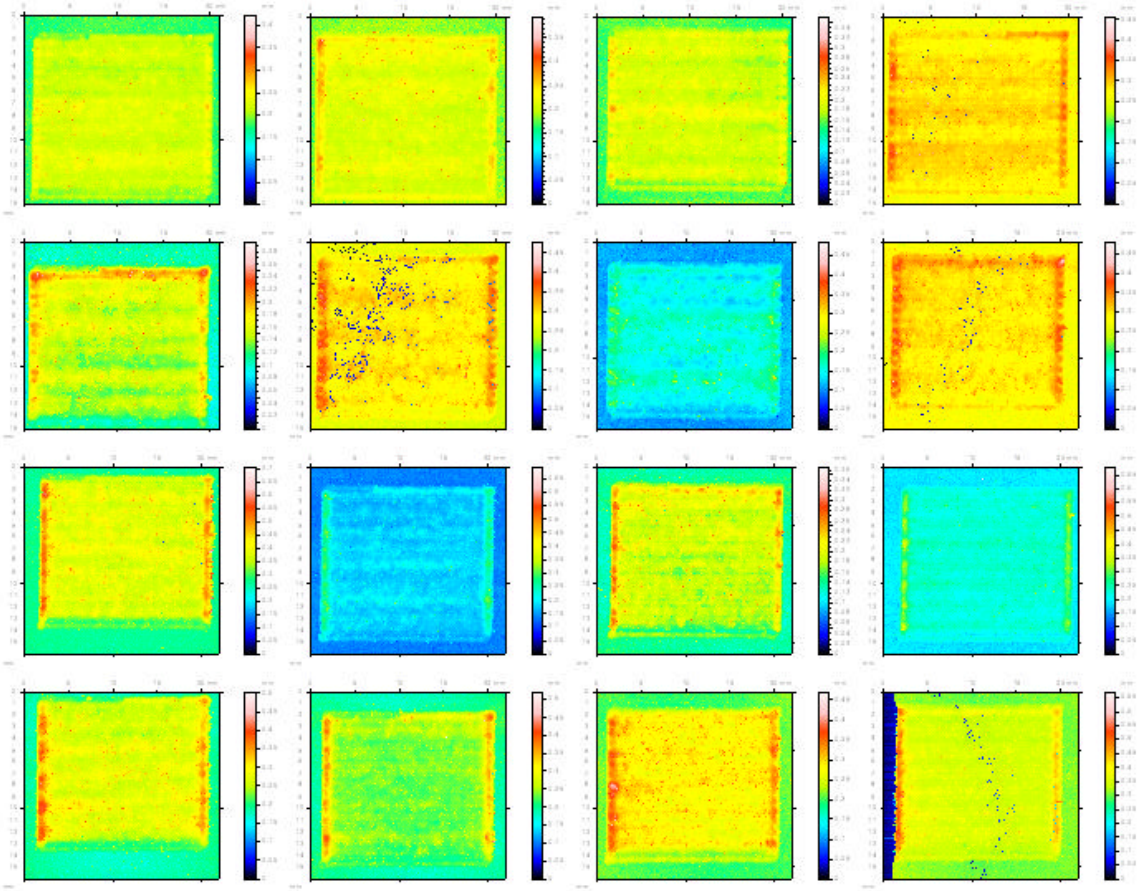

Figure 40: All 1-Layer builds (top view)

Images are arranged Top to Bottom, Left to Right. There are 4 builds in each row and 16 builds in all. ***Table 9*** *in the Experimental Methods section lists the build parameters for each build.*

Appendix E: 2-Layer Builds

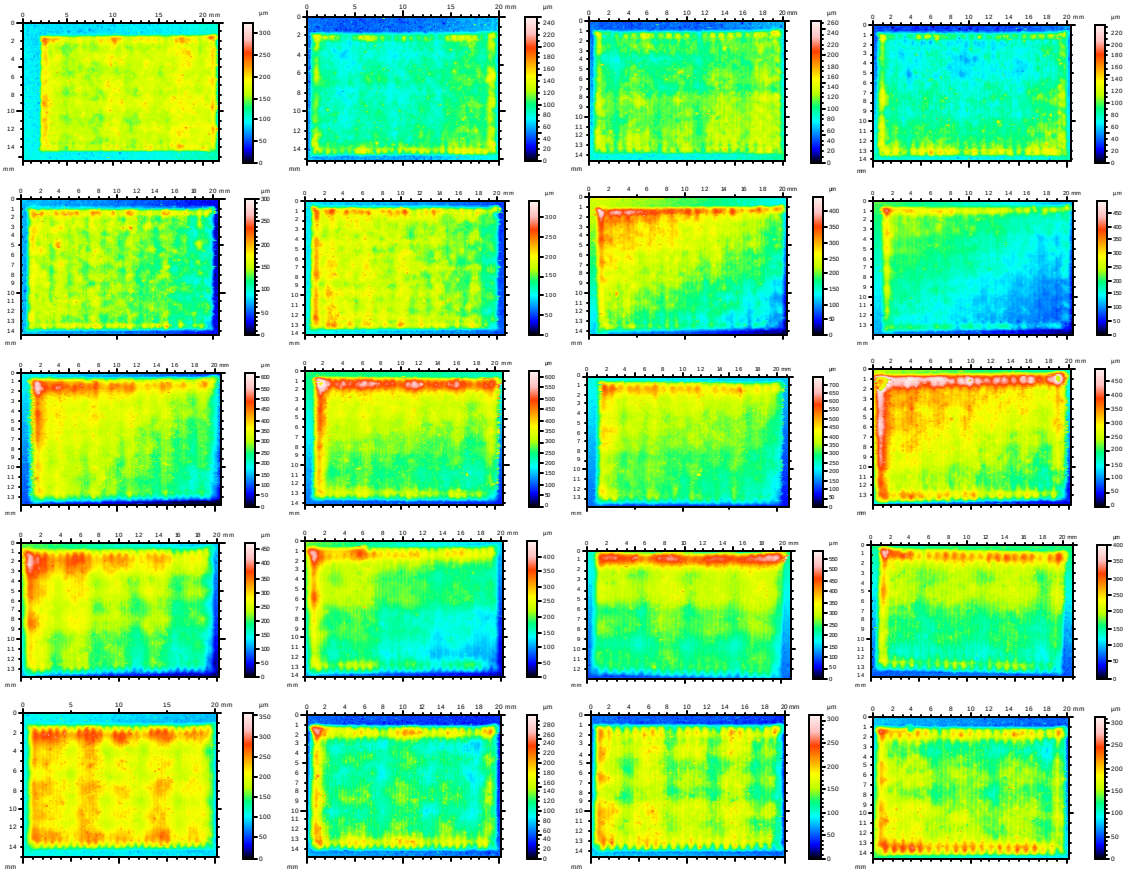

Figure 41: All 2-Layer builds (top view)

Images are arranged Top to Bottom, Left to Right. There are 4 builds in each row and 20 builds in all. ***Table 10*** *in the Experimental Methods section lists the build parameters for each build. The last four builds are repast of samples 5 through 8 (inclusive).*